STIMULI-RESPONSIVE HYBRID NANOMATERIALS:

SPATIAL AND TEMPORAL CONTROL

OF MULTIFUNCTIONAL PROPERTIES

A Dissertation
Presented to
The Academic Faculty

by

Maneesh Kumar Gupta

In Partial Fulfillment
of the Requirements for the Degree
Doctor of Philosophy in the
School of Materials Science and Engineering

Georgia Institute of Technology
December, 2012

STIMULI-RESPONSIVE HYBRID NANOMATERIALS:

SPATIAL AND TEMPORAL CONTROL

OF MULTIFUNCTIONAL PROPERTIES

Approved by:

Dr. Vladimir V. Tsukruk, Advisor
School of Materials Science and Engineering
Georgia Institute of Technology

Dr. Rajesh R. Naik, Co-Advisor
Materials and Manufacturing Directorate
Air Force Research Laboratories

Dr. Kenneth A. Gall
School of Materials Science and Engineering
Georgia Institute of Technology

Dr. Valeria T. Milam
School of Materials Science and Engineering
Georgia Institute of Technology

Dr. Seung Soon Jang
School of Materials Science and Engineering
Georgia Institute of Technology

Date Approved: October 19, 2012

Dedicated to my loving family, Kamna, Anju, Mom and Dad

ACKNOWLEDGEMENTS

During my graduate studies, I have had the great fortune of having two tremendously supportive advisors, Prof. Vladimir Tsukruk and Dr. Rajesh Naik. Prof. Tsukruk has been an ideal mentor as he provided me with a clear direction and vision, but placed tremendous trust in me to generate ideas and solve problems. Whenever I have gotten stuck he has been understanding, compassionate, and generous with his time and help. He has ensured that I have had opportunities during my PhD that I could not have imagined, and has always been a strong advocate for my interests giving me the best possible advice. Most importantly, I am grateful for the push and motivation he has given me to identify my deficiencies and attempt to overcome them. While this is an ongoing process, I would not be where I am without him. Dr. Rajesh Naik gave me an opportunity to work at AFRL among world class researchers when I had little background or experience. This experience was a turning point for me. It gave me a sense of direction, and eventually the chance to pursue a PhD at Georgia Tech. Throughout my PhD, he has been a friend and great mentor generously offering his technical expertise, broader perspective, and personal advice. I would also like to thank Prof. Kenneth Gall, Prof. Seung Soon Jang, and Prof. Valeria Milam for their helpful feedback, suggestions, and kind willingness to take part in my dissertation committee.

This research effort would not be possible without the strong support of current and former SEMA lab members, special thanks are due to Prof. Srikanth Singamaneni, Dr. Michael McConney, Dr. Ray Gunawidjaja, Dr. Sehoon Chang, Dhaval Kulkarni, Swati

Naik, Dr. Tobias Konig, and Ren Geryak for the significant contributions they have made in the work presented here. Over the past four plus years, the SEMA lab has become like home for me. Not because of long hours, but because of the great friends who have made research a truly fun and wonderful experience.

I am also grateful for the chance to work with truly exceptional collaborators as a part of the Georgia Tech-AFRL BIONIC center. Dr. R. Vaia, Dr. L. Drummy, Dr. D. Nepal, Dr. S. Biswas, Dr. T. Bunning, Dr. M. Durstock, Dr. B. Taylor, and J. Deneault from the AFRL; Prof M. El-Sayed, Prof. A. Fedorov, David Anderson, and Rachel Near from Georgia Tech have provided helpful discussion, feedback, and assistance in many critical experiments. Their help and contribution in the successful completion of this work cannot be overstated. Funding for this work has been provided by the Air Force Office of Scientific Research and the Air Force Research Laboratory. I would also like to offer a special thanks to Mr. and Mrs. Corcia for their generous fellowship.

Finally, I could never complete this journey without the unconditional love and support of my family. My dear wife, Kamna, is both my best friend and the love of my life. I am deeply grateful to her for joining me in the middle of this endeavor. She has given me a real home away from the lab, and has been a constant source of happiness and optimism. My younger sister, Anju, is a great friend who can always make me smile. I owe my life to my parents. They both have provided me and my sister with every imaginable opportunity and taught us the value of hard work, sacrifice, and service to family and community.

TABLE OF CONTENTS

Page

ACKNOWLEDGEMENTS iv

LIST OF FIGURES ix

LIST OF SYMBOLS AND ABBREVIATIONS xiv

SUMMARY xv

CHAPTER

1 INTRODUCTION 1

1.1 Motivation 1

1.2 Background 5

1.2.1 Responsive Polymers and Biopolymers 5

1.2.2 Silk Fibroin 7

1.2.3 Plasmonic Nanoparticles 10

1.2.4 Template-Assisted Fabrication 13

1.2.5 Active Plasmonic Devices 16

2 RESEARCH GOALS AND OVERVIEW 22

2.1 Research Goals 22

2.2 Organization and Composition of Dissertation 24

3 EXPERIMENTAL TECHNIQUES 29

3.1 Fabrication Techniques 29

3.1.1 Fabrication of Ultrathin Silk Films 29

3.1.2 Fabrication of Layer-by-Layer Polymer Films 29

3.1.3 Fabrication of Porous Anodic Alumina Templates 30

3.1.4 Electrodeposition of Metals 32

3.2 Characterization Techniques 33

3.2.1 Atomic Force Microscopy 34

3.2.2 Confocal Raman Microscopy 35

3.2.3 Electron Energy Loss Spectroscopy 35

3.2.4 Single Particle Spectral Measurements 36

3.2.5 Computational Modeling of Plasmonic Modulation 37

4 TEMPLATE-BASED FABRICATION STRATEGY FOR MICROPATTERNING PROTEIN CHAIN CONFORMATION IN SILK MATERIALS 38

4.1 Introduction 38

4.2 Experimental Methods 41

4.3 Results and Discussion 43

4.4 Conclusion 52

5 pH TRIGGERED SERS VIA MODULATED PLASMONIC COUPLING IN INDIVIDUAL BIMETALLIC NANOCOBS 54

5.1 Introduction 54

5.2 Experimental Methods 57

5.2.1 Preparation of Bimetallic Nanocobs 58

5.2.2 Characterization 60

5.3 Results and Discussion 61

5.4 Conclusion 70

6 UNIFORM SURFACE ASSEMBLY AND SINGLE PARTICLE MEASUREMENTS OF ANISOTROPIC PLASMONIC PROPERTIES IN STRONGLY COUPLED GOLD NANORODS 72

6.1 Introduction 72

6.2 Experimental Methods 75

6.2.1 Template-Based Synthesis of Segmented Nanorods 76

6.2.2 Immobilization of Nanorods 77

6.2.3 Characterization 77

6.2.4 DDA and FDTD Simulations 78

6.3 Results and Discussion 79

6.3.1 Assembly of Segmented Nanorods on Surfaces 79

6.3.2 Single Particle Scattering Measurements 86

6.4 Conclusions 99

7 A ROBUST AND FACILE APPROACH TO ASSEMBLING TUNABLE, MOBILE, AND HIGHLY-OPEN UNFRUSTATED TRIANGULAR LATTICES FROM FERROMAGNETIC NANORODS 100

7.1 Introduction 100

7.2 Experimental Methods 102

7.2.1 Fabrication of Nickel Nanorods 102

7.2.2 Magnetic Assembly 103

7.2.3 Tethering Nanorods to Substrate 104

7.2.4 Characterization 104

7.3 Results and Discussion 105

7.4 Conclusion 116

8 GENERAL CONCLUSIONS, IMPACT, AND FUTURE DEVELOPMENTS 119

REFERENCES 126

VITA 142

LIST OF FIGURES

Page

Figure 1.1: General schematic for application of responsive polymers in active plasmonic hybrids depicting colorimetric response due to change in particle coupling and surrounding dielectric 4

Figure 1.2: Schematic of the interaction of an EM Wave with a metal nanosphere, depicting the polarization in the direction parallel to external electric field 10

Figure 1.3: SEM images showing the packing at different surface pressures (left) and corresponding photographs of the air water interface showing the striking color change (right) 12

Figure 1.4: Evolution of longitudinal and transverse LSPR peaks in gold nanorods as the aspect ratio increases. Top left shows the color of the gold solutions changing as the aspect ratio of the nanorods increases as seen in the corresponding micrographs (bottom). The color change is due to evolution of the longitudingal LSPR peak (top right), which has a large absorbance and is very sensitive to the aspect ratio. 13

Figure 1.5: Examples of porous anodic alumina. A) Commercial anodisc from Whatman (100 nm pores); B-D)Alumina templates fabricated in sulfuric, oxalic, and phosphoric acid electrolytes respectively. 15

Figure 1.6: Active plasmonics schematic showing common strategies for tuning of LSPR peak in metal nanostructures. 16

Figure 4.1: Strategy for patterning secondary structure in silk films. a) Schematic of the patterning strategy, from top to boootm. First, a PS mask is deposited on the silk film by CTL. Next, the silk film is selectively exposed to methanol vapor converting the exposed regions to silk II. Third, the PS mask is removed in toluene. Finally, the silk I regions can be selectively dissolved in water to reveal the patterning. b) Optical image of silk film with PS mask deposited on top (inset is the square pattern at the same scale). c) Optical image after removal of the PS mask in toluene. d) Optical image after selective dissolution of the silk I regions. 44

Figure 4.2: Raman spectra of patterned silk films. a) Representative Raman spectra of Amide I and III regions of both exposed and masked regions. b) Confocal Raman mapping of silk film showing peak intensity distribution at 1250-1270 cm-1. c) Amide III peak deconvolution for masked region indicating dominating silk I secondary structure. d) Amide III peak deconvolution for exposed region indicating dominating silk II secondary structure. 46

Figure 4.3: Surface morphology of silk films before and after methanol exposure. a and b) AFM height and phase images respectively of silk film before methanol exposure (z-range 50 nm). c and d) AFM height and phase images respectively of silk film after methanol exposure (z-range 50 nm). 48

Figure 4.4: Surface morphology of patterned silk films a) AFM topography image of silk film patterned with 10 μm line pattern: 7 μm silk I and 3 μm silk II are alternating (z-range 50 nm) b) AFM topography image of silk film patterned with 3 μm checker-board pattern (z-range 50 nm). c) AFM topography image and cross section of the interface between silk I and silk II regions (z-range 30 nm). d) AFM phase image of the interface between silk I and silk II regions 49

Figure 4.5: AFM force volume (FV) measurements. a) AFM FV topography image of silk film patterned with 10 μm line pattern: 7 μm silk I, and 3 μm silk II (z-range 25 nm) b) AFM FV topography image of silk film patterned with 3 μm checkerboard pattern (z-range 15 nm). c) AFM FV surface adhesion image corresponding to the topography image shown in A. d) AFM FV surface adhesion image corresponding to the topography image shown in B. e) Surface adhesion histogram showing bimodal distribution of adhesion forces. f) Representative loading data for silk I and II regions in 10 μm line pattern. 51

Figure 5.1: Structure of responsive nanocobs a) TEM images of the nanocobs, top inset shows a low magnification view and bottom inset show a high resolution image of the Au nanoparticles on the Ag nanowire; b) HRTEM image of Au nanoparticles (inset shows Fourier transform); c) Schematic depicting how pH-triggered changes in PAA thickness lead to variable interparticle distance. 63

Figure 5.2: a) UV-Vis spectra of solutions with Au nanoparticles and Ag nanowires. b) UV-Vis spectrum of solution of bimetallic nanocobs at pH 7. c) UV-Vis spectrum of solution of bimetallic nanocobs at pH 2; d) Raman spectra of R6G adsorbed on a single nanocob at pH 2 and pH 7. 64

Figure 5.3: HRTEM analysis of bimetallic nanocobs. a) total thickness of PAA nanocoating from individual nanocobs cast from at pH 2 and pH 7. b) HRTEM images showing PAA layer on Ag nanowire at pH 7 (inset shows corresponding Fourier transform); c) and d) HRTEM images of nanocob surface at pH 2 and 7 respectively showing changes in polymer thickness and interparticle distance. 67

Figure 6.1: Segmented nanorods comprised of gold and nickel fabricated by electrodeposition in porous alumina templates. a) Schematic showing the segmented nanorods in the porous alumina template. b and c) SEM images of template cross section showing the segmented nanorods within the pores. The nanorods are comprised of gold and nickel segments with the gold appearing brighter. d) HAADF TEM images of the nanorod dimers in array 1 with gap spacings of 15, 8 and 2 nm. e-g) SEM images of the nanorod dimers in array 2 with gap spacing of 40, 20, and 8 nm. 80

Figure 6.2: Assembly of segmented nanorods according to method 1. a) Schematic depicting the uniform assembly of nanorods. 1) The nanorods are firmly embedded in thin polystyrene films at high temperature (>120 °C), 2) Selective etching of nickel segments to leave behind an array of gold dimers with precisely controlled gap size. b and c) SEM images of the nanorod arrays deposited by method 1 before and after nickel etching respectively. Images showing the full length of array 1 embedded in polystyrene. c and d) Higher-resolution images of nanorod dimers after nickel etching with 15 and 8 nm gaps between rods. 82

Figure 6.3: SEM images of nanorod dimers deposited by method 2 before and after nickel etching. a) Image showing well dispersed nanorods with relatively uniform coverage. b) The dimers remain adhered and maintain uniform coverage after etching the nickel segments. The inset image shows the consistent gap size between the dimers. 84

Figure 6.4: Optical pattern matching with SEM images was used to ensure that hyperspectral analysis was performed on single segmented nanorods. The nanorods in the a) hyperspectral dark-field image are clearly visible in the b) SEM image. 87

Figure 6.5: Hyperspectral dark-field images and unpolarized scattering spectra from arrays 1 and 2. a) High-resolution hyperspectral image of array 1. Each pixel in the image represents a scattering spectrum from 400 to 1000 nm. b) Scattering spectra corresponding to each dimer or rod shown in (a) along with integrated spectrum of a segmented nanorod (dashed line). c) Dark-field optical image of array 2 showing several arrays each consisting of 3 dimers. The color of each dimer can clearly be seen to shift from green to red as the gap size between the nanorods is reduced. d) Scattering spectra for dimers in array 2 with decreasing gap size indicating a noticeable red-shift in the longitudinal mode. e) DDA simulations of nanorod dimers showing the expected shift in the longitudinal mode. f) Comparison of the magnitude of the shift in the longitudinal mode with decreasing gap size, showing good correlation between the experimental and simulated results. 89

Figure 6.6: a) Polarized scattering for each dimer or rod in array 1. 0 and 180 degrees polarization correspond to the long axis of the dimer array (red lines), and 90 degrees polarization is perpendicular to the long axis of the dimer array (blue lines). Polarized spectra show selective excitation of the transverse and longitudinal modes with varying polarization angle. b) Dark-field optical images collected with polarized incoming light. The images show change in the predominant scattering mode from a red/orange color corresponding to the longitudinal mode excited at 0 and 180 degrees, to a green color corresponding to the transverse mode excited at 90 degrees. 91

Figure 6.7: Polar charts showing the relative intensities of the transverse (blue lines) and longitudinal (red lines) modes for each dimer or rod in array 1. 94

Figure 6.8: FDTD simulations of the effects of the tip shape on the scattering modes in uncoupled gold nanorods. a-c) Simulated spectra for nanorods with a combination of convex or concave tip shapes. Nanorods with concave tip shapes show a second transverse mode at higher energy, which was also observed in the experimental results. d) Simulated spectrum for a nanorod with a "comet-tail" like tip which resulted in a new peak appearing at 830 nm. FDTD simulations of the effects of the end tip shape on the scattering modes: 3D model of asymmetric tail along with plots of two strongest asymmetric charge distribution modes which contribute to the appearance of new long-wavelength resonance. 97

Figure 7.1: Assembly of nickel nanorods in a non-uniform orthogonal magnetic field. a) SEM image of a 200 by 800 nm nanorod; b) Illustration of a polyvinylpyrrolidone coated nickel nanorod; c) Magnetic force microscopy image showing the persistent magnetic dipole on a nanorod after removal from an external magnetic field; d) Schematic showing a cross-sectional and top-down perspective of the proposed nanorod assembly process; e-f) Optical microscopy images showing e) a well formed island imaged under dark field, f) a smaller assembly imaged under bright field with corresponding fft, g) an assembly imaged at high magnification under dark field with corresponding fft. 107

Figure 7.2: Sequence of dark field optical images showing the coarsening of labyrinth structure into discrete islands. 108

Figure 7.3: Sequence of optical images depicting islands of varying size and number of rods. 109

Figure 7.4: Tunability of lattice spacing and symmetry. a) Graph demonstrating the linear relationship between nickel nanorod volume and the equilibrium rod spacing in the assemblies. Inset images are shown (left to right) for 0.0126, 0.0251, and 0.0503 μm3 . b) Graph demonstrating the linear relationship between applied magnetic field and the equilibrium rod spacing in the assemblies. Inset images are shown (left to right) for 900, 1800, and 2700 Gauss applied field. c) Schematic showing a cross-sectional and top-down perspective of the effect of an orthogonal and non-orthogonal field on the rod assemblies. d-f) Sequential dark field optical microscopy images of rods as magnetic field is tilted and corresponding FFTs: d) orthogonal field, e and f) tilted fields. 111

Figure 7.5: Tethering of nanorod arrays to the substrate. a) Bright field optical image demonstrating the effect of removing the external field without tethering nanorods. b-d) SEM images showing tethered nanorods after external fields have been removed, b) large area view of 400 nm length rods, c) close-up image of 400 nm length rods, d) close up image of 800 nm length rods. 113

Figure 7.6: Sequential deposition of hierarchical assemblies and actuation of arrays. a) Schematic showing robust tethering process based on hydrogen-bonding between PMAA and PVPON layers. b) Darkfield optical image showing sequential deposition of two islands on the same substrate left island is comprised of 400 nm long nanorods and right-side island of 80 nm long rods. c) Darkfield images from movie S4 showing the change in scattering intensity as nanorods are actuated by an external magnetic field. 115

LIST OF SYMBOLS AND ABBREVIATIONS

ω_p	Plasma resonance frequency
ε	Relative perimittivity
I	Scattering intensity
α	Polarization anisotropy
θ	Polarization angle
H	Magnetic Field
m	Magnetic moment
M	Magnetization
LSPR	Localized Surface Plasmon Resonance
SERS	Surface Enhanced Raman Scattering
HRTEM	High Resolution Transmission Electron Microscopy
EELS	Electron Energy Loss Spectroscopy
AFM	Atomic Force Microscopy
MFM	Magnetic Force Microscopy

SUMMARY

Recently, technological advancement and the promise of next-generation devices have created an overwhelming push for the continued miniaturization of active systems to the micro- and nanometer scale. In this regime, traditional mechanical systems are largely inaccessible and as a result new active or stimuli-responsive materials are required.

The work presented in this dissertation provides an understanding of the responsive nature of polymer and biopolymer interfaces especially in contact with metal nanoparticles. This understanding was utilized in conjunction with top-down template-based and self-assembly fabrication strategies to create hybrid protein based films and active polymer-metal hybrids that exhibit large and well-defined modulation of mechanical and optical properties. These materials processing developments represent advancement in the current state of the art specifically in three major areas: 1. template-based top-down control of protein chain conformation, 2. high-throughput synthesis and assembly of strongly coupled plasmonic nanoparticles with modulated optical properties (both near- and far-field), 3. field-assisted assembly of highly mobile and non-close packed magnetic nanorods with capabilities for rapid actuation.

CHAPTER 1

INTRODUCTION

1.1 Motivation

Traditionally, the vast majority of active manmade devices have relied on mechanical systems in order to actuate changes in functional properties. Recently, technological advancement and the promise of next-generation devices have created an overwhelming push for the continued miniaturization of active systems to the micro- and nanometer scale. In this regime, traditional mechanical systems are largely inaccessible and as a result new active or stimuli-responsive materials are required. Stimuli-responsive materials undergo large and abrupt conformational changes in response to an externally applied stimulus and include materials such as shape memory alloys, liquid crystals, and responsive polymers. In this research area, a substantial effort has focused on enhancing the functionality of such responsive materials through strategic incorporation of nanoparticles to yield hybrid systems with responsive or active functionality.

Currently, nanomaterials are poised to advance a vast number of existing technologies and spur the development of new technologies that were not even imagined a short while back. Owing to their small size, nanoparticles have unique physical and chemical properties that are strikingly different from bulk materials. For example, metal nanoparticles are unique in their ability to confine electromagnetic modes through coherent oscillation of their conduction band electrons, a process known as localized surface plasmon resonance (LSPR).[1] As a result, the optical signature (absorption,

scattering, and extinction) is enhanced several fold, and is very sensitive to changes in the size and shape of particles, coupling between particles, and the surrounding dielectric medium.[2]

The strong and unique interaction of these particles with light has the potential to impact a number of developing nanotechnologies including optoelectronics, photovoltaics, near-field imaging and lithography, medical imaging and diagnostics, and chemical or biological sensing.[3,4,5] Recent research in plasmonics has led to significant progress in development of various passive plasmonic components. For example, researchers have demonstrated the ability to tune the LSPR peak of Au and Ag nanoparticles by precisely controlling the size, shape (spheres, rods, cubes, triangles, and discs), composition (alloys of varying composition), and structure (solid vs. hollow) of synthesized nanoparticles.[6] Plasmonic studies, however, have almost exclusively focused on passive devices with properties that are fixed by the nanostructure parameters.

Many applications including sensing and diagnostics require **active** control to achieve signal switching, modulation, and amplification in the generation and detection of plasmons. This can be realized if plasmonic nanostructures are hybridized with stimuli-responsive materials. To date, the vast majority of these efforts have concentrated on active control of the LSPR through controlled aggregation of nanoparticles or through changes in the surrounding dielectric medium.[7] Changes in the surrounding dielectric medium can be used to detect binding or adsorption of chemical or biological molecules on the particle surface.[8,9] However, such changes are limited in the types of stimuli that

can be used and the binding is often irreversible allowing only one time detection of the target molecules. Controlled aggregation of particles, on the other hand, can occur in response to a number of stimuli including changes in ion concentration, pH, temperature, and magnetic field. However, a major limitation is that the random character and polydispersity of the physical arrangement in the aggregated system typically results in a very weak and non-selective optical response.

In order to overcome many of these limitations, there has been a major effort to hybridize metal nanoparticles with responsive systems including ferromagnetic materials, liquid crystals and stimuli responsive polymers. In particular, stimuli responsive polymers are defined as polymers that undergo relatively large, reversible, and *abrupt* changes in macromolecular structure in response to small external changes in the local environmental conditions.[10] This change in macromolecular structure results in changes to the physical and chemical properties of the polymer and can be extended to mechanotransduction at larger length scales.

This responsive hybrid approach seeks to pair the synergistic characteristics of plasmonic nanoparticles (as an optical reporter) with stimuli responsive polymers (as a signal transduction pathway). The response scheme for this strategy is illustrated in figure 1.1. Here, a responsive polymer is used to drive reversible changes in the surrounding dielectric and in the coupling between metal nanoparticles. These changes are evidenced as colorimetric response caused by a robust amplification/modulation of the LSPR.

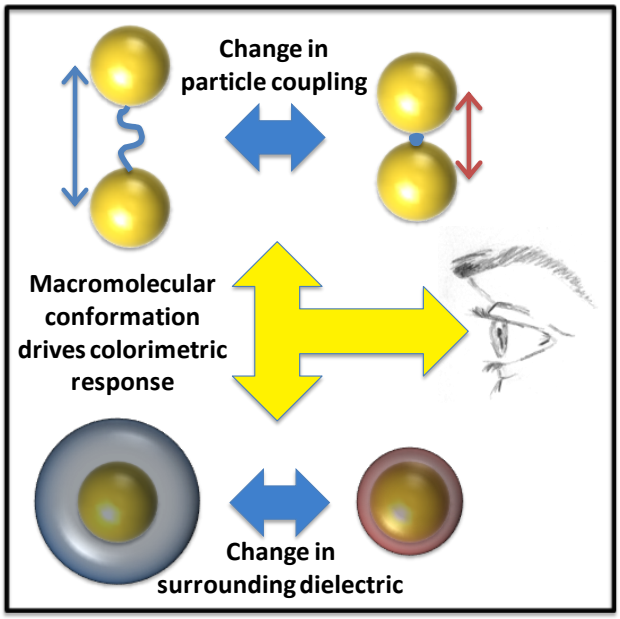

Figure 1.1 General schematic for application of responsive polymers in active plasmonic hybrids depicting colorimetric response due to change in particle coupling and surrounding dielectric

The use of responsive polymers to drive these changes has several critical advantages. First, through a rational combination of top-down and bottom-up fabrication approaches there is strong potential to create efficient active plasmonic nanostructures. Second, the tremendous diversity in polymer structures will open the door for a vast number of externally applied stimuli to be used to actively tune plasmonic properties. Finally, there is the possibility of creating multifunctional plasmonic nanostructures with multiplexed or orthogonal optical response through the coordinated use of multiple polymers. Such research efforts can help to unlock the potential of plasmonics for the improvement of real-world applications and provide insight into nanoscale phenomena that are critical for the development of active plasmonics.

Despite the tremendous potential of such active hybrid systems, there remain a number of critical materials processing challenges that present a significant hurdle towards this realization. Foremost is that the functional properties (especially far-field optical properties) of nanomaterials are critically dependent on fine nanoscale structural features. As a result fabrication techniques that allow for nanoscale resolution while maintaining cost-efficiency and high-throughput are needed. Moreover, these techniques must be compatible with downstream processing to integrate nanomaterials with stimuli-responsive materials.

1.2 Background

1.2.1 Responsive Polymers and Biopolymers

Polymers, which exhibit large, reversible, and abrupt conformational and volumetric changes in response to external stimuli, are defined as responsive polymers.[11] At the molecular level the polymer chain undergoes a coil to globule transition that is governed by a balance of attractive and repulsive forces.[12] In response to a stimulus, (which can include solvent, pH, temperature, chemical analyte, light, and electric field) the balance of forces between the chains is disrupted. If the repulsive forces dominate the polymer chains will move to the coil conformation, and if the attractive forces dominate the chains adopt a globular conformation.

The earliest responsive gels to be studied were temperature responsive polyacrylamide gels that swelled in water.[13] It was found that cooling these gels resulted in polymer-polymer interactions becoming more favorable than polymer-solvent interactions. As a

result the gels collapsed and became cloudy. Polymer systems are unique in that phase separation can occur due to either heating above a critical point, called a lower critical solution temperature (LCST), or cooling below a critical point, called an upper critical solution temperature (UCST).[14] The early polyacrylamide gels studied by Tanaka serve as good examples of UCST polymer gels.[13] Poly(N-isopropylacrylamide) (PNIPAM), poly(vinyl methyl ether), and poly(N-vinyl caprolactam) are examples of gels with LCST responsive behavior.[15] In these systems the polymer chains hydrogen bond well with water at low temperature and are swollen, however as the temperature rises to the LCST, the efficiency of hydrogen bonding decreases. The hydrophobic groups on the polymer chains then begin to interact and aggregate causing the network to expel water and collapse. PNIPAM gels have been heavily studied for biomedical applications because the LCST is in the physiologically relevant range of 32-35 °C.[16] Some of the most common applications of PNIPAM gels are for use in drug delivery, cell sheet engineering, tissue engineering, mass flow control, and dynamic optics.[15,17]

Polymer chains with weakly acidic or basic side groups can have pH responsive phase transitions.[18] For example, the protonation of the ionized acidic groups causes a decrease in the charge of the polymer chains. Subsequently, there is a decrease in the number of mobile counter ions and in the strength of electrostatic repulsions between the polymer chains. As a result the repulsive forces keeping the chain in the coil conformation diminish and the attractive forces begin to dominate causing the chain to collapse. In contrast, the deswelling phase transition in polycationic chains requires an increase in pH until the basic groups deprotonate and lose their positive charge. The phase transition

occurs in a narrow pH range close to the pKa of the acidic groups or pKb of the basic groups.[11] For example in poly(4-vinylpyridine) (P4VP) an imidazole group is protonated between pH 3-4 causing the polymer to swell at lower pH. The introduction of hydrophobic groups shifts the transition to a higher pH for acidic gels and to a lower pH for basic gels.[12]

Researchers have also synthesized a wide variety of polymers that are sensitive to other stimuli such as electric field[19], light,[20] magnetic field,[21] and chemical analyte.[22] Ultrathin gel films immersed in electrolyte were shown to swell or collapse (depending on polarity) in response to an applied voltage.[23,24] Light and magnetic field responsive polymers have been fabricated by incorporation of nanoparticles that heat the polymer through a critical temperature when exposed to high intensity light or alternating magnetic field.[25]

1.2.2 Silk Fibroin

Silk fibroin is a high molecular weight protein isolated from the cocoon fibers of the silkworm *Bombyx mori*. Fibroin represents a particularly interesting biopolymer due to its commodity level production, excellent biological and mechanical properties, and intriguing responsive properties. Fibroin is comprised of two proteins, the heavy chain (350 kDa) and the light chain (25 kDA), which are covalently linked by a disulfide bond.33 In the native fiber form, known as silk II, silk fibroin forms a high concentration of β-sheet crystallites due to the fact that the heavy chain contains a large number of hydrophobic repeat sequences of the amino acids glycine and alanine.[26] These crystallites act as physical crosslinks and greatly stabilize the protein and enhance the

mechanical properties of the fiber. However, when processed directly from aqueous solvents silk materials typically form a crank-shaft conformation as described by Lotz *et al,* known as silk I.[27] These materials are soluble or swellable in water and have a lower elastic modulus compared to silk II materials. In tissue engineering studies, it has also been found that silk I biodegrades much faster compared to silk II.[28]

Silk fibroin, can be fabricated into a wide range of cellular scaffolds including cords, fibers, films, nonwoven mats, hydrogels, and composites.[29,30,31] These silk fibroin materials have many of the biological, chemical, and mechanical characteristics that make it an attractive material for a range of modern biotechnology as well as optical and mechanical applications.[32,33,34] Silk is capable of supporting the adhesion and growth of a wide variety of mammalian cell types.32 These scaffolds retain the high modulus and outstanding toughness of silk fibers caused by multistep unfolding of hydrophobic domains.[35] The protein contains several moieties that can be covalently functionalized with biological molecules to further direct cell growth or to conduct reduction of inorganic nanoparticles for growth of natural nanocomposites. Silk fibroin scaffolds tested *in vivo* exhibit favorable biocompatibility, immunogenicity, and slow degradation characteristics in addition to outstanding mechanical properties.[36] The biological properties are a consequence of the fibroin protein's unique repetitive primary amino acid sequence and mechanically robust secondary structure.[36,37]

Of particular interest in this work, silk fibroin matrices have been shown to be responsive to external chemical, mechanical, or thermal stimuli. Fibroin materials in the silk I or

random coil conformation undergo a dramatic shift to the silk II conformation in response to exposure to methanol, strain, or heat. Moreoever this responsive nature can be enhanced as fibroin is extremely efficient in the encapsulation and immobilization of enzymes.[38,39,40] As an example, a glucose sensor was developed by encapsulating glucose oxidase in fibroin films. Here, glucose oxidase was dissolved in an aquous silk solution and cast. The film was then stretched to convert silk I to the stable silk II form, thereby immobilizing the enzyme in the matrix. Glucose oxidase immobilized in the fibroin showed greater pH and temperature stability compared to free enzyme, and the enzyme even retained activity after the films were. Moreover, very little (<0.1%) enzyme was lost even after 10 days in water.[41] The efficient encapsulation of enzymes and excellent biocompatibility make silk fibroin a valuable material for biosensing and diagnostic applications.

Another strategy for increasing the responsive behavior of fibroin materials is the direct incorporation of traditional stimuli-responsive polymers. For example, interpenetrating networks of silk fibroin and PNIPAM have been shown to result in temperature responsive materials with improved storage and loss moduli, faster deswelling kinetics, and improved biocompatibility while also maintaining a high swelling ratio.[42,43] It was proposed that the β-sheet crystallites in the silk fibroin act as crosslinks providing an increased restoring force during the deswelling process above the LCST of PNIPAM. Additionally, responsive polymers have been chemically grafted directly to the fibroin protein chain. Recently, our group has shown the layer-by-layer assembly from such conjugates with pH responsive properties enabling controlled release applications.[44]

1.2.3 Plasmonic Nanoparticles

From an electromagnetic point of view, metals are plasmas comprised of fixed positive ion cores and mobile conduction electrons. The interaction of an electromagnetic wave (comprised of an oscillating electric field) with a metal causes the free electrons to coherently oscillate at the plasma frequency (ω_p) against the immobile positive ion lattice. Due to the coulombic attraction between the electrons and nuclei, the charge redistribution provides a restoring force, causing oscillation of the electron cloud relative to the nuclei.[45] These oscillations are described as plasmons and shown in figure 1.2.

When the electrons are confined in a finite system such as a nanoparticle, the light induces electronic oscillations in the LSP. In a confined system, the surface effects dominate the bulk contribution and the LSP frequency is altered from that of the bulk metal. For example, the plasmon resonance frequency of a spherical metal nanoparticle in a vacuum is given by $\omega_p / \sqrt{3}$, where ω_p is the plasmon resonance of the bulk metal in vacuum.

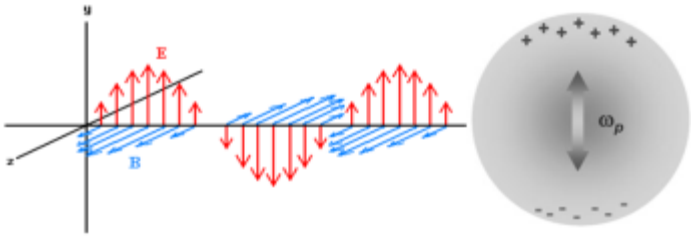

Figure 1.2 Schematic of the interaction of an EM Wave with a metal nanosphere, depicting the polarization in the direction parallel to external electric field [47]

For a nanoparticle with radius much smaller than the wavelength of the incident light (r < 5 nm, for visible light) a simple equation can be developed to describe the polarizability (a) of the particle: $a = 4\pi r^3\{[\varepsilon_1 - \varepsilon_2]/[\varepsilon_1 + 2\varepsilon_2]\}$. Here, ε_1 is the complex relative permittivity of the metal, and ε_2 is the relative permittivity of the surrounding.[46] The resonance condition is satisfied when ($Re(\varepsilon_1) = -2\varepsilon_2$). However, since the relative permittivity of metals is dependent on the frequency (or equivalently wavelength) of the incident light, the resonance condition for each metal is satisfied at a particular wavelength. For gold, silver and copper, the resonance condition is met in the visible portion of the electromagnetic spectrum.

The excitation of the LSPR results in strong light scattering and absorption.[47] The extinction (scattering + absorption) of light in the visible region imparts bright colors to metal nanoparticle suspensions. The frequency and intensity of the surface plasmon absorption bands are characteristic of the type of material and are highly sensitive to the size and shape of the nanostructures as well as to the environment around them.[48] Another factor which significantly affects the LSPR is the proximity to other nanoparticles which causes coupling of the plasmons and shift in the optical properties.[49] This particular phenomenon has been elegantly demonstrated by Yang *et al* for silver nanocrystals (Figure 1.3).[50] A monolayer of silver nanocrystals spread at the air-water interface was compressed to vary the distance between the individual nanostructures. This was accompanied by a change from a hexagonal lattice to a close-packed superlattice at the maximum pressure. Interestingly, the color of the nanocrystal film also

continuously changed with compression, which indicates a change in coupling between particles along with the decreasing interparticle spacing.

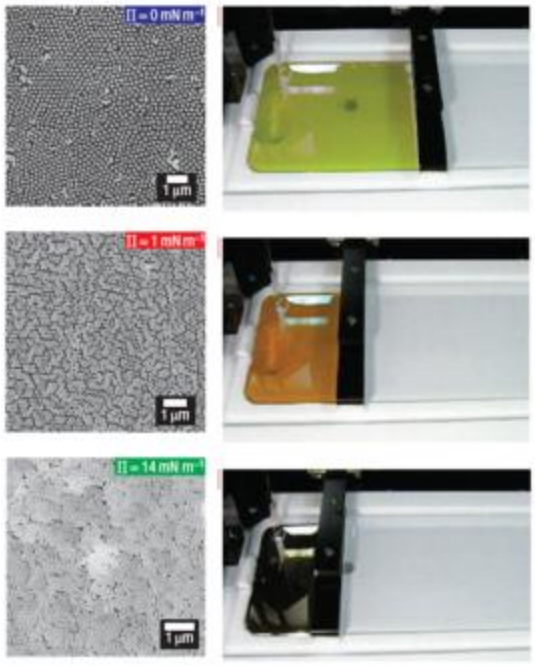

Figure 1.3 SEM images showing the packing at different surface pressures (left) and corresponding photographs of the air water interface showing the striking color change (right) [51]

Metal nanorods have been of special interest due to the fact that electron polarization can occur in two directions. Simulations and experimental results have shown that the polarization in the minor axis (transverse plasmon) is blue shifted and the polarization in the major axis (longitudinal plasmon) is red shifted relative to the spherical particle. Figure 1.4 shows the evolution of the transverse and longitudinal bands as the aspect ratio increases from a gold nanosphere to nanorod. The position of the longitudinal plasmon band is especially sensitive to changes in the aspect ratio, which can be seen in the strong shift in solution color. The combination of the strong LSPR sensitivity and the ability to

selectively couple and modulate longitudinal and transverse LSPRs makes anisotropic metal nanostructures particularly attractive for active plasmonic devices.

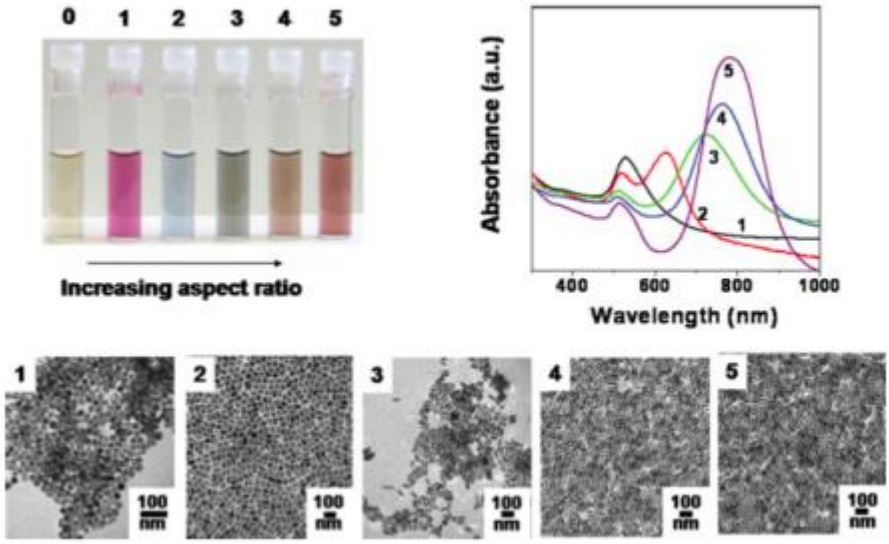

Figure 1.4 Evolution of longitudinal and transverse LSPR peaks in gold nanorods as the aspect ratio increases. Top left shows the color of the gold solutions changing as the aspect ratio of the nanorods increases as seen in the corresponding micrographs (bottom). The color change is due to evolution of the longitudingal LSPR peak (top right), which has a large absorbance and is very sensitive to the aspect ratio. [8]

1.2.4 Template-Assisted Fabrication

Metal nanoparticles have been fabricated using numerous solution, electrochemical, and vapor based approaches.[4,5] The demand for uniform nanoparticles with easy to control size and shape has made top-down template based approaches indispensable. There are many porous structures, such as colloidal masks, porous anodic alumina, track etched membranes, mica, and block copolymer films which have been and are currently being used as templates for the fabrication of metal nanoparticles.4 In this work, we will focus primarily on the use of porous anodic alumina as templates for synthesis of nanoparticles of hybrid plasmonic nanostructures.

Porous anodic alumina is another hard template that has been widely investigated for fabrication of metal nanomaterials.[4,5,46] Deposition of metal in porous anodic alumina is done through electrochemical means. The templates are commercially available in pore diameters ranging from 10-200 nm, however, commercial alumina templates tend to have irregular pore shape and branched pores (figure 1.5a). Fortunately, high quality unbranched templates can be synthesized following the two-step anodization process established by Masuda *et al* in which nanosized pores are grown through electrochemical anodization of aluminum.[51] In this process, a sheet of high-purity aluminum is first electropolished, which removes the surface oxide layer leaving behind a mirrored surface. Subsequently, the aluminum is subjected to an anodization step in an acidic electrolyte solution. The sheet is then placed in a chromic acid solution to completely remove the oxide layer grown in the first anodization. Finally, a second anodization is performed in the same acidic solution. The resulting membrane contains cylindrical pores of uniform diameter arranged in a hexagonal array with pore densities as high as 10^{11} pores per cm^2.[4]

The dimensions of the alumina templates can be tailored by altering the anodizing conditions. The pore length (template thickness) is dependent on the anodization time with longer time yielding longer pores. Pore diameters can be tailored by varying the composition and concentration of the acidic electrolyte solution, the solution temperature, and the anodization voltage. Pore diameters of 5–33 nm, 30– 70 nm, and 150–267 nm can be achieved by using sulfuric, oxalic, and phosphoric acid baths, respectively (figure 1.5b-d).[52]

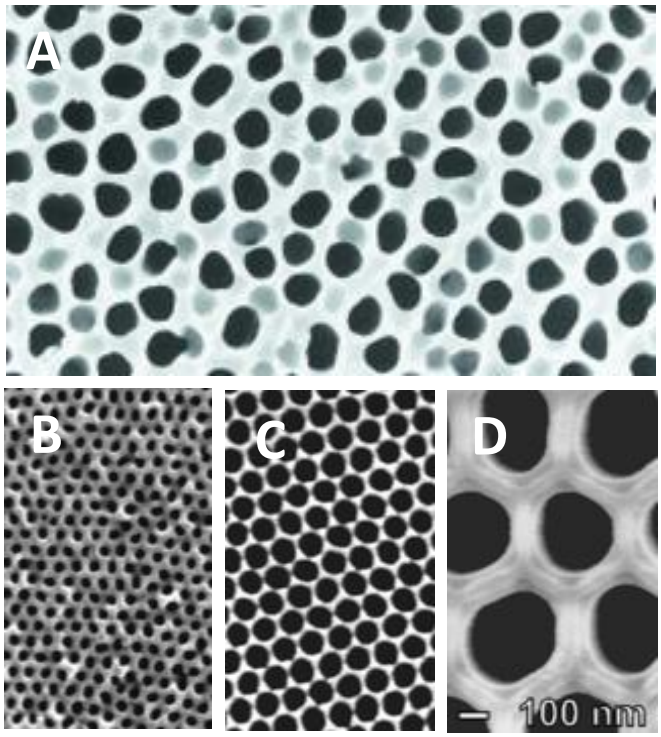

Figure 1.5 Examples of porous anodic alumina. A) Commercial anodisc from Whatman (100 nm pores); B-D)Alumina templates fabricated in sulfuric, oxalic, and phosphoric acid electrolytes respectively. [54]

Metals are most commonly deposited in porous anodic alumina using DC electrochemical deposition.4 This is accomplished by first freeing the alumina template from the underlying aluminum and creating a template with through-hole pores. A thin metal film is then sputter coated on one side of the freestanding alumina to serve as the working electrode. A wide range of metals including Au, Ag, Cu, Fe, Ni, Cr, and Pt can be deposited in this way. Additionally, metals can be alternated to create segmented rods.4 Gosele *et al* have developed a pulsed deposition technique which allows metal deposition without removing the alumina template from the underlying aluminum.[53]

1.2.5 Active Plasmonic Devices

The extremely intense and highly confined electromagnetic fields produced by the LSPR are sensitive to small spatial and chemical changes and can be tuned for metal nanomaterials. Figure 1.6 shows common strategies to actively tune the LSPR in metal nanoparticles.[54] In addition to two classical approaches discussed above, spinplasmonics and charge/discharge based approaches are able to tune the plasmonic resonance of the nanoparticle through externally applied weak magnetic and electric fields.[153] As described in the previous section, the LSPR of nanoparticles is also very sensitive to size and shape. However, this LSPR tuning typically occurs during synthesis of the nanoparticle and is not a facile strategy for actively tuning the LSPR in a device environment.[55] In this work we will focus on active plasmonics based on changes in the surrounding dielectric constant and the interparticle distance since these are properties that can be readily tuned using responsive polymer transduction pathways.

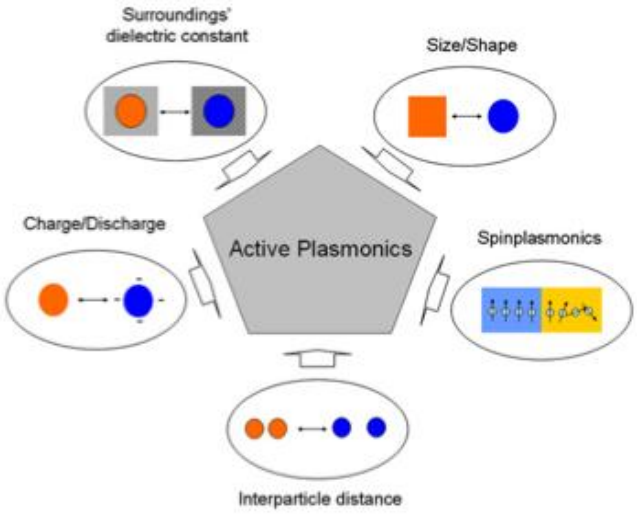

Figure 1.6 Active plasmonics schematic showing common strategies for tuning of LSPR peak in metal nanostructures. [54]

1.2.5.1 Dielectric Modulation of LSPR

The plasmon resonance frequency of the metal nanoparticles is sensitive to small changes in the local dielectric (equivalently refractive index).[56,57] In techniques such as SPR spectroscopy, which is a label-free optical detection method, a change in dielectric environment upon binding of the specific analyte at the surface of a noble metal film results in an easily detectable shift in SPR resonance.[58,59] The peak sensitivities of Au nanorods (aspect ratio of 2.2) and nanospheres correspond to shifts in the LSPR band of 366 and 76 nm per refractive index unit respectively.[60] Gold nanorod LSPR sensor substrates fabricated by self-assembly have been used for the immunospecific detection of secondary antibodies. Using a stable nanoparticle substrate and by carefully controlling the surface chemistry, the measured binding rates and equilibrium constants were similar to those obtained from the traditional SPR technique, but with much simpler instrumentation.[61]

The refractive index sensitivity of nanoprism arrays (formed by NSL) has been used to quantitatively detect and thermodynamically evaluate the binding constants of streptavidin, anti-biotin and concanavalin.[62,63,64] Nanoprism arrays were also used to detect biomarkers for Alzheimers disease.[65] Multi-arrayed sensors and high throughput LSPR assays have been utilized for the detection of protein concentration in small samples. Antibodies immobilized on each sensing spot of the array were used to detect different concentrations of their corresponding antigens as analyzed by changes in extinction spectra.[66]

Another common strategy for shifting the refractive index of the surrounding medium is to bind a molecule to the metal nanoparticles whose refractive index changes in response to an externally applied stimulus.[67] Electroactive plasmonic hybrids were made by functionalizing gold nanoparticles with the conducting polymer polyaniline. The redox state of the polyaniline was electrically switched causing a reversible shift in the refractive index of the polymer coating.[23,68] In another example, photoresponsive plasmonic devices were developed based on the cis/trans photo-isomerization of azobenzene molecules. Au nanoparticles were coated with a liquid crystal and a small amount of azobenzene was added as a guest molecule. Irradiation with 420 nm light caused an isotropic to nematic phase transition in the liquid crystal resulting in a lower refractive index and blue shift in the LSPR peak.[69,153]

1.2.5.2 Particle Coupling Modulation of LSPR

On the other hand, the particle coupling approach to active plasmonics is based on changes in color due to near-field electromagnetic coupling caused by nanoparticle aggregation. The inter-particle plasmon coupling strongly modulates the frequency of the plasmon resonance thus leading to significant changes in the optical properties.[70,71]

Colorimetric detection of analytes (physical, chemical and biological) based on particle-particle coupling is a powerful tool, owing to the excellent sensitivity and simplicity of the optical read-out. For example, assays using oligonucleotide-functionalised Au-nanoparticles exhibited strong red shift as evidenced by a striking visual color change upon aggregation in the presence of the complimentary oligonucleotide.[72] By

aggregation of nanoparticles in solution to detect biomolecular recognition events, the spectral shift in plasmon resonance can easily be observed visually or using a low-cost spectrophotometer. Nanoparticles absorb and scatter light so intensely that single nanoparticles can be observed using dark field optical microscopy and can serve as brightly colored labels in immunoassays and cellular imaging.

Resonant coupling between two metal nanoparticles linked *via* an ssDNA has been used to monitor DNA conformation changes upon hybridization.[73] Oligonucleotide-functionalized Au-nanoparticles have been used to determine the relative binding strengths of duplex and triplex DNA-binding molecules.[74] Due to the correlation that can be made between ligand binding strength and biological activity, plasmonic sensors provide new insight into the activity of anticancer drugs. Different biomolecules such as aptamers have also been combined with metal nanoparticles for high selectivity to detect adenosine and cocaine in a colorimetric disassembly process.[75] Aptamer functionalized Au nanoparticle aggregates form a 3D network that becomes unstable due to structural transformation in the aptamer in the presence of target adenosine or cocaine, leading to a color shift from purple to red. In another example, using lactose-stabilized Au-nanoparticles, cholera toxin has been detected when it binds to the derivative, inducing nanoparticle aggregation detected by a color shift from red to purple.[76] Colorimetric methods have been used for the detection of metal ions like Pb^{2+}, Cu^{2+}, Zn^{2+} or Co^{2+} by using catalytically active DNA molecules called DNAzymes.[77]

The swelling response of polymers has also been used to tune the plasmon resonance coupling of Au or Ag nanoparticles. Gold nanoparticles have been incorporated in humidity,[78] temperature,[79] and pH responsive[80] brush layers. Change in the brush conformation under external stimuli was used to tune the distance between the Au nanoparticle and Au islands patterned on the surface. The response in such systems is fairly weak and does not reflect the response range of coupled plasmonic systems.

Stimuli-responsive polymers have tremendous potential as mechanotransduction pathways in active plasmonic systems. However, they have failed to produce the shifts in the LSPR peaks that have been theoretically modeled and demonstrated experimentally. The major limitation in current approaches is that the amplitude response of the polymer systems does not drive coherent and well defined changes in particle coupling.[78,79,80]

The incorporation of stimuli responsive polymers in optically responsive nanomaterials is not trivial due to several fundamental technical challenges. First, nanoscale confinement and interfacial effects can dramatically limit the amplitude of response in polymer systems, thus suppressing their efficient signal transduction function.[81] Second, the colorimetrically reporting uniform nanoparticles must be synthesized so that the external stimulus results in a well-defined and uniform change in nanoparticle coupling and not polydisperse aggregation. Third, the responsive inorganic-organic hybrids must be carefully structured so that the isotropic response of the polymer results in an anisotropic shift to drive significant changes in the metal particle coupling. Finally, the

nanoparticle/structure's size, shape, and spacing have to be carefully selected so as to maximize the colorimetric shift.[82]

The ability to develop a comprehensive and fundamental understanding for the use of responsive polymers as a transduction pathway in active plasmonics has the potential to broaden the impact of nanotechnology in next-generation devices. Such developments would be especially critical in chemical and biological sensors, where there is a critical need for an affordable and robust sensor design that results in a single platform offering high functionality with simple and efficient signal transduction.

CHAPTER 2

RESEARCH GOALS AND OVERVIEW

2.1 Goal

The overall goal of the work presented in this dissertation is to develop a fundamental understanding for materials processing strategies that can enable spatial and temporal control of functional mechanical and optical properities in hybrid nanomaterials with nanoscale spatial precision, and to characterize the critical surface, interfacial, and nanoscale properties, which contribute significantly towards such control. In order to design efficient hybrid nanomaterials, we have considered two general fundamental questions. ***First, how do interfacial and nanoscale structural effects impact the mechanical and optical properties of nanoparticle assemblies? Second, how can template-based synthesis and field assisted assembly of nanoparticles be paired so that spatial control of properties can be manipulated over a wide range of length scales ranging from a few nanometers to hundreds of microns?***

In the proposed work this two level understanding will be accomplished through the following specific objectives:

- *Template-based strategies for permanent micropatterning of chain conformation in responsive polymer or biopolymer ultrathin films.*
- *Characterization of structure-function relationship in patterned ultrathin biopolymer films to measure nanoscale mechanical properties as a function of chain conformation.*

- *Synthesis and assembly of silver/gold core-shell bimetallic nanocob structures with a pH responsive polymeric linker to achieve switchable SERS enhancement.*
- *Structural and optical characterization of bimetallic nanocobs to elucidate impact of reversible structural changes on optical (both far- and near-field) properties.*
- *Development of template-based fabrication strategies to synthesize and efficiently assemble over large areas segmented metallic nanorods with precisely programmed nanoscale gaps to achieve tunable far-field optical properties.*
- *Single-particle optical characterization and computational modeling of assembled nanorods to study the effects of gap size, tip shape, ambient dielectric, and substrate interactions on the plasmonic coupling and far-field optical properties of nanorod assemblies.*
- *Develop magnetic field-assisted assembly techniques to create mobile arrays of nanorods with long-range order and tunable lattice symmetry and spacing.*
- *Characterize the impact of critical variables including the field strength, field orientation, nanorod magnetization, nanorod concentration, and interfacial mobility on the order, spacing, and symmetry of the nanorod arrays.*
- *Investigate materials processing strategies to sequentially manipulate the interfacial mobility of nanorods as a means to tether nanorods to the substrate surface and preserve the array structure in the absence of the external magnetic field.*
- *Demonstrate hierarchical assembly and rapid field-assisted actuation of magnetic nanorod arrays enabled by a layer-by-layer based polymeric anchor.*

The strength and novelty of this approach is that, first, a robust understanding of the responsive nature of polymers and biopolymer interfaces especially in contact with metal nanoparticles has been developed. Then this understanding was used in conjunction with top-down template-based and self-assembly fabrication strategies to create hybrid protein based films and active polymer-metal hybrids that exhibit large and well-defined modulation of mechanical and optical properties. These materials processing developments represent advancement in the current state of the art specifically in three major areas: 1. template-based top-down control of protein chain conformation, 2. high-throughput synthesis and assembly of strongly coupled plasmonic nanoparticles with modulated optical properties (both near- and far-field), 3. field-assisted assembly of highly mobile and non-close packed magnetic nanorods with capabilities for rapid actuation.

2.2 Organization and Composition of Dissertation

Chapter 1 is an analytical review of active plasmonic devices. This chapter includes a synopsis of key features of plasmonic nanoparticles, template assisted fabrication techniques, and responsive polymer systems.

This chapter, **Chapter 2**, includes a concise description of the goals and technical objectives of the work presented in this dissertation. Furthermore, it provides a brief overview of the organization of the dissertation, with brief descriptions of the contents of each chapter.

Experimental techniques that played a critical role in the studies presented in this dissertation are described in detail in **Chapter 3**. The presentation of these methods includes material fabrication processes and characterization techniques. Material fabrication processes include fabrication of porous anodic alumina templates, electrodeposition of segmented nanorods, and capillary transfer lithography. Characterization techniques include atomic force microscopy, scanning electron microscopy, hyperspectral imaging, and confocal Raman microscopy. In several subsequent chapters the experimental techniques are supplemented with specific protocols used for the particular studies presented.

Chapter 4 presents a novel and versatile approach to patterning of the secondary structure of silk films on the micrometer scale using a soft lithographic technique, as illustrated in the figure. The alternating areas of silk I and silk II structure have different mechanical, surface, and solubility properties but nominally the same chemical composition. This technique has the potential to enable the development of other tailored protein materials with selectively transformed localized secondary structure and functional properties. The study in this chapter was focused primarily on enhancing the biocompatible and mechanical functionality of hybrid biomaterials comprised solely of silk fibroin by controlling the secondary structure. In the following chapters, the focus is shifted to integration of nanomaterials in responsive polymer systems to further incorporate optical and magnetic functionality.

In **Chapter 5**, we demonstrate the pH triggered SPR and SERS properties of silver nanowires functionalized with gold nanoparticles in both solution and dry states. In contrast with previous example of such bimetallic nanocobs, here we utilize a responsive polyacrylic acid (PAA) nanocoating acting as a linker between the nanoparticles and nanowire. The pH responsive nature of the PAA nanocoating which is sensitive to the environmental pH is employed to vary the distance of separation between the gold nanoparticles and the silver nanowire and thus control plasmon coupling. Moreover, placing nanoparticles inside polymer gel layer in close proximity to the nanowire surface effectively prevents any potential aggregation of nanoparticles under variable environmental conditions in contrast with regular nanoparticle solutions which easily precipitate with changing conditions. It was found that the near-field SERS properties of the nanocobs could be triggered by pH with nearly 100 fold increase in signal enhancement. However, the response of the far-field optical properties was found to be weaker and less specific owing to the heterogeneous nature of the nanocobs. The following chapter presents a template-based strategy to synthesize plasmonic nanomaterials with precisely controlled coupling to realize fine control of far-field optical properties.

In **Chapter 6,** we developed an assembling strategy so that segmented nanorods (diameter 50 nm) fabricated through template-assisted methods can be robustly transferred and embedded in a pre-functionalized substrate with excellent uniformity over large surface areas. After embedding the rods, sacrificial nickel segments were selectively etched leaving behind strongly coupled segmented gold nanorods with gaps

between rods below 40 nm and as small as 2 nm. Hyper-spectral imaging was utilized to measure Rayleigh scattering spectra from the individual and coupled nanorod elements in contrast to common bulk measurements. This approach allows to discern the effects of not only changing segment and gap size but also the presence of characteristic defects on the plasmonic coupling between closely spaced nanorods. Polarized hyper-spectral measurements were conducted to provide direct observation of the anisotropic plasmonic resonance modes in individual and coupled nanorods which are close to those predicted by computer simulations for nanorods with ideal shapes. On the other hand, some common deviations from ideal shape such as non-flat facets and asymmetric tails were demonstrated to result in appearance of characteristic plasmon resonances which have not been considered before. The large-scale assembly of coupled noble nanostructures with fine control over geometry and high uniformity provides means to strongly tune the scattering, absorption, and near-field plasmonic properties through the geometric arrangement of precisely controlled nanorod segments.

In **Chapter 7**, we extend the versatility of the template-based segmented nanorod synthesis by presenting a simple and widely applicable approach to assemble long-range two-dimensional mobile arrays of functionalized magnetic nanorods with a tunable, unfrustrated, and 'highly-open' lattice structure. The magnetic assembly of uniformly oriented nanorods was achieved by a phase separation of the kinetically confined yet mobile vertical nanorods driven by a gradient magnetic field. The lattices can be further locked in place allowing for the removal of the applied magnetic field and processing without disrupting the initial order with different symmetries precisely assembled and

locked in their position on the same substrate. We suggest that the tunable assemblies of magnetic nanorods provide a versatile platform for downstream handling of open lattice arrays for eventual device integration.

Finally, **Chapter 8** provides general conclusions for the overall work in the dissertation with a specific focus on impact and future directions.

CHAPTER 3

EXPERIMENTAL TECHNIQUES

The following chapter is intended to provide a brief description and experimental details for the techniques and instruments used throughout this work.

3.1 Fabrication Techniques

3.1.1 Fabrication of Ultrathin Silk Films

For the preparation of ultrathin silk films, fibroin protein is purified from *B. mori* cocoons. First, cocoons are boiled for 20 min in an aqueous solution of 0.02 M Na_2CO_3 and then rinsed thoroughly with distilled water to extract the glue-like sericin proteins.[83,84] The extracted silk fibroin fibers are dissolved in 9.3M LiBr solution at 60°C for 4 h, yielding a 20% (w/v) solution. This solution is dialyzed against distilled water using Slide-a-Lyzer dialysis cassettes (MWCO 3,500, Pierce) at room temperature for 3 days to remove the LiBr. The dialysate is centrifuged three times, each at 4°C for 20 min, to remove impurities and aggregates that form during dialysis. Glass fiber syringe filters are used to filter the solution just prior to use. The final concentration of silk fibroin aqueous solution is approximately 8% (w/v). Silk films with thickness of 50-150 nm are spin coated on silicon substrates at 3000 RPM.

3.1.2 Fabrication of Layer-by-Layer Polymer Films

LBL films of pH responsive polymer are deposited using electrostatic assembly. Aqueous solutions of PMAA (1 mg/ml) and PVPON are prepared and buffered to pH 3.5

and 7.5 respectively. Precise pH buffering of the solutions is critical in order to maintain a proper ratio of charged and uncharged functional groups.

To coat metal nanorods with LBL films, 0.5 ml of PVPON is added to a 1 ml suspension of nanorods. The suspension is shaken vigorously for 5 minutes and then centrifuged at 9000 RPM for 5 minutes. The excess polymer solution is removed and the nanorods are dispersed in nanopure water adjusted to pH 7.5, brief sonication (<10 s) is used to ensure that no rod clusters remain. The nanorods are again centrifuged and the wash procedure is repeated to completely remove any unbound polymer. The PMAA layer is deposited in a similar manner with the exception of using nanopure water adjusted to pH 3.5 for wash steps. The process for depositing PVPON and PMAA is repeated to achieve the desired thickness LBL film.[85]

For deposition of LBL films on flat substrates the spin-assisted technique is used. First, 150 μl droplet of 0.2% PVPON solution is dropped on the substrate and rotated for 20 s with a 3,000 r.p.m. rotation speed. The substrate was rinsed twice with Nanopure water and dried while spinning for 30 s. In the same manner, 0.2% PMAA solution was deposited. This procedure was repeated until the needed number of polymer bilayers was achieved.[86]

3.1.3 Fabrication of Porous Anodic Alumina Templates

Porous anodic alumina templates are prepared via a two-step anodization of high purity aluminum (99.999% Goodfellow). A first long-duration oxidation and subsequent

dissolution of the formed alumina is used to create a prepatterned aluminum surface. The surface of the aluminum keeps the regular hexagonal texture that is formed during the first anodization process by self-assembly. This patterned surface acts as a nucleation point for the second anodization. After the second oxidation, an ordered nanopore array is obtained.[87]

The diameter and depth of the pores as well as the distance between them and the degree of ordering depends primarily on the anodization solution and the parameters used. Typical parameters used in this work are a 10 wt% phosphoric acid solution with anodizing potential of 150 V and temperature of 4° C or 0.3M oxalic acid solution with anodizing potential of 40 V and temperature of 15° C. These conditions typically yield 250-300 nm and 40-70 nm diameter pores respectively.[87]

Specifically the templates used in this work were fabricated by anodization of 99.999% purity aluminum foils (as-rolled, 1 mm thickness from Goodfellow Corporation). The foil was cut into 3 cm X 4 cm coupons and degreased first in acetone and then ethanol. A Keithley 2400 power supply was used to supply current and voltage for electropolishing and anodization steps. Coupons were electropolished in a solution comprised of 100 ml 60% perchloric acid solution (Alfa Aesar) and 400 ml 99.9% ethanol (caution vapor from perchloric acid can form explosive crystals!) at 7 °C by passing 1 A of current at 20 V for 15 minutes.[88] The coupons were then extensively rinsed in ethanol and dried in a nitrogen stream. Before anodization, one side of the coupons was protected with Tolber Miccro XP-2000 stop-off paint to prevent current leakage.

Anodization was performed in two stages using an aqueous 0.3 M oxalic acid (Alfa Aesar) solution at 15 °C and 40 V. The first anodization was carried out for 15 hours to create well-ordered vertically oriented pores. After the first anodization, the oxide layer was completely etched in a chromic acid solution (1.8 wt% $Cr0_3$ and 3.5 wt% H_3PO_4) at 65 °C for 2 hours. The second anodization was carried out for 6 hours to achieve the desired membrane thickness of 40 microns.

To create free-standing and through-hole membranes, the pore side of the membrane was protected by spin coating a layer of cellulose acetate from a 3 wt% solution in acetone. The remaining back side aluminum was removed in a solution of 6 g $CuCl_2$ in 75 ml 38% HCl and 75 ml water. After completely removing the aluminum, the bottom side of the pores (adjacent to the aluminum) was opened in a 1M NaOH solution for 2 minutes to yield through-hole pores. Finally, the protective cellulose acetate layer was dissolved in acetone, and the membrane was extensively rinsed in water and allowed to air dry.

3.1.4 Electrodeposition of Metals

Metal deposition was started by sputtering a 50 nm thick gold layer on the PAA template to serve as the working electrode and attached at the edge to a thin wire using conductive silver paste. A thick sacrificial nickel layer was then deposited from a commercial nickel sulfamate RTU solution (Technic Inc) by applying a -1.8 V potential using a Keithley 2400 sourcemeter for 10 minutes. This thick nickel layer served to seal the pores, allowing deposition to only occur inside the pores in the next step. The membrane was

then mounted in a custom made Teflon electrochemical cell with only the open side of the pores exposed to the electrolyte. Sequential nickel and gold depositions were carried out using commercial solutions from Technic as described above for nickel and Orotemp 24 RTU for gold. Depositions were performed at -0.9 V with respect to a saturated calomel reference electrode. A thin platinum foil was used as the counter electrode and potential was applied using a Gamry series G potentiostat. The total charge deposited was measured real-time by the potentionstat and monitored to control the lengths of the individual segments. The cell was thoroughly rinsed in between segments to remove any residual electrolyte.

After deposition, the wires were removed by first dissolving the PAA template in 1M NaOH containing 10 mg/ml PSS. Typically, a quarter of the sample area (~ 1.25 cm^2) was dissolved in 1.5 ml of KOH/CTAB solution. The segmented rods were purified by repeated centrifugation and rinsing. A total of 8 rinses were used: the initial 5 rinses were performed with 30 mg/ml CTAB solution to remove residual salt, next two rinses with water to remove excess CTAB, and finally rods were rinsed and dispersed in ethanol.

3.2 Characterization Techniques

The research involves in the application of a wide range of characterization techniques for the comprehensive study of material interfaces, mechanical, and optical properties. Most of the techniques such as scanning electron microscopy (SEM), transmission electron microscopy (TEM), optical microscopy, UV-Vis spectroscopy, are relatively

well established and will not be discussed due to the space limitation. Some of the techniques, which are specific to the current research in that they are either custom built or tailored for specific requirements, will be briefly described.

3.2.1 Atomic force microscopy (AFM)

The morphology and nanomechanical properties of various organic and inorganic surfaces with nanometer resolution will be measured using both the Dimension 3000 and the Multimode microscopes (Veeco Inc., Santa Barbara, CA). The AFM is primarily a cantilever with an ultrasharp tip that deflects when interacting with a sample surface. The deflection is measured by reflecting a laser off of the cantilever onto a photodiode position sensor that can record both normal and lateral deflection signal. The result is a three-dimensional map of the sample surface with nanometer resolution allowing for quantitative analysis of the surface roughness.[89] The topographical imaging can be performed in various modes which include contact, tapping and non-contact modes. Tapping mode AFM allows for the high resolution imaging of soft polymeric and biological samples without damage to tip or sample since contact with the surface is minimized. This is achieved by using specially designed probes that oscillate above the surface at their resonant frequencies of 100 – 500 kHz.

Force-Volume is another capability of AFM and will be used extensively in this research to map the nanomechanical properties of the sample. Surface force spectroscopy (SFS) has been shown to be a valuable tool for quantifying adhesion and elastic properties of heterogeneous surfaces of polymer layers at the nanoscale.[90, 91] This mode utilizes the

force distance curve (FDC) of the SFM.[92] A single FDC records the forces felt by the tip as it approaches to and retracts from a point on the sample surface. SFS allows collections of a square array of FDCs at unique XY coordinates over a pre-set sample area.[93] This allows for mapping of the mechanical properties (adhesion, elastic modulus) of polymer surfaces with nanometer scale resolution, while obtaining topographical information simultaneously. The applied normal load and speed of the nanoindentations are critical parameters to control in force volume to ensure that the polymer is not plastically deformed during the measurement.

3.2.2 Confocal Raman Microscopy

Protein secondary structure and SERS enhancement caused by plasmonic coupling in hybrid metal/polymer nanomaterials will be mapped using confocal Raman microscopy. The Raman scattering intensity of molecules in greatly enhanced in nanoscale gaps between plasmonic nanoparticles. It has been shown that this intensity can be tuned in hybrid systems by controlling aggregation and coupling between nanoparticles.[94] We will measure the change in SERS intensity using a WiTek (Alpha 300 R) confocal Raman microscope equipped with a Nd:Yag laser (514 nm). The Raman microscope provides a lateral resolution of ~250 nm and vertical resolution of 1μm.

3.2.3 Electron Energy Loss Spectroscopy (EELS)

A STEM equipped with EELS will be used to map surface plasmons of metal nanoparticles at nanometer resolution (in collaboration with H. Frasier (OSU) and L. Drummy (WPAFB)). The principle of STEM-EELS probing is to first position the

electron beam in an electron microscope close to the nanoparticle surface or penetrating through the nanoparticle.[95] The electromagnetic field of the incident electrons can then couple to the LSP near fields of the nanoparticles, thus polarizing them and giving rise to LSPR excitations, which result in electron energy losses. An electron beam can, therefore, excite bright LSPs by coupling primarily to their evanescent-field components close to the nanoparticle surface. This yields detailed information on the spatial distribution of LSPs. In contrast, external light can couple to bright plasmons, but it does not provide the corresponding spatial information.[96] This technique will be used to measure the spatial distribution of the LSPs in hybrid nanomaterials.

3.2.4 Single Particle Spectral Measurements

Dark-field imaging (100×) of gold nanorods was done using an Olympus BX-51 microscope and 100 W quartz halogen light source on a CytoViva microscope and software. Spectral data were captured with a CytoViva spectrophotometer and integrated CCD camera. Each spectrum shown represents a single pixel imaged with a 100× objective and approximately 64 nm in size. Samples were prepared on glass slides to allow scattering measurements to be performed in transmission mode. The sample was covered with type A immersion oil and then covered with a cover slip and sealed with nail polish to minimize disturbances. Each spectra is normalized by dividing it by a reference region (identical width, but with no particles). Spectral analysis was performed with the CytoViva Hyperspectral analysis software (ENVI) program. For polarized dark-field scattering measurements, the incident light was polarized with a linear polarizer. The direction of polarization was rotated between 0-360°.

3.2.5 Computational Modeling of Plasmonic Modulation

A critical support for the understanding of the fundamental aspects of plasmonic coupling is expected from computational efforts. The primary purpose of the computational simulations is to quantitatively optimize the structure of the plasmonic hybrids. At the same time they will provide general qualitative trends about the effect of different factors (e.g. nanoparticle, size, shape, metal type, inter-particle gap) on the plasmon resonance and field enhancement.

The optical response of gold nanorods with varying interparticle separation was calculated using the DDA method with the DDSCAT 6.1 code offered publicly by Draine and Flatau. The dielectric values for gold reported by Johnson and Christy were used and the medium surrounding the particle was represented as oil with a refractive index of 1.51.

For calculation of the scattering spectra and the surface charges distributions, we used the commercial software from Lumerical Solutions Inc. (FDTD Solutions, Version 7.5.7). The nanorod models were designed in SolidWorks (Education Edition, 2012 SP 3.0). The data were saved in the STereoLithography (STL) format and afterwards converted into a Lumerical Solutions Inc. readable file format called Graphic Database System (GDSII) format via STL2GDS from Artwork Conversion (Version 1.24). According to the GDSII data format the nanorods were sliced in 1 or 0.5nm thickness (corresponding to simulation mesh), respectively. Longitudinal and transversal modes were simulated by the corresponding polarization.

CHAPTER 4

A NOVEL FABRICATION STRATEGY FOR PATTERNING PROTEIN CHAIN CONFORMATION IN SILK MATERIALS

4.1 Introduction

The surge of interest in multifunctional high-performance materials has placed a premium on the ability of researchers to spatiotemporally pattern and control the structure and consequently functional properties of materials. Many new fields in biotechnology including tissue engineering, drug delivery, and biosensing require such control over the 2D and 3D chemical and physical properties on multiple length scales.[97,98] In tissue engineering, in order to create even very simple tissues researchers must be able to precisely control the adhesion, growth, differentiation, morphology and numerous other aspects of cell behavior. Control over cell behavior is exerted through the mechanical properties, topology, chemical cues, and the presence of other cell types in the surrounding environment. Furthermore, the surrounding environment in developing tissues is dynamic, constantly changing to meet the demands of growing cells. To design materials for this purpose a variety of synthetic and natural polymers have been explored to date.

One such material, silk fibroin, can be fabricated into a wide range of cellular scaffolds including cords, fibers, films, nonwoven mats, hydrogels, and composites.32[,99,100,101] These silk fibroin materials have many of the biological, chemical, and mechanical characteristics that make it an attractive material for a range of modern biotechnology as well as optical and mechanical applications.[102,103,104] Silk is capable of supporting the

adhesion and growth of a wide variety of mammalian cell types.32 These scaffolds retain the high modulus and outstanding toughness of silk fibers caused by multistep unfolding of hydrophobic domains.[105] The protein contains several moieties that can be covalently functionalized with biological molecules to further direct cell growth or to conduct reduction of inorganic nanoparticles for growth of natural nanocomposites.31,[106] Silk fibroin scaffolds tested *in vivo* exhibit favorable biocompatibility, immunogenicity, and slow degradation characteristics in addition to outstanding mechanical properties.[34] The biological properties are a consequence of the fibroin protein's unique repetitive primary amino acid sequence and mechanically robust secondary structure.[107,108] Beyond cellular scaffolds, enzymes have been immobilized in fibroin matrices for use in biomedical applications, and recent work by the Kaplan group has explored the use of silk fibroin in optical and microfluidic devices.[109,110,111]

As known, fibroin is comprised of two proteins, the heavy chain (350 kDa) and the light chain (25 kDA), which are covalently linked by a disulfide bond.33 In the native fiber form, known as silk II, silk fibroin forms a high concentration of β-sheet crystallites due to the fact that the heavy chain contains a large number of hydrophobic repeat sequences of the amino acids glycine and alanine.[112] These crystallites act as physical crosslinks and greatly stabilize the protein and enhance the mechanical properties of the fiber. However, when processed directly from aqueous solvents silk materials typically form a crank-shaft conformation as described by Lotz *et al*, known as silk I.[113] These materials are soluble or swellable in water and have a lower elastic modulus compared to silk II

materials. In tissue engineering studies, it has also been found that silk I biodegrades much faster compared to silk II.[114]

Silk materials (silk I and amorphous silk) can undergo an irreversible transition in secondary structure to the silk II type upon exposure to organic solvents, heat, dehydration, and mechanical strain.[115] Silk II is a partially crystalline material with nanometer-scale crystallites that shows increased elastic modulus and mechanical strength critical for demanding mechanical applications.[116,117] The rational design of nanocomposite materials and tailored surfaces which combine properties of these two different silk phases in an organized manner is an intriguing opportunity which has not been explored to date.

In this report, we present a novel strategy to selectively tune the chemical and mechanical properties of nanoscale silk fibroin materials by spatial micropatterning of the protein's secondary structure with high resolution. Furthermore, we show that the patterned silk material with alternating silk I and silk II regions retain their intrinsic chemical and mechanical characteristics and show well-developed modulation of localized properties. With this strategy, we envision the ability to fabricate structured silk materials with properties tuned in the range between silk I and silk II as well as micropatterned silk materials with highly localized regions tailored to suit particular functions. These materials will have tremendous potential for use. For example, in tissue engineering, patterned silk materials could be used to create scaffolds with uniform nominal surface chemistry and localized mechanical properties or biodegradation. This would allow

researchers tremendous flexibility in the control of cells and delivery of drugs. The ability to create tailored biocompatible materials with tunable properties in a straightforward and robust way without the use of toxic chemicals will provide additional versatility to the use of silk in biotechnology and microdevices applications.

4.2 Experimental Methods

For all experiments, 18.2 MΩcm resistivity Nanopure water was obtained from a Barnstead Nanopure system. Silk was obtained from *B. mori* silkworms raised on a diet of Silkworm Chow (Mullberry Farms, Fallbrook, CA). Live pupae were extracted from the cocoons prior to sericin removal in order to avoid contamination of the fibroin protein. Cocoons were then boiled for 20 min in an aqueous solution of 0.02 M Na_2CO_3 and then rinsed thoroughly with distilled water to extract the glue-like sericin proteins.[118,119] The extracted silk fibroin was dissolved in 9.3M LiBr solution at 60°C for 4 h, yielding a 20% (w/v) solution. The solution was dialyzed against distilled water using Slide-a-Lyzer dialysis cassettes (MWCO 3,500, Pierce) at room temperature for 3 days to remove the LiBr. The dialysate was centrifuged three times, each at -20°C for 20 min, to remove impurities and the aggregates that occurred during dialysis. The solution was filtered just prior to using glass fiber syringe filters. The final concentration of silk fibroin aqueous solution was approximately 8% (w/v).

Silicon substrates were cleaned by the standard laboratory protocol.[131] Silk films with the thickness of 100-150 nm were spin coated on silicon substrates at 3000 RPM. Sacrificial PS masks on top of silk films were obtained by use of capillary transfer lithography. For

this process, PDMS substrate was soaked in toluene for 1-2 min before a thin PS film was prepared on a PDMS substrate by spin-coating of PS 200 kDa, 2% in toluene at 3000 rpm for 20 s. A PDMS mold with the appropriate pattern was then brought into conformal contact with the PS film on the PDMS substrate and pressed for 1 min. When the PDMS mold was detached from the PDMS substrate, the patterned polymer layer was trapped inside the recessed regions of the PDMS mold. The polymer pattern formed in this way was then immediately transferred onto the silk film by conformal contact of the PDMS mold with the silk film for 1 min.

After fabrication of the PS mask the silk film was exposed to methanol vapor. Methanol vapor was formed in a crystallization dish that was equilibrated to 40^{o}C on a hot plate. The films were suspended above the dish and exposed to vapor for 20 seconds. After exposure the film was allowed to thoroughly dry for 10 minutes at ambient conditions. The PS mask layer was then removed by submerging the film in toluene for 1 minute. This was repeated to ensure complete removal of trace PS.

Optical micrographs of silk films were taken using a Leica DM 4000 microscope in brightfield and darkfield reflection modes. Film thickness was measured by spectroscopic ellipsometry (Woolam Inc). Surface force spectroscopy was conducted and surface morphology was studied by tapping mode on Dimension 3000 AFM from Digital Instruments using the established procedure.[124,129] Silk secondary structure was measured and mapped by confocal Raman microscopy using a WiTek Alpha 300R microscope with a usual procedure.[120]

4.3 Results and Discussion

The technique for patterning silk secondary structure presented here utilizes capillary transfer lithography (CTL) as a first step (Figure 7.1a).[121] By utilizing CTL we first deposited a sacrificial polystyrene (PS) mask onto a flat silk I film which was spin-cast from aqueous solution on silicon wafer (see Experimental). The masked silk I film was then briefly exposed to methanol vapor, which induced a highly localized transformation to silk II in the exposed regions without affecting other regions protected by PS mask. The PS mask was then dissolved away leaving a flat silk film with coexistent silk I and silk II regions alternating in a manner determined by the pattern of the original mask (Figure 4.1a).

The process of initial micropatterning, localized transformation, and mask removal were monitored with optical microscopy for a line pattern with spacing of 10 □m and checkerboard pattern with spacing of 3 □m (Figure 4.1). Optical micrographs show optical images of two different PS masks on a silk film (Figure 4.1b). After exposure of the masked silk I film to methanol vapor followed by removal of the mask, patterned regions can be differentiated by optical microscopy due to significant difference in the refractive properties (Figure 4.1c). Finally, exposure of the patterned silk I/silk II film to water results in selective dissolution of *only silk I regions* which confirms that masked regions of the film were not converted to silk II but preserved original silk I structure (Figure 4.1d).

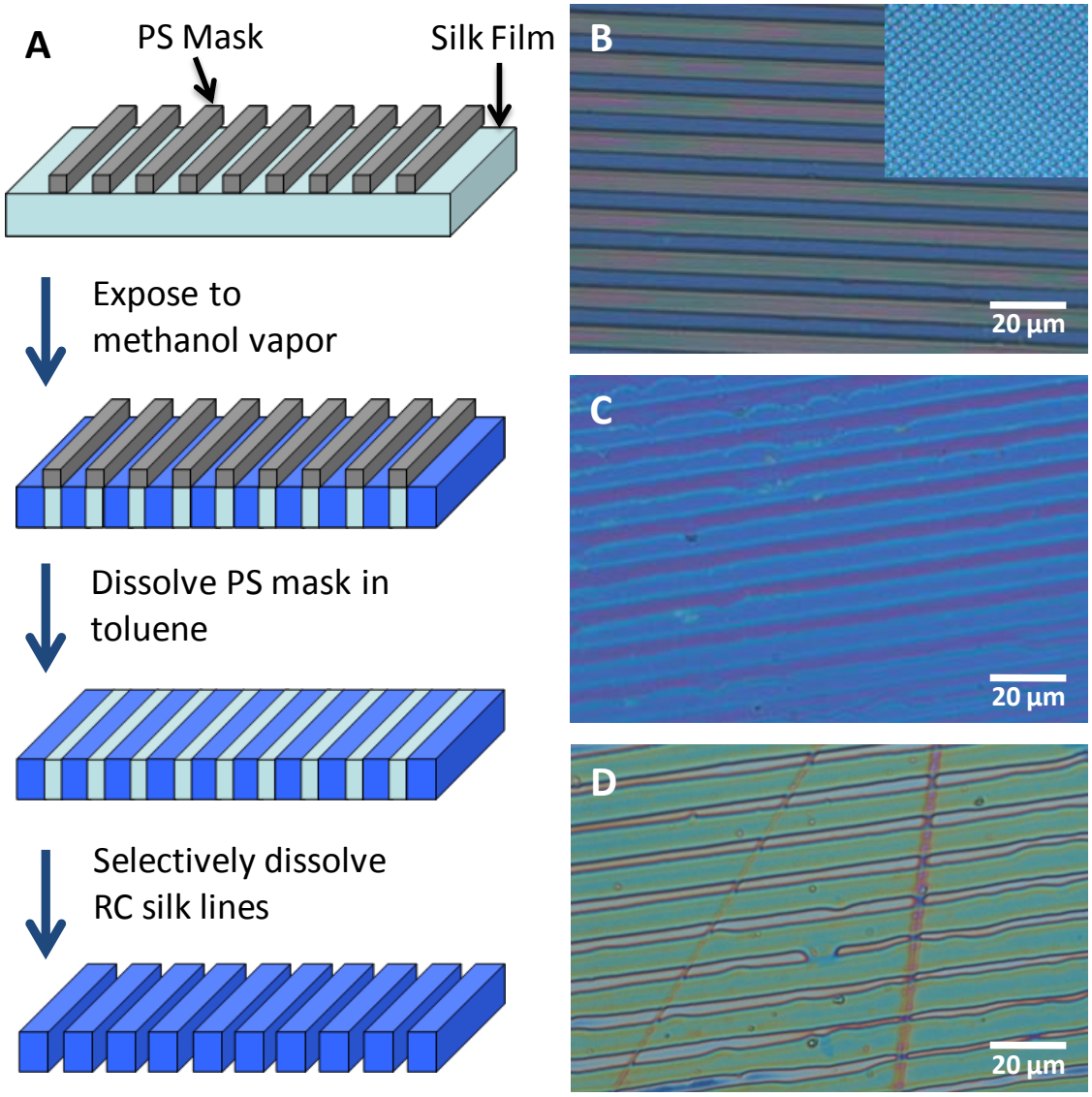

Figure 4.1: Strategy for patterning secondary structure in silk films. a) Schematic of the patterning strategy, from top to boootm. First, a PS mask is deposited on the silk film by CTL. Next, the silk film is selectively exposed to methanol vapor converting the exposed regions to silk II. Third, the PS mask is removed in toluene. Finally, the silk I regions can be selectively dissolved in water to reveal the patterning. b) Optical image of silk film with PS mask deposited on top (inset is the square pattern at the same scale). c) Optical image after removal of the PS mask in toluene. d) Optical image after selective dissolution of the silk I regions.

Various microscopic patterns of alternating silk I and silk II regions were produced by the approach described above including 10 μm periodicity line patterns and a 3 μm periodicity square pattern (Figure 4.1b inset). The size of features developed in the silk patterns is generally limited by the CTL used to deposit the mask. The resolution of the method is limited to the resolution of photolithographic master utilized for the mask deposition and molecular diffusion at the boundary region. As the size of the features decreases below 1 micron it is increasingly difficult to deposit a well-defined PS mask, instead it is more likely that a topographically patterned PS film will be deposited blocking the entire silk film below. The size of the patterned features is also dependent on the ratio of the film thickness to the smallest lateral pattern dimension. The film must be thin enough so that the methanol diffuses through the thickness of the film fast enough to avoid significant undercutting of the features. To achieve the smallest feature and highest resolution, we used 100-150 nm thick films with an 8-10 second methanol exposure, thus approaching feature sizes below 1 □m and the width of the interface between two regions of silk I and II below 100 nm (see below).

The secondary structure of the different silk regions was confirmed unambiguously by Raman spectroscopy (Figure 4.2). Indeed, Raman spectra collected separately for spatially resolved regions of the exposed and masked silk confirmed characteristic features of different silk secondary structures (Figure 4.2a). Raman spectra with the amide I peak for the masked and exposed regions at 1660 cm^{-1}, resulting from stretching modes in C=O groups, show strengthening of the peak intensity and reduction in the peak width in the exposed region compared to the masked region. This is indicative of

increased homogeneity in the β-sheet structure in silk II compared to less ordered chains in the amorphous of silk I states.[122] The aromatic peak occurring at 1617 cm^{-1} is representative of the high tyrosine content of silk fibroin.

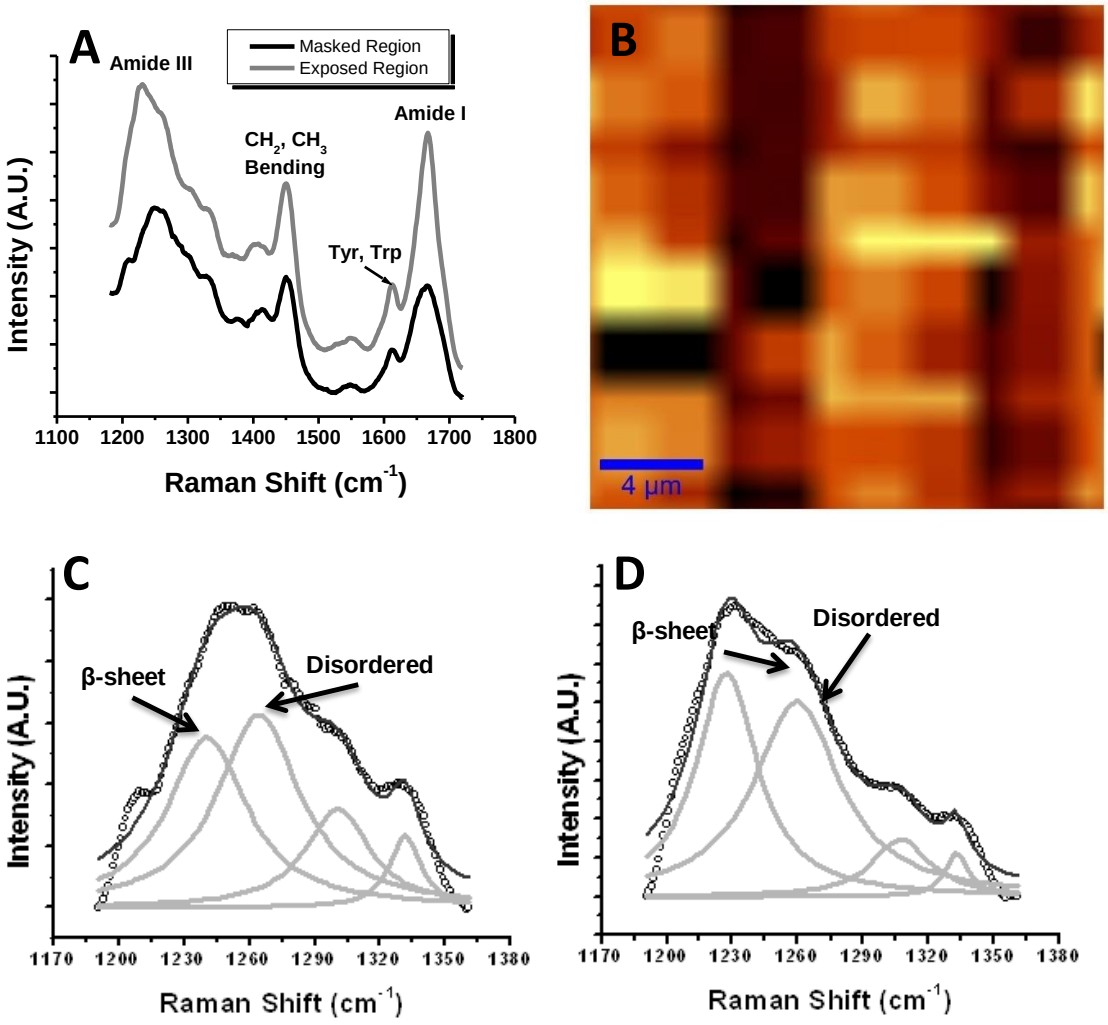

Figure 4.2: Raman spectra of patterned silk films. a) Representative Raman spectra of Amide I and III regions of both exposed and masked regions. b) Confocal Raman mapping of silk film showing peak intensity distribution at 1250-1270 cm^{-1}. c) Amide III peak deconvolution for masked region indicating dominating silk I secondary structure. d) Amide III peak deconvolution for exposed region indicating dominating silk II secondary structure.

On the other hand, the amide III region around 1230-1275 cm^{-1} is much more complex due to coupling of other modes appearing in this range with the dominant C-N-H in-plane bending and C-N stretching modes. For further analysis we conducted deconvolution of this regions with four Lorentzian peaks by following usual procedure (Figure 4.2c,d).[123] From this analysis we can conclude that the dominating peak at 1230 cm^{-1} in the spectra of exposed regions is clearly indicative of an anti-parallel β-sheet structure unambiguously confirming the transformation to silk II structure (Figure 7.2d). In contrast, the most intense peaks at 1264 cm^{-1} in the masked regions can be attributed to random coiled and α-helical secondary structures respectively confirming the preservation of silk I structure (Figure 4.2c).

Raman mapping of patterned surface shows preferential distribution of different peaks confirming localized transformation of secondary silk structure (Figure 4.2b). Indeed, confocal Raman mapping of a patterned (10 μm line spacing) silk film based upon the peak intensity integrated from 1260 to 1275 cm^{-1} shows alternating higher and lower intensities with overall spacing of 10 μm which corresponds to original patterned mask. The brighter regions correspond to 7 μm-wide silk I regions and darker regions indicate the presence of 3 μm-wide regions transformed to silk II material. The noise in the image and local variation are a result of the overall low signal level of Raman signal obtained from the ultrathin silk film. The Raman data shown here along with the selective silk dissolution mentioned above clearly indicate that we are able to pattern the secondary structure of the silk films at the micron length scale.

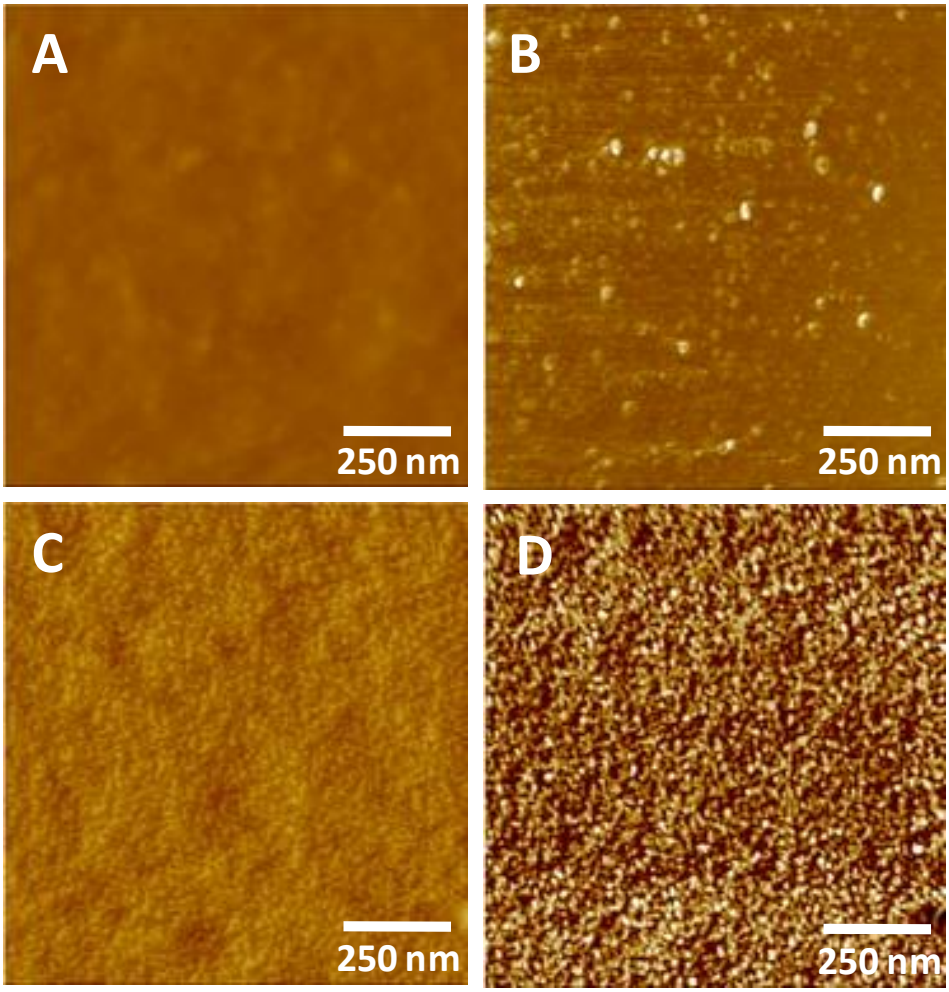

Figure 4.3: Surface morphology of silk films before and after methanol exposure. a and b) AFM height and phase images respectively of silk film before methanol exposure (z-range 50 nm). c and d) AFM height and phase images respectively of silk film after methanol exposure (z-range 50 nm).

Atomic force microscopy (AFM) of the patterned silk films revealed changes in surface morphology as a result of the transformation from silk I to silk II (Figure 4.3). Prior to methanol exposure, the silk I regions were relatively smooth with surface roughness of 1.4 nm within 1 x 1 µm (Figure 4.3a and b). However, conversion to these areas to silk II dramatically increased the surface roughness of the exposed regions to 3.1 nm due to the appearance of grainy morphology (Figure 4.3c and d). We suggest that swelling of the

native silk I film and rearrangement of the protein chains to adapt β-sheet conformation in the course of crystallization contributed to the increased roughness of the transformed regions with resulting characteristic grainy structure with dimensions of individual crystallites below 50 nm common for partially crystalline materials.[124,125]

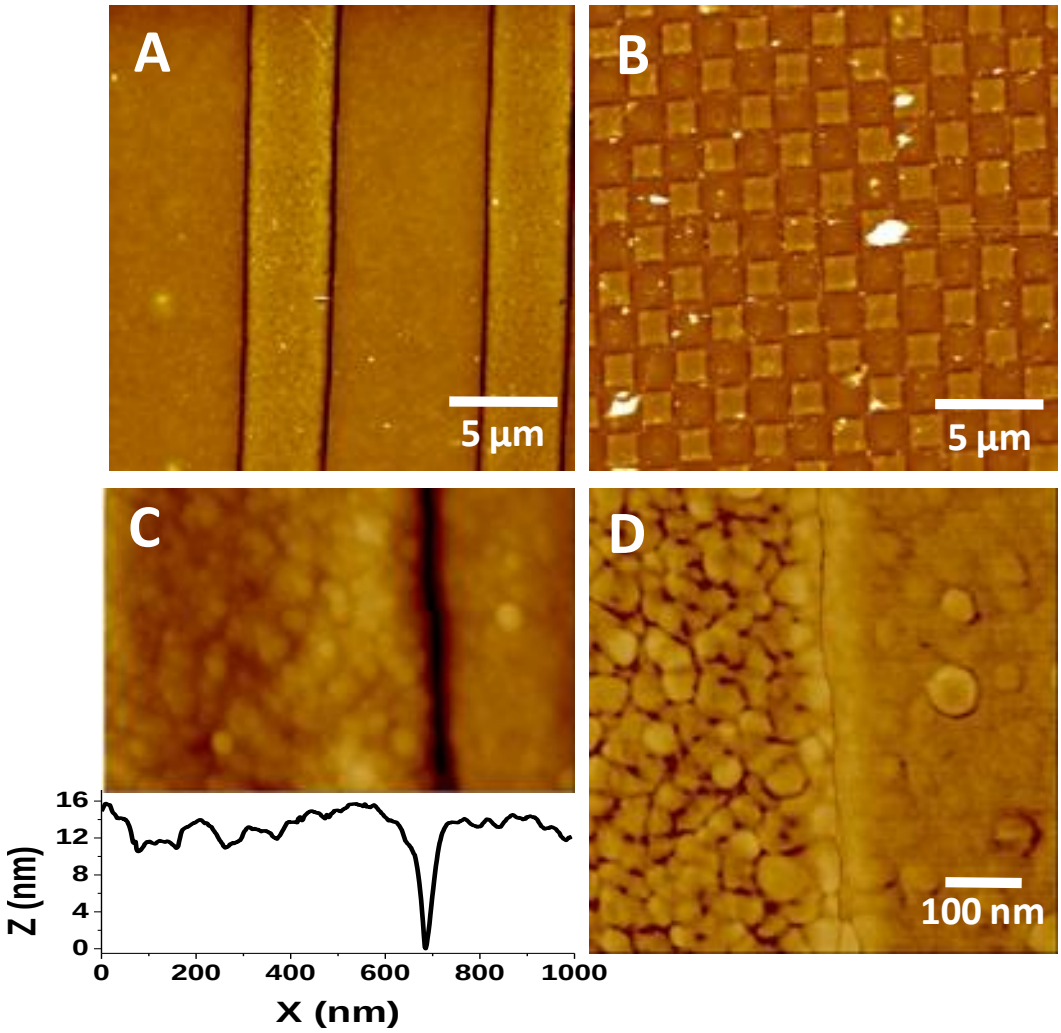

Figure 4.4: Surface morphology of patterned silk films a) AFM topography image of silk film patterned with 10 µm line pattern: 7 µm silk I and 3 µm silk II are alternating (z-range 50 nm) b) AFM topography image of silk film patterned with 3 µm checker-board pattern (z-range 50 nm). c) AFM topography image and cross section of the interface between silk I and silk II regions (z-range 30 nm). d) AFM phase image of the interface between silk I and silk II regions

AFM imaging after dissolution of the PS mask shows well-defined periodic surface topography of the patterned films (Figure 4.4). The AFM topographical image shows a 10 μm line pattern with 7 μm-wide silk I and 3 μm-wide silk II regions with some difference in elevations (Figure 4.4a). In addition, Figure 7.4b displays the AFM topographical image of a 3 μm periodic square pattern demonstrating similar differences in elevations of silk I and silk II regions each 1.5 □m wide. The surface morphologies of the silk I and II regions correspond very well with the morphology of the exposed region before and after methanol exposure respectively. The interface between silk I and silk II regions features a deep and sharp trench which is formed during the patterning process (Figure 7.4c). This is most likely caused by a decrease in free volume as the exposed regions convert to silk II causing these areas to pull away from the portion of the film that is held rigidly in place by the PS mask. High resolution phase images of the interfacial region suggest that the interface between silk I and silk II materials is very sharp with the width not exceeding 100 nm (Figure 4.4d).

Finally, AFM nanomechanical measurements were employed to directly measure the elastic modulus and surface adhesion of patterned silk films with resolution within 100-200 nm by employing force volume mode of surface force spectroscopy (Figure 7.5).[126,127,128,129] The elastic modulus of the films determined from the Hertzian contact mechanics analysis of the loading data (indentation depth vs normal load) ranged from 0.5 to 1.5 GPa, which corresponds to reported range for ultrathin silk fibroin films (Figure 4.5f).[130] However, the increased roughness of the silk II regions distorts the ability to quantitatively compare the modulus of the silk I and silk II regions.

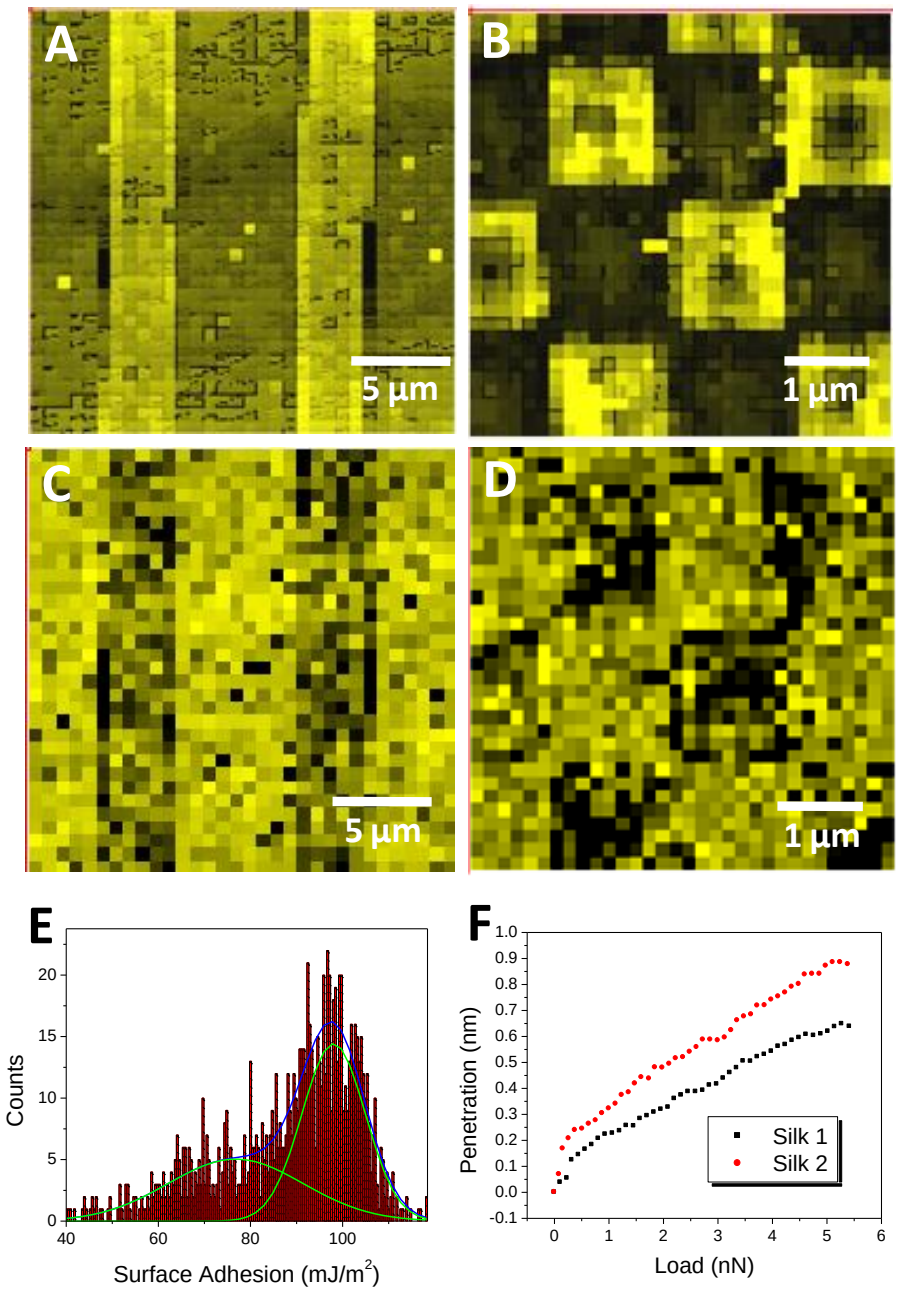

Figure 4.5: AFM force volume (FV) measurements. a) AFM FV topography image of silk film patterned with 10 µm line pattern: 7 µm silk I, and 3 µm silk II (z-range 25 nm) b) AFM FV topography image of silk film patterned with 3 µm checkerboard pattern (z-range 15 nm). c) AFM FV surface adhesion image corresponding to the topography image shown in A. d) AFM FV surface adhesion image corresponding to the topography image shown in B. e) Surface adhesion histogram showing bimodal distribution of adhesion forces. f) Representative loading data for silk I and II regions in 10 µm line pattern.

The force spectroscopy mapping, however, does clearly show that silk I regions have a higher surface adhesion (pull-off forces) as compared to silk II regions (see examples for both line and checkerboard patterns in Figure 4.5c and d). Such patterned response results in overall bimodal histogram of surface distribution with ratio of two broad contributions proportional to the fractional surface areas (Figure 4.5e). We suggest that the difference in surface adhesion between the silk I and silk II regions is caused by capillary forces between the film surface and the hydrophilic silicon probe since these measurements were conducted in air at ambient conditions.[131,132] Since the silk fibroin was dissolved in water, hydrophobic interactions will force segregation of hydrophobic amino acids to the protein core. As a result, the silk I films are likely to have surfaces dominated by hydrophilic residues with local increase in capillary-driven adhesion. On the other hand, the conversion to silk II causes the formation of β-sheets and as a result brings hydrophobic residues to the film surface thus reducing hydrophilic interactions. (Professor please add some lines per the first reviewer second comment.

4.4 Conclusion

In conclusion, we have demonstrated that the secondary structure of silk films can be patterned on the micron scale using a soft lithographic technique with high spatial resolution. The selective transformation of the silk I structure resulted in well-defined regions with very differed mechanical, surface, and solubility properties controlled by local secondary structure of silk protein. We believe that while the silk substrates used in this study were flat films, this method can be extended to other geometries. A variety of other microprinting techniques including inkjet printing, dip-pen lithography, nanosphere

lithography, and photo lithography could be used to expand the applicability of this approach to other surfaces with higher resolution and over larger areas. The patterned silk films can be prepared for liquid use by prior annealing of the films to prevent dissolution of the silk I regions. The technique can also be extended as new paradigm for patterning the chain conformation of other materials including cellulose, scaffold proteins, collagen, and lipids. In the future, this technique will allow researchers to study the properties of silk I and silk II side by side and allow for the development of tailored protein materials with nominally uniform chemical composition but selectively transformed secondary structure.

CHAPTER 5

pH TRIGGERED SERS VIA MODULATED PLASMONIC COUPLING IN INDIVIDUAL BIMETALLIC NANOCOBS

5.1 Introduction

Hybrid organic–inorganic nanostructures are a critical platform for a wide range of chemical and biological sensing applications.[133,134,135] Optical responses such as Raman scattering and absorbance serve as a signature for specific chemical groups and can be used for identification and quantification of analyte molecules.[136] Raman scattering, which is the quantized vibration signature of a molecule can be enhanced when the molecule is subjected to the enhanced electromagnetic field caused by plasmon resonance in the vicinity of plasmonic nanostructures.[137,138,139] It is well known that the plasmon absorption (resonance condition) and the electromagnetic coupling between metal nanoparticles can be tuned by external ambient, shape, dimensions, inter-particle distance, and orientation.[140,141,142] Of special interest is the coupling of surface plasmon resonances (SPR) in adjacent metal nanostructures separated by nanoscale gaps, which can modulate the optical absorption through coupling of plasmonic resonances.[143] These nanoscale gaps between plasmonic nanoparticles are also of intense interest as the formation of "hot spots" caused by the intense electric fields present in the gaps has been seen to dramatically enhance Raman scattering leading to extremely sensitive analyte detection schemes.[137,144,145, 146,147,148,149,150]

Recently, the development of active plasmonic nanostructures, which exhibit selectively and reversibly tunable optical properties, has become an intense area of interest

especially in the fields of bioimaging, as well as chemical and biological sensing.[151,152] The development of active plasmonic nanostructures has the potential to open a wide range of new possibilities beyond the simple tracking of biomolecules. For example, active plasmonic nanostructures and other quantum phenomena could be used to detect catalytic events, map chemical gradients, and changes in pH *in situ*.[153,154,155,156] This responsive behavior can be realized by functionalization of nanoparticles with active moieties such as responsive polymers which can mediate SPR coupling by changing spatial dimensions of interparticle gaps and aggregation. A number of physical phenomena which cause large dimensional changes in materials due to volume phase transformations can be utilized for design of these nanostructures.[157,158,159] Nano-structures such as metal nanoparticles and quantum dots have been widely used to track and detect biomolecules in cell, tissues, and whole organisms.[160]

To date, the vast majority of these efforts have concentrated on active control of the SPR through aggregation of nanoparticles or through changes in the surrounding dielectric medium.[161] Changes in the surrounding dielectric medium can be used to detect binding or adsorption of chemical or biological molecules on the particle surface and swelling of a grafted polymer layer in a solvent.[162,163] However, such changes are limited in the types of stimuli that can be used and binding of biomolecules is often accompanied by spontaneous and non-reversible aggregation of nanoparticles precluding quantitative analysis of the optical response.

For instance, controlled placement of nanoparticles in the vicinity of the proper surfaces was suggested by Minko et al as an efficient path to create responsive surface.[164] Zhao *et al* have demonstrated controlled temperature and light activation of aggregation as a way to modulate optical properties.[165,166] In another study, Nie *et al* have also demonstrated pH controlled aggregation of Raman encoded nanoparticles as a way to turn on and off SERS enhancement.[167] Aggregation of nanoparticles has been used recently to detect enzymatic activity of endonucleases and methyltransferases.[168] The major limitation of aggregation-based approaches is the requirement of high concentrations of nanoparticles so that aggregation can be induced. This restricts the versatility of this approach especially in cases where it is difficult to deliver high concentrations of nanoparticles. Moreover, the reliance on uncontrolled nanoparticle aggregates precludes the utilization of this phenomenon as intracellular sensing platforms.

In this chapter, we demonstrate the pH triggered SPR and SERS properties of silver nanowires functionalized with gold nanoparticles in both solution and dry states. In contrast with previous example of such bimetallic nanocobs, here we utilize a responsive polyacrylic acid (PAA) nanocoating acting as a linker between the nanoparticles and nanowire.[169] The pH responsive nature of the PAA nanocoating which is sensitive to the environmental pH is employed to vary the distance of separation between the gold nanoparticles and the silver nanowire and thus control plasmon coupling. Moreover, placing nanoparticles inside polymer gel layer in close proximity to the nanowire surface effectively prevents any potential aggregation of nanoparticles under variable

environmental conditions in contrast with regular nanoparticle solutions which easily precipitate with changing conditions.

Remarkably, this phenomenon is observed not only in the wet state (reversible changes in solution) but also under dry ambient conditions indicating that pH-induced changes in the wet PAA nanocoating are robust enough to be maintain changes in the optical properties and morphology even in dry state. To this end, high resolution transmission electron microscopy (HRTEM) employed in this work reveals that the thickness of the dry PAA nanocoating in the collapsed state is approximately equal to the width of only two polymer backbones (about 0.9 nm). Unexpectedly, even after drying in high vacuum the pH-treated, initially swollen PAA nanocoating had a thickness of 4 nm. Such dramatic morphological changes result in the appearance of broad SPRs, which is critical for the appearance of large SERS phenomenon.

5.2 Experimental Methods

All chemicals were acquired from Sigma-Aldrich, Alfa-Aesar, VWR, and Fisher and used as received without further purifications: silver nitrate salt (99.97%), poly(vinylpyrrolidone) (PVP, M_n=1,300,000 Da), Ethylene Glycol (99%), $Fe(acac)_3$, poly(allylamine hydrochloride) (PAH, 70,000 g/mol), poly(acrylic acid) (PAA, M_n=100,000 g/mol, 35 wt% solution), transparent phosphate buffer (pH 7, 0.05 M), R6G, and dimethylformamide (ACS reagent grade). Silver nanowires[170,171] and gold nanoparticles[172] were synthesized in high-yield according to standard procedures. In the procedures described below, 2 mg/mL PAA solution in pH 7 phosphate buffered solution

(0.01 M) is used for modification. All associated glassware were cleaned with aqua regia solution (3:1 HCl: HNO_3) and rinsed abundantly with Nanopure water.

5.2.1 Preparation of Bimetallic Nanocobs

A 60 mL solution of poly(vinylpyrrolidone) (PVP, 0.36 M) in ethylene glycol was heated at 160 ºC under constant stirring for one hour to remove water from the solution. Next, a separate 30 mL solution of silver nitrate in ethylene glycol ($AgNO_3$, 0.12 M) was prepared at room temperature by vigorous vortexing. Sonication or heating was avoided, since it could lead to the unwanted formation of silver nanoparticles. Next, 50 μg of Fe(acac)3 in 0.5 mL ethylene glycol solution was added into the hot PVP solution, followed by dropwise addition of the homogeneous silver nitrate solution. The drop-wise addition was done manually by means of pipette. The solution mixture was allowed to stir for a minimum of one hour, or until the solution turns opaque-gray. The formation of silver nanowires could be easily confirmed from optical microscope with 20x or 50x objectives in the dark-field mode.

A 4.1 mL aqueous solution of gold chloride ($HAuCl_4$.HCl, 30 mM) was mixed with 6.8 mL toluene solution of tetraoctylammonium bromide (TOAB, 25 mM) and vigorously stirred. As soon as all of the gold chloride salt has transferred from the aqueous phase into the organic phase, as seen from the distinctive yellow-orange color, a freshly prepared 4.1 mL ice-cold aqueous solution of sodium borohydride ($NaBH_4$, 0.4M) solution is added dropwise into the two-phase solution mixture. The solution mixture gradually turns dark purple, almost black, accompanied by vigorous bubbling. The final

solution mixture is left to stir overnight. The next day, the purple organic-phase is extracted using pipette and washed with 0.1 M sulfuric acid, followed by washing with 0.1 M sodium hydroxide, and finally washed three times with nanopure water. Equal volume of aqueous solution of 4-dimethylaminopyridine (4-DMAP, 0.1 M) is then added to the gold nanoparticles solution. Within one hour, the gold nanoparticles moved into the aqueous phase. The aqueous phase is pipetted out and separated from the organic phase to give Au:DMAP solution.

A certain amount of the methanolic solution of silver nanowires can be easily isolated from its solution by brief centrifugation at 3,300 rpm for less than five minutes. Following the centrifugation in pre-weighed centrifuge tubes the transparent supernatant is pipetted out to remove spherical nanoparticles. A typical concentration used for the subsequent procedure is 1-3 mg/mL.

To obtain negatively charged silver nanowires, 10 mg silver nanowires is mixed with cysteamine ($NH_2CH_2CH_2SH$) overnight at 1:10 mole ratio between the silver atom and cysteamine in methanol at 0.5 mg/mL concentration. The modified silver nanowires were isolated from excess ligands by multiple centrifugation-redispersion cycle in methanol. And finally, the silver nanowires are stored at pH 7 phosphate buffer solution to activate the surface charge (1 mg/mL concentration, 10-5 M phosphate buffer). Silver nanowires are dispersible in the pH 7 buffer solution when sonicated or vortexed, but gradually precipitate within 30 minutes. The silver nanowires are then redispersed in a

PAA solution (2 mg/mL, 0.01M phosphate buffer) with the aid of brief sonication and vortexing (0.5 mg/mL concentration).

The gold nanoparticles densities on silver nanowire substrates are varied as follows. To obtain a low-density gold nanoparticles, 0.1 mL solution of the as-prepared Au:DMAP solution is diluted in a 2.4 mL Nanopure water (pH 7, 2x10-3 M phosphate buffer). Next, this solution mixture is added dropwise into a stirring solution of 2.5 mL of negatively-charged silver nanowires (1 mg/mL concentration, pH 7, 2x10-3 phosphate buffer). The solution mixture is sonicated for 30 seconds and vortexed for 2 minutes to ensure uniform gold nanoparticles attachment onto the silver nanoparticles surface. Excess of unattached gold nanoparticles are then removed by centrifugation (3,300 rpm, 5 minutes). The silver nanowire-gold nanoparticles are then redispersed in a PAA solution (2 mg/mL, 0.01M phosphate buffer) with the aid of brief sonication and vortexing (0.5 mg/mL concentration). Excess of unattached PAA is removed with multiple centrifugation and redispersion cycle in Nanopure water. This is to coat the outer silver-gold nanostructure with PAA. Otherwise, the silver-gold nanoparticles are not-dispersible in water. For a high-density gold nanoparticles, 0.5 mL solution of the as-prepared Au:DMAP solution is used instead for the same amount of silver nanoparticles. Correspondingly, fivefold phosphate buffer concentration is used.

5.2.2 Characterization.

The nanocob solutions were adjusted to pH 2 by drop-wise addition of concentrated HCl. The pH of the solution was monitored using a digital pH meter. UV-Vis spectra of

nanocob solutions at pH 7 and 2 were recorded using a Shimadzu UV-2450 spectrophotometer. Samples were prepared for dry state characterization (AFM, HRTEM, and Raman) by depositing 2 µl of nanocob solution on either lacey carbon coated TEM grids or freshly piranha-cleaned silicon substrates. The solution was allowed to dry at ambient conditions. AFM topographical and phase images were obtained using a Dimension-3000 microscope in the tapping mode at 1.0-2.0 Hz scan rate, according to the usual procedure.[173,174] HRTEM images and EELS spectra were collected using a FEI Titan 300 kV microscope equipped with a Cs image corrector.

Raman spectra were collected with an Alpha300R Witek confocal Raman microscope with Argon ion laser, λ = 514.5 nm, with the incident power set below 3 mW and 20 second integration time.[175] The samples are prepared for Raman measurements by first exposing the wires to 10^{-6} M R6G at neutral pH. Excess R6G is then removed be centrifuging the nanocobs and rinsing with water. Following removal of the excess R6G, the pH of the samples was adjusted to pH 2 as described above.

5.3 Results and Discussion

The hybrid bimetallic nanocob structures used here have been prepared by a multi-step assembly of positively-charged gold nanoparticles (Au:DMAP) onto PAA coated negatively charged one-dimensional silver nanowires (Ag:COOH) as detailed above.169,[176] TEM and atomic force microscopy (AFM) images show the length of Ag nanowires to be 6$\pm$2 µm with a diameter of D=75$\pm$20 nm with aspect ratio of 80 and characteristic grainy surface morphology of bimetallic nanowires with gold nanoparticles

surrounding silver nanowire (Figure 5.1a). From HRTEM images, the diameter of spherical Au nanoparticles attached to the Ag nanowires was found to be 4.1$\pm$1 nm (Figure 1b). HRTEM images confirm the crystal structure of the Au nanoparticle with 0.23 nm corresponding the (111) lattice spacing (Figure 5.1b).[177]

The PAA nanocoating serves two important purposes in fabrication of bimetallic nanocobs. Firstly, the PAA layer stabilizes the hybrid nanostructures in the solution, which otherwise tend to form irreversible aggregates which precipitate fast. The PAA coated nanocobs are very stable in aqueous solution, however, due to the large size of the nanowires they settle due to gravitational forces after several hours. Even after settling the nanowires are easily dispersed by mild sonication. No irreversible aggregates were observed even after centrifugation of the nanocobs or storage of the samples for several months. Secondly, PAA, which is a weak anionic polyelectrolyte, imparts novel pH responsive properties to the bimetallic hybrid nanocobs (Figure 5.1c). It is well known that at neutral pH the PAA takes on a highly swollen state. Deprotonated carboxylic groups cause an influx of counter ions and hence dramatic swelling (factor of 5-10 in linear dimension) of the polymer layer.[178] But PAA coating collapses at lower pH upon protonation of carboxylic acid side group above pH 3.6.[178] Here, we suggest that this swelling-deswelling volume transition at pH 3.6 that can be used to drive the plasmonic coupling phenomena in the bimetallic nanocob (Figure 5.1c).

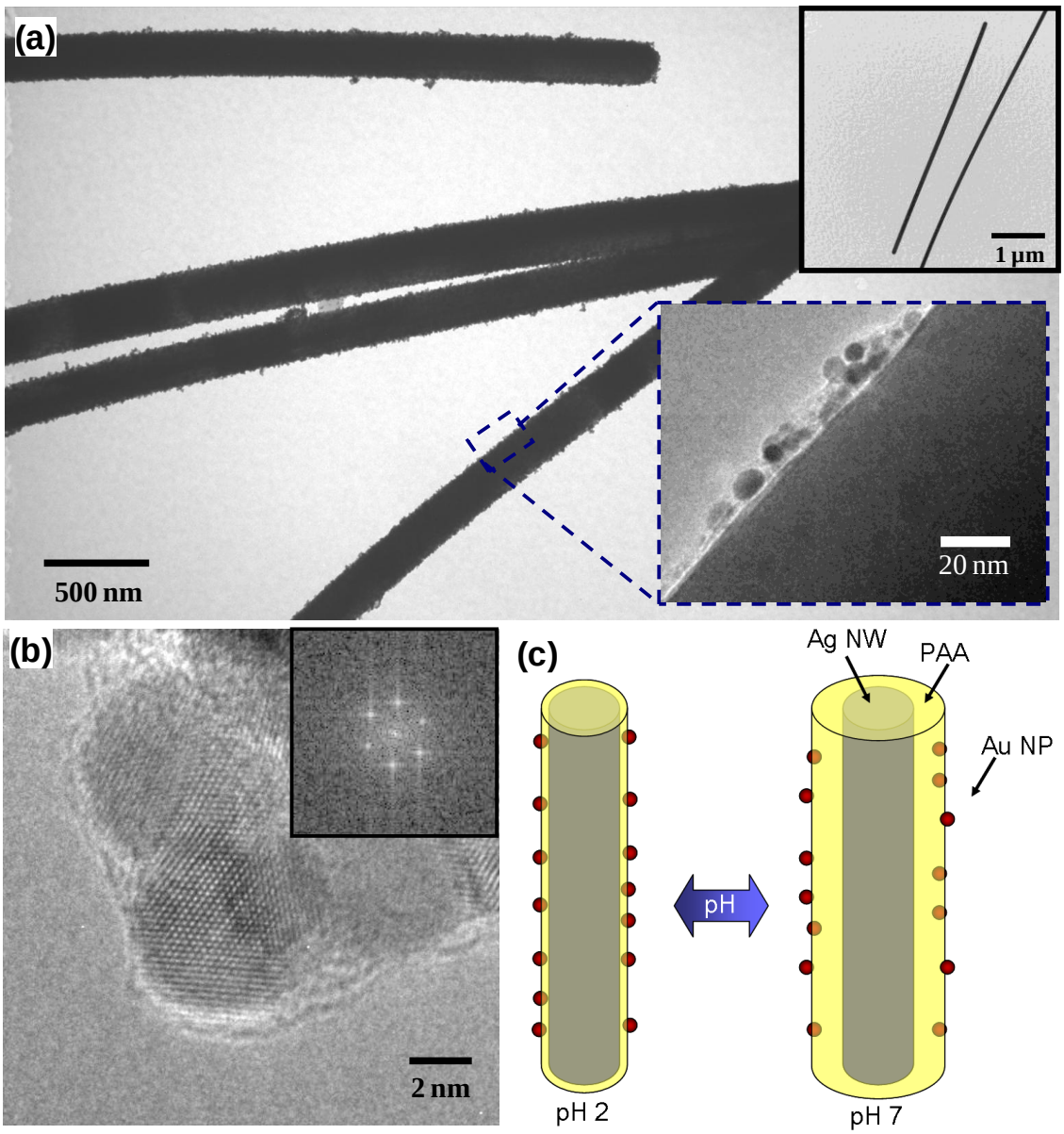

Figure 5.1: Structure of responsive nanocobs a) TEM images of the nanocobs, top inset shows a low magnification view and bottom inset show a high resolution image of the Au nanoparticles on the Ag nanowire; b) HRTEM image of Au nanoparticles (inset shows Fourier transform); c) Schematic depicting how pH-triggered changes in PAA thickness lead to variable interparticle distance.

Complex UV-Vis spectra for the assembled bimetallic nanocobs in solution reveal the presence of individual SPR peaks and variable coupling contributions at pH 2 and pH 7 (Figure 5.2). The UV-Vis spectra of the component solutions show a characteristic silver nanowires SPR peak at 390 nm and a characteristic SPR peak at 533 nm for individual gold nanoparticles (Figure 5.2a).[176] Electron energy loss spectroscopy (EELS) spectrum of adsorbed bimetallic nanocobs shows a peak at 3.3 eV corresponding approximately to a wavelength of 375 nm thus confirming intact silver surface after modification, adsorption, and drying (Figure 5.2b).

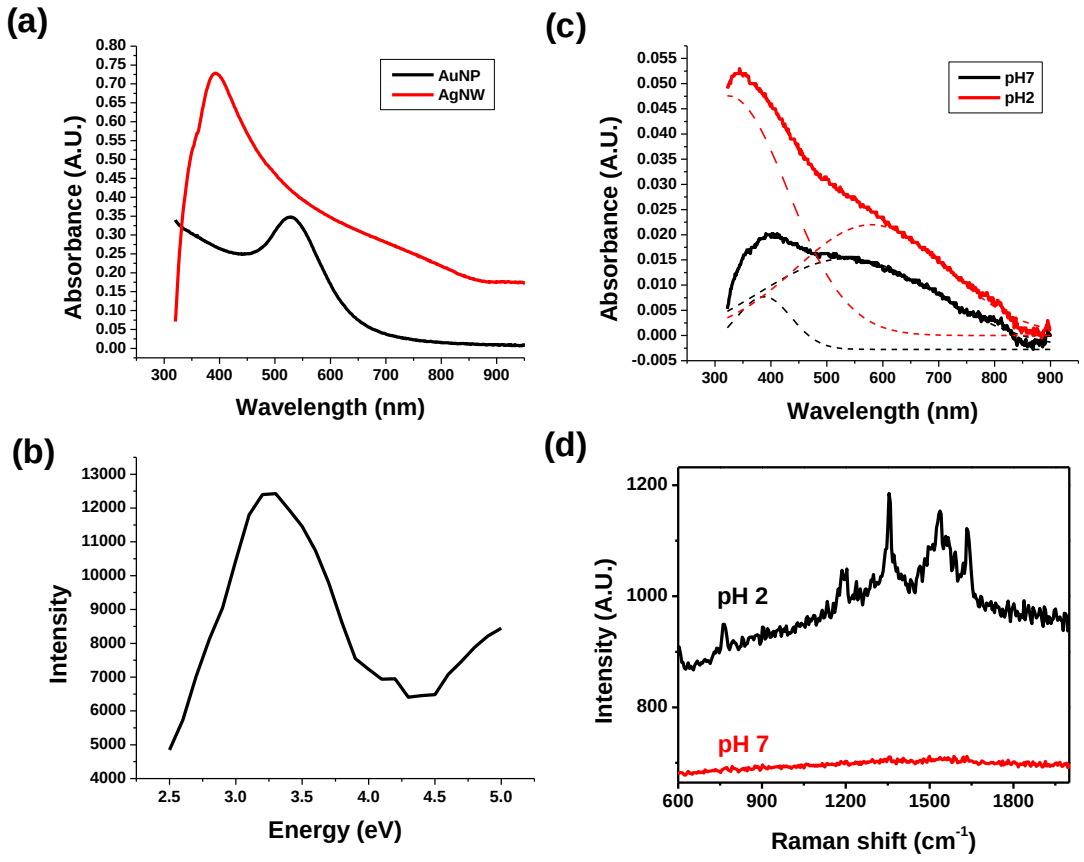

Figure 5.2. a) UV-Vis spectra of solutions with Au nanoparticles and Ag nanowires. b) UV-Vis spectrum of solution of bimetallic nanocobs at pH 7. c) UV-Vis spectrum of solution of bimetallic nanocobs at pH 2; d) Raman spectra of R6G adsorbed on a single nanocob at pH 2 and pH 7.

Deconvolution of the UV-Vis spectra for assembled nanocobs in solution clearly reveals four majors contributing peaks: first peak below 400 nm belongs to silver nanowires, second peak within 500-550 nm represents SPR for individual gold nanoparticles shows, and smaller peaks within 700-850 nm are caused by SPR resonances originated from gold-gold and gold-silver nanostructures coupling.[141,169] Comparison of UV spectra at different pH reveals a significant red-shift in the SPR peak of gold nanoparticles from 525 nm at pH 7 to 550 nm at pH 7. The SPR peak due to the coupling of gold and silver components also exhibits a red-shift from 700 to 730 nm (Figure 5.2c). Both shifts indicate increased plasmon coupling between gold nanoparticles and between gold nanoparticles and silver nanowires which causes dramatic appearance of SERS (see below). These changes can be attributed to both a variation in the surrounding dielectric caused by swelling of the PAA coating and to change in plasmon coupling between the Au nanoparticles and the Ag nanowires.

In order to verify how the observed changes in UV-Vis spectra and SERS enhancement correlate with structural reorganizations, the morphology in the vicinity of silver surfaces was monitored using HRTEM. Probing the structural changes in the ultrathin (2-5 nm) PAA nanocoating wrapped around the nanowires is extremely technically challenging. Conventional approaches for monitoring the changes in coating thickness such as ellipsometry and AFM cannot be readily applied in this case. As we find that the observed changes in the UV-Vis and SERS enhancement persist even in the dry state, it is critical to experimentally determine structural features in the dry nanocobs. Dry state

samples were prepared for HRTEM by depositing 2 µl of dilute aqueous nanocob solution at either pH 2 or pH 7 directly on lacey carbon coated TEM grids and the solution was allowed to dry at ambient conditions. Concentrated HCl was used to adjust the pH of the nanocob solution to pH 2 as measured by a digital pH meter. The pH 7 samples were deposited directly from 18.2 MΩ cm water without any additional treatment.

Indeed, HRTEM images clearly reveal dramatic changes in the morphology of the PAA nanocoating on nanocobs adsorbed from solutions with different pHs (Figure 5.3). Firstly, at acidic conditions (collapsed state) the total thickness of the PAA nanocoating was found to be 0.88 ± 0.19 nm (Figure 5.3a). In contrast, the same PAA nanocoating at pH 7 was found to be 3.95 ± 0.33 nm. It is important to note that four-fold change in the PAA thickness is observed here in highly dried state in contrast to conventional observations in wet state.[179] We suggest that very significant difference in the thickness of the PAA layer even in the dry state is due to rapid drying of the nanocobs after deposition and the maintenance of acidic pH during the deposition and drying process. Since dilute aqueous HCl solutions are known to have vapor pressures and boiling points very similar to that of pure water, it is expected that, while the local pH may vary slightly, an acidic pH below the pKa of 3.6 for PAA would be maintained throughout the drying process.

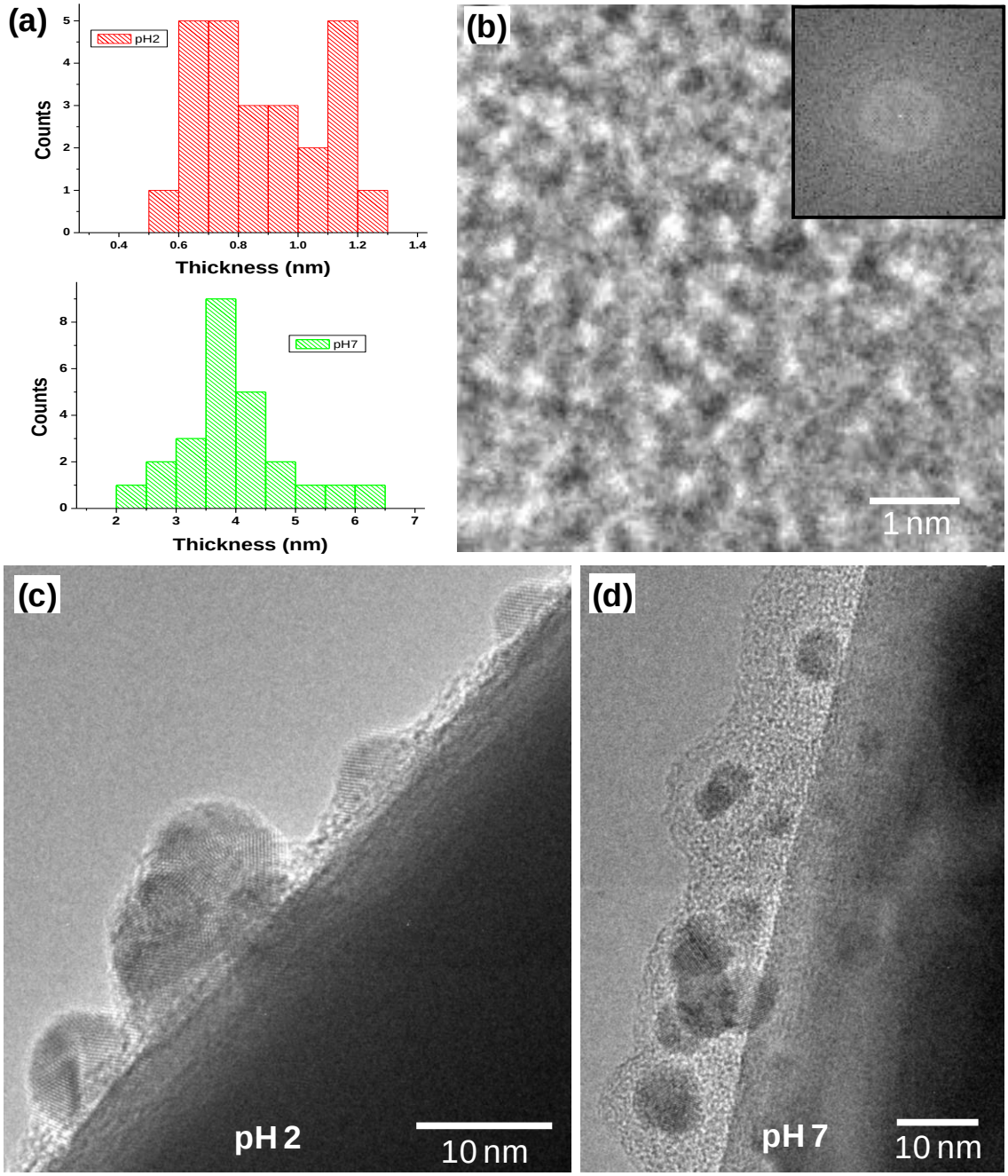

Figure 5.3. HRTEM analysis of bimetallic nanocobs. a) total thickness of PAA nanocoating from individual nanocobs cast from at pH 2 and pH 7. b) HRTEM images showing PAA layer on Ag nanowire at pH 7 (inset shows corresponding Fourier transform); c) and d) HRTEM images of nanocob surface at pH 2 and 7 respectively showing changes in polymer thickness and interparticle distance.

The internal morphology of the PAA nanocoating of silver nanowires cast from solution with different pH was revealed by HRTEM (Figure 5.3b). After drying from acidic conditions, the PAA nanocoating is highly collapsed and it is impossible to reveal the detailed morphology of collapsed polymer chains (Figure 5.3c). However, at pH 7, large PAA regions (up to 10 x 10 nm) can be found in expanded state of continuous coatings despite the fact that the specimens were in the dry state, an unexpected result even for gel materials. This expanded state allowed for observation of the molecular ordering in the swollen-dried state (Figure 5.3 b and d). The HRTEM image shows randomly varied contrast (bright and dark areas) which can be related to the presence of the amorphous PAA phase. The question of whether the observed expanded state can be associated with nanopores formation/preservation under the confined state of the nanoscale coating with embedded nanoparticles and the exact nature of the unusual phenomenon observed here remain to be elucidated. The Fourier-transform shows a diffuse halo usually arising from liquid-like, short-range molecular ordering, a characteristic of amorphous polymer phases with or without porous morphology. However, the exact location of this halo in reciprocal space is variable depending on the defocus value of the objective lens in HRTEM with further analysis required for conclusive discussion on the nature of the nanoscale morphology observed here.[180] Such local density measurements are difficult to make from local variation of phase contrast of HRTEM images of gel nanocoatings, however alternative imaging techniques to quantitatively determine local density are currently underway.

The change in the separation of gold nanoparticles and silver surface is caused by the expanded state of the PAA layer (Figure 5.3). At pH 2, the distances evaluated from HRTEM images are varied widely but stay below 1 nm indicating almost direct contact of gold nanoparticles and silver nanowires (Figure 5.3a). At pH 7, swelling of PAA layer results in many of the gold nanoparticles appearing lifted off the silver surface. The average distance between gold nanoparticles and silver surface increases to above 3 nm. We suggest that the formation of such a wide gap as compared to optimal gap size within 1-2 nm compromise the plasmon coupling and diminish the appearance of strong SERS phenomenon.[143]

To verify how reorganization of local morphology observed with HRTEM affects such critical optical properties as SERS phenomenon, a known Raman marker R6G, was employed as a model analyte (Figure 4.2d).[181,182] While the PAA polymer is also present in the metal/metal gap, the Raman scattering of R6G is much stronger than that of PAA and is dominant in the Raman spectra. Characteristic peaks from PAA that are reported in the literature are apparently not SERS-active because they do not appear in any of the spectra obtained.[183] The SERS peak assignment of R6G adsorbed on colloidal silver correspond to the literature data: 614 cm^{-1} is C-C-C ring in-plane bending; 774 cm^{-1} is C-H in-plane bending; 1,129 cm^{-1} is C-H in-plane bending, and 1,183 cm^{-1}; 1,310 cm^{-1}, 1,363 cm^{-1}, 1,509 cm^{-1}, 1,572 cm^{-1}, and 1,648 cm^{-1} are aromatic C-C stretchings.[43] Nanocob solutions were exposed to 10^{-6} M R6G at pH 7. Excess R6G was washed before the solutions were adjusted to pH 2. Raman spectra were collected from a selected surface area which includes only a single bimetallic nanocob deposited on a silicon

surface. Care was taken to ensure that the polarization direction was normal to the longa axis of the nanocob as this has been shown to have a strong influence on the intensity of SERS enhancement in coupled nanoparticle-nanowire systems.[184,185] At pH 7, the Raman spectrum for R6G has a very low intensity observed by the barely visible peaks (Figure 2d). In contrast, the Raman spectra for a single bimetallic nanocob cast from pH 2 solution shows similar R6G peaks but with increased intensity (more than two orders of magnitude) (Figure 5.2d). All peaks are sharp, well-defined, and intense thus indicating a strong SERS enhancement after PAA nanocoating collapse to a very thin (<1 nm) coating at pH 2.

5.4 Conclusion

In this chapter we have demonstrated a bimetallic hybrid nanostructure assembled from gold nanoparticles embedded into responsive PAA nanocoating around silver nanowires in which modulation of the gold-silver structural distances can serve as a chemical trigger for SERS activity. These finding are unique in that the modulation of optical Raman signal occurred without uncontrolled interparticle aggregation but only through changes in the interparticle distances within a single nanocob complex. The tunable separation distance between the two plasmonic nanostructures resulted in modulation of electromagnetic coupling and thus a dramatic change in the corresponding SERS enhancement. The observed optical properties are reversible in wet state and can be presented in the dry state.

We suggest that the ability to change optical and SERS properties of a single nanostructure is a significant advancement over the current approach involving aggregation of multiple nanoparticles by allowing measurements to be made independently of nanoparticle concentration and under robust conditions. Placing nanoparticles inside polymer gel layer in close proximity to the nanowire surface suggested here effectively prevents any potential aggregation of nanoparticles under variable environmental conditions in contrast with regular nanoparticle solutions which easily precipitate with even slight change in environmental conditions (temperature, ionic conditions, pH, and shelf time). Future directions must focus on increasing the versatility of such complexes by incorporation of polymers that are responsive to a wider array and more practically important triggers including temperature, light, electric field, and presence of chemical or biological analytes. In chapter 5 we will present an improved path for the fabrication of complexes with more homogenous morphology yielding stronger optical shifts, and systems such as nanoforests capable of multiplexed detection. Nanoparticle complexes designed with the basic principles described in this work have the potential to play a significant role in chemical and biological sensing applications that can be expanded to a wide variety of extreme environmental conditions such as in-field, long-term, intracellular or *in vivo* applications.

CHAPTER 6

UNIFORM SURFACE ASSEMBLY AND SINGLE PARTICLE MEASUREMENTS OF ANISOTROPIC PLASMONIC PROPERTIES IN STRONGLY COUPLED GOLD NANORODS

6.1. Introduction

The coupling of localized surface plasmon resonances (LSPR) in noble metal nanostructures provides a versatile approach to precisely tailor optical properties such as absorption, scattering, and near-field enhancement.[186,187,188,189,190] Recent studies have shown that nanoparticle assemblies with strongly coupled plasmons are of tremendous interest for a broad range of important applications including optoelectronics, photovoltaics, biological/chemical sensors, and nanophotonics to name a few.[191,192,193,194,195] However, the ability to precisely fabricate large numbers of monodisperse assemblies remains a significant bottleneck for their effective utilization in many emerging applications.

Top-down fabrication techniques such as electron-beam lithography have been used with tremendous success to fabricate user-defined nanoparticle arrays. These tools have been widely used to study fundamental aspects of LSPR coupling interactions such as the "plasmon ruler equation", and have more recently provided examples of Fano resonances and negative-index metamaterials in plasmonic systems.[196,197,198,199,200,201,202,203,204,205] While these tools provide users with unparalleled control over the assembly geometry, they result in polycrystalline nanoparticles, which can have significant losses, and are largely restricted by the high-cost and intricacy of the fabrication process.[206] As

described in the preceding chapter, bottom-up assembly of nanostructures, while offering advantages of single crystal structures, atomically smooth surfaces, low cost, and easy scalability, has typically been limited by the rigorous design requirements of chemical or biomolecular linkers needed to achieve diverse geometries and spacings along with the comparatively higher polydispersity among assemblies.[207,208,209,210,211,212,213,214,215,216] However, recent studies have demonstrated tremendous progress in the efforts to generalize assembly complex structures both in solution and on solid substrates.[217,218,219,220,221,222,223]

Template based strategies have been shown to provide an intermediate approach for precisely fabricating plasmonic nanostructures with a high-degree of control and in large quantities relative to conventional top-down methods.[224,225,226,227,228] In particular, porous anodic alumina (PAA) templates have proven to be extremely versatile for the fabrication of metal nanorods using both electro-less and electrodeposition methods.[229,230,231,232,233,234,235,236] Based on these techniques a number of studies have demonstrated the ability to fabricate linear arrays of nanorods with controlled diameter, length, and gap between rod segments by sequential deposition of metals followed by selective etching of sacrificial metal segments.[237,238,239,240,241,242,243,244] The strong near-field enhancement in the gaps between adjacent segments in these array structures have been thoroughly investigated especially for use in optical antenna and surface enhanced Raman scattering (SERS) applications.[245,246,247,248] These template-assisted arrays have tremendous potential for a wide range of applications including photovoltaics, electronics, and biological/chemical sensing owing to the ability precisely tailor the

geometric and compositional structure of the array along with the high-throughput and relatively low-cost of fabrication.

Current strategies for preserving the inter-rod gaps in template fabricated arrays are based on vapor phase deposition of backing layers followed by re-dispersion and then etching of sacrificial metal segments.[249] This approach serves exceptionally well for applications, such as *in situ* biosensing, where dispersible nanorod arrays are desired.[250] However, there remain numerous applications, including substrate-based sensors, photovoltaics, and optoelectronics, in which nanorod arrays are desired on fixed substrates. For these applications, high-throughput and efficient techniques to assemble these multi-segmented nanorods directly on substrates while preserving the local array structure are critical to realize the broader potential of these template-based arrays. Additionally, optical techniques capable of addressing and resolving individual array elements must be utilized to characterize the influence of structural, compositional, ambient dielectric, and substrate interaction factors on the far-field optical properties. Currently measurement of far-field optical properties in template-assisted arrays has been limited to ensemble measurements of solutions of nanorods with unpolarized light.

In this chapter, we develop materials processing strategies so that micron-long, multi-segmented nanorods with diameters as small as 50 nm, nanorod segments ranging from 70 to 150 nm, and gaps between nanorods ranging from 40 to 2 nm can be robustly transferred to a pre-functionalized substrate without compromising the original linear array structure. Hyper-spectral imaging was utilized to measure Rayleigh scattering

spectra from *the individual and coupled nanorod elements* in contrast to common bulk measurements. This approach allows one to discern the effects of not only changing segment and gap size but also the presence of characteristic defects on the plasmonic coupling between closely spaced nanorods. Polarized hyper-spectral measurements were conducted to provide direct observation of the *anisotropic plasmonic resonance modes in individual and coupled nanorods* which are close to those predicted by computer simulations for nanorods with ideal shapes. The polarized measurements also provided a means to identify scattering modes that may arise from anomalous structural features. On the other hand, some common deviations from ideal shape such as non-flat facets and asymmetric tails were demonstrated to result in appearance of characteristic plasmon resonances which have not been considered before. Simulations of ideal and roughened nanorods allowed for identification of fine structural features that may cause traditional and peculiar scattering modes observed in polarized measurements of individual nanostructures.

6.2 Experimental Methods

All chemicals were acquired from Sigma-Aldrich and VWR and used as received without further purifications. All aqueous solutions were prepared using ultrapure 18.2 MΩ*cm resistivity water obtained from a Barnstead Nanopure-UV system. Large area, free-standing, and through-hole porous alumina templates were fabricated according to procedures presented in chapter 3.

6.2.1 Template-Synthesis of Segmented Nanorods

Metal deposition was started by sputtering a 50 nm thick gold layer on the PAA template to serve as the working electrode and attached at the edge to a thin wire using conductive silver paste. A thick sacrificial nickel layer was then deposited from a commercial nickel sulfamate RTU solution (Technic Inc) by applying a -1.8 V potential using a Keithley 2400 sourcemeter for 10 minutes. This thick nickel layer served to seal the pores, allowing deposition to only occur inside the pores in the next step. The membrane was then mounted in a custom made Teflon electrochemical cell with only the open side of the pores exposed to the electrolyte. Sequential nickel and gold depositions were carried out using commercial solutions from Technic as described above for nickel and Orotemp 24 RTU for gold. Depositions were performed at -0.9 V with respect to a saturated calomel reference electrode. A thin platinum foil was used as the counter electrode and potential was applied using a Gamry series G potentiostat. The total charge deposited was measured real-time by the potentionstat and monitored to control the lengths of the individual segments. The cell was thoroughly rinsed in between segments to remove any residual electrolyte.

After deposition, the wires were removed by first dissolving the PAA template in 1M NaOH containing 10 mg/ml PSS. Typically, a quarter of the sample area (~ 1.25 cm^2) was dissolved in 1.5 ml of KOH/CTAB solution. The segmented rods were purified by repeated centrifugation and rinsing. A total of 8 rinses were used: the initial 5 rinses were performed with 30 mg/ml CTAB solution to remove residual salt, next two rinses

with water to remove excess CTAB, and finally rods were rinsed and dispersed in ethanol.

6.2.2 Immobilization of Nanorods

PS films were spin cast on freshly piranha cleaned glass or silicon substrates using a 1 wt% solution of 250,000 MW PS in toluene at 3000 rpm. The PS coated substrates were then placed on a hotplate at 150 °C and were allowed to equilibrate for 5-10 minutes. The segmented rod ethanol dispersion was then deposited dropwise on the heated substrates to embed the rods in the PS layer. Once embedded, the nickel segments were etched in 38 % HCl for 5 minutes with extensive rinsing in water afterwards to remove any residue.

6.2.3 Characterization

SEM images were collected using a Zeiss Ultra 60 FE-SEM and a Hitachi S-3400 SEM with accelerating voltage typically at 5-10 kV and working distance of 5-7 mm. Dark-field imaging (100×) of gold nanorods was done using an Olympus BX-51 microscope and 100 W quartz halogen light source on a CytoViva microscope and software. Spectral data were captured with a CytoViva spectrophotometer and integrated CCD camera. Each spectrum shown represents a single pixel imaged with a 100× objective and approximately 64 nm in size. Samples were prepared on glass slides to allow scattering measurements to be performed in transmission mode. The sample was covered with type A immersion oil and then covered with a cover slip and sealed with nail polish to minimize disturbances. Each spectra is normalized by dividing it by a reference region

(identical width, but with no particles). Spectral analysis was performed with the CytoViva Hyperspectral analysis software (ENVI) program. For polarized dark-field scattering measurements, the incident light was polarized with a linear polarizer. The direction of polarization was rotated between 0-360°.

High Angle Annular Dark Field-Scanning Transmission Electron Microscopy (HAADF-STEM) was performed on a 300 kV Cs-corrected FEI Titan. Spot size 9, a convergence angle of 7.2 mrad, and an annular detector camera length of 105 mm, and a Fischione model 3000 PMT detector were used to collect the images.

6.2.4 DDA and FDTD Simulations

The optical response of gold nanorods with varying interparticle separation was calculated using the DDA method with the DDSCAT 6.1 code offered publicly by Draine and Flatau. The dielectric values for gold reported by Johnson and Christy were used and the medium surrounding the particle was represented as oil with a refractive index of 1.51.

For calculation of the scattering spectra and the surface charges distributions, we used the commercial software from Lumerical Solutions Inc. (FDTD Solutions, Version 7.5.7). The nanorod models were designed in SolidWorks (Education Edition, 2012 SP 3.0). The data were saved in the STereoLithography (STL) format and afterwards converted into a Lumerical Solutions Inc. readable file format called Graphic Database System (GDSII) format via STL2GDS from Artwork Conversion (Version 1.24). According to the GDSII

data format the nanorods were sliced in 1 or 0.5nm thickness (corresponding to simulation mesh), respectively. Longitudinal and transversal modes were simulated by the corresponding polarization.

Simulations with an edge rounding of 4nm of the concave tip face were set to 1nm mesh size. Mesh size of the tip tail was set to 0.5nm for best possible rendering of the edges. First conformal variant was used for mesh refinement. The mesh size was stretched above the whole field source with the following x-y-z-dimensions: 200, 150 and 150nm (x-axes correspond to the longitudinal axes). All simulations were well converged below the simulation time of 75fs at an auto shutoff level of 10^{-5}. As boundary conditions perfect match layer (PML) was used. The gold permittivity was chosen from Johnson and Christy[251] and fitted by a 8 coefficient function showing an RMS error of 0.206 at a fitting range between 400 and 1000nm. The background index was chosen over the mentioned spectra according to the experimentally used oil index (1.515).[252,253]

6.3 Results and Discussion

6.3.1 Assembly of Segmented Nanorods on Surfaces

The linear nanorod arrays analyzed in this report were fabricated by sequential electrodeposition of silver, gold, and nickel metals into porous alumina templates with pore diameters of 50 nm (Figure 6.1a-c) using a thin sputter coated gold film as the working electrode. In order to facilitate high-throughput and monodisperse synthesis of the segmented nanorods, large area templates (>10 cm^2) with highly uniform pore diameters were fabricated and used.

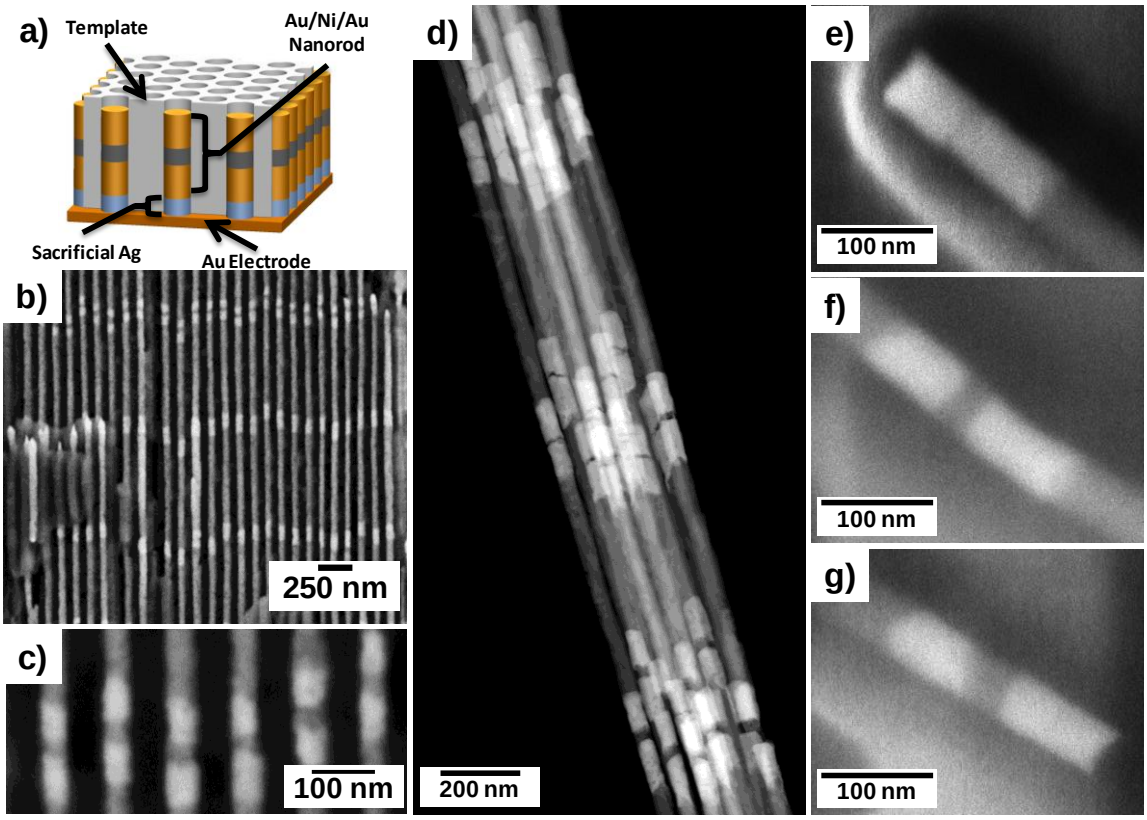

Figure 6.1: Segmented nanorods comprised of gold and nickel fabricated by electrodeposition in porous alumina templates. a) Schematic showing the segmented nanorods in the porous alumina template. b and c) SEM images of template cross section showing the segmented nanorods within the pores. The nanorods are comprised of gold and nickel segments with the gold appearing brighter. d) HAADF TEM images of the nanorod dimers in array 1 with gap spacings of 15, 8 and 2 nm. e-g) SEM images of the nanorod dimers in array 2 with gap spacing of 40, 20, and 8 nm.

A major challenge of template-based fabrication is that upon dissolution of the template a significant number of the nanorods can become "bundled" irreversibly into aggregates, significantly reducing the throughput of the synthesis. This problem is particularly severe with small diameter nanorods (<100 nm diameter) that have higher surface energy and a greater propensity to aggregate. To overcome these issues, we dissolved the alumina template in a 1M NaOH solution containing 10 mg/ml of polystyrene sulfonate

(PSS) to act as a capping layer for the rods.[254,255] Furthermore, the alumina was dissolved with the working electrode intact, and the rods were functionalized with PSS as an array. This approach kept the nanorods well separated allowing the PSS to diffuse quickly and better coat the rods. After the template was dissolved and the rods were functionalized, they were dispersed and separated from the working electrode by selectively dissolving the sacrificial silver layer. We found that this strategy was effective at creating high-yield suspensions of nanorods that were well dispersed and remained so for several months.

The lengths of the metal segments in the nanorod arrays were controlled by varying the duration of the electrodeposition. In this way, we were able to reliably deposit metal layers as thin as 2 nm. For single particle scattering measurements, two different arrays of dimers were made. In the structure of array 1, the first nanorod was 70 nm long, followed by three sets of nanorod dimers with intra-dimer gaps of 15, 8, and 2 nm between 70 nm rods (Figure 6.1d), and finally a single nanorod 140 nm in length. In the second array (array 2), nanorod dimers with gaps of 40, 20, and 8 nm were fabricated (Figures 6.1e-g). The distance between adjacent rods or dimers was maintained to be at least 500 nm to minimize LSPR coupling interactions between the adjacent array elements.

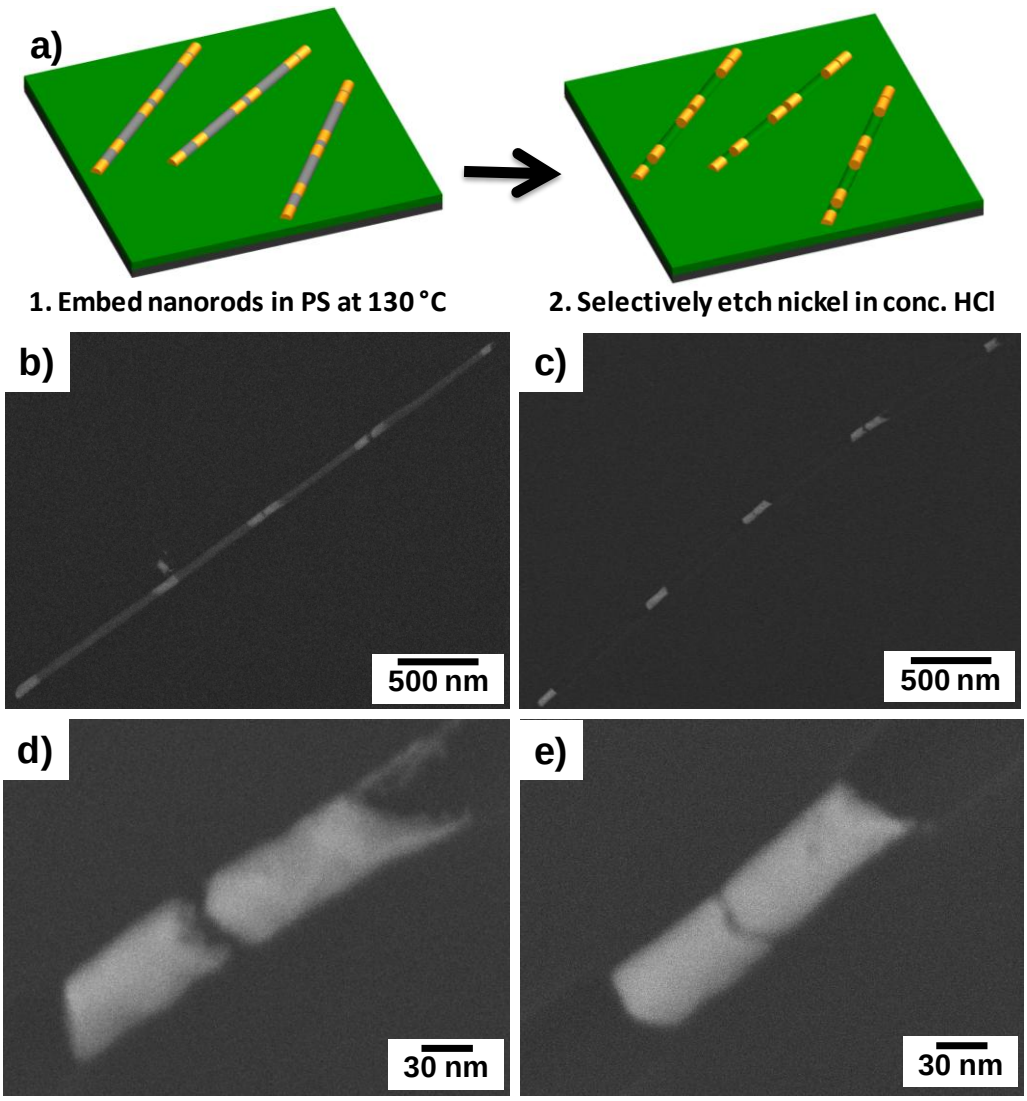

Figure 6.2: Assembly of segmented nanorods according to method 1. a) Schematic depicting the uniform assembly of nanorods. 1) The nanorods are firmly embedded in thin polystyrene films at high temperature (>120 °C), 2) Selective etching of nickel segments to leave behind an array of gold dimers with precisely controlled gap size. b and c) SEM images of the nanorod arrays deposited by method 1 before and after nickel etching respectively. Images showing the full length of array 1 embedded in polystyrene. c and d) Higher-resolution images of nanorod dimers after nickel etching with 15 and 8 nm gaps between rods.

In order to uniformly assemble the segmented nanorods directly on solid substrates while preserving the local array structure, two methods were developed. In the first method (method 1), the segmented nanorods suspended in ethanol were drop-cast on 70 nm thick

polystyrene films at elevated temperature, allowing for immediate embedding of nanorods in the pre-melted polymer coating (Figure 6.2a). This routine is a critical step in the process that served several major purposes. First, at temperatures above the glass transition of the polystyrene (>110°C) the deposited rods became partially embedded in the softened film and were frozen in place upon subsequent fast cooling. Second, this procedure immobilizes the rods and allows selective etching of nickel segments in hydrochloric acid with preservation of the original array geometry and without disturbing the nanoscale dimensions of gaps between the rods (Figure 6.2b-e). Finally, the elevated temperature resulted in nearly instantaneous drying of the ethanol, and hence largely prevented capillary induced aggregation of the segmented rods, a common challenge for conventional drop-casting.

This method worked very well to firmly embed the nanorods and preserve the nanoscale gaps after etching the nickel segments. However, due to the transient nature of the deposition at high temperature, it was difficult to uniformly cover large area substrates with the segmented nanorods. Another challenge with this method was the difficulty in precisely controlling the distance between the rods and the substrate. With 70 nm thick polystyrene films, the rods were partially embedded in the polymer film and typically 20-30 nm above the substrate surface. In order to reduce this distance, we tried to embed the nanorods in thinner films. However, this led to dewetting of polymer films around the segmented rods and significant aggregation. Finally, while the polystyrene film was robust enough to withstand harsh aqueous solutions (38% aqueous HCl), exposure to

organic solvents or high temperatures after removal of the nickel segments led to swelling or softening of the polymer film and significantly disrupted the array structure.

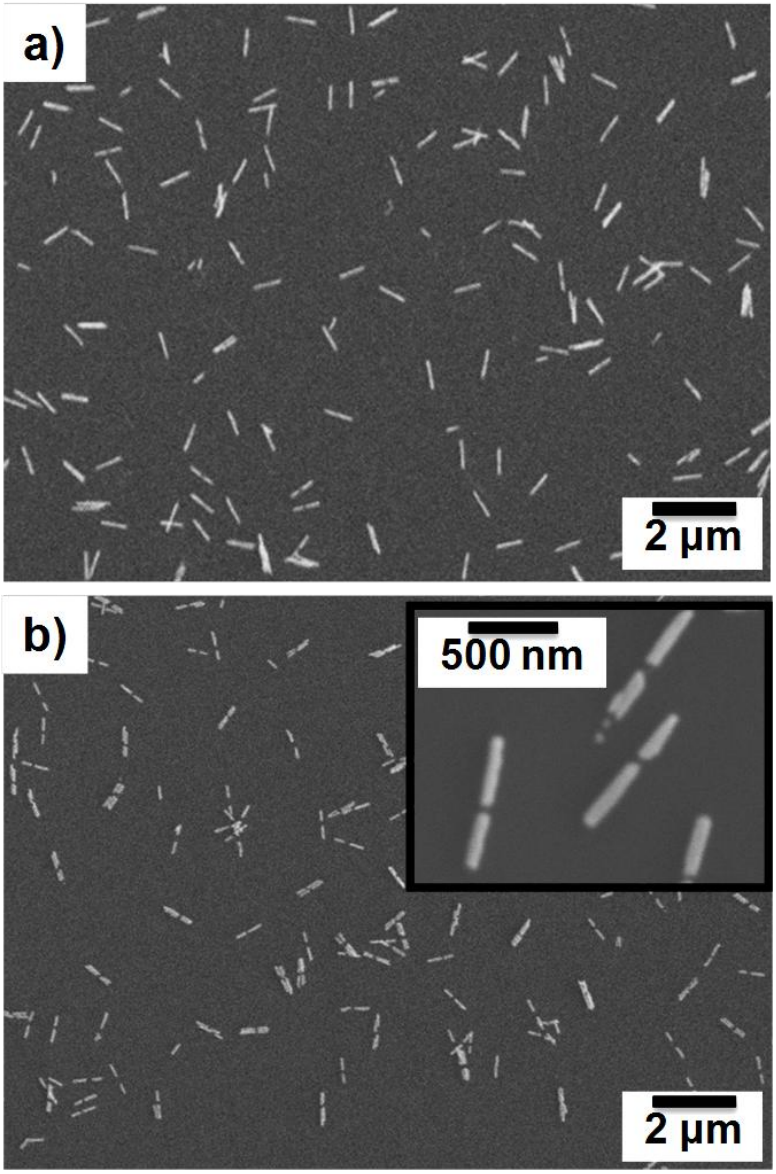

Figure 6.3: SEM images of nanorod dimers deposited by method 2 before and after nickel etching. a) Image showing well dispersed nanorods with relatively uniform coverage. b) The dimers remain adhered and maintain uniform coverage after etching the nickel segments. The inset image shows the consistent gap size between the dimers.

As a further improvement, we developed a second method (method 2) to immobilize the nanorod arrays allowing for more uniform coverage over larger areas and better control of the spacing between the nanorods and the substrate. This method was based upon electrostatic interactions between the negatively charged PSS coated nanorods and positively charged polyallylamine hydrochloride (PAH) functionalized substrates (Figure 6.3).[256,257,258] Owing to the presence of the magnetic nickel segments, the nanorods could be magnetophoretically pulled from the suspension using a strong rare earth magnet placed below the substrate and fixed by electrostatic interactions between the oppositely charged polyelectrolytes (Figure 6.3a).[259] This ensured that the deposition could be performed very quickly (<5 minutes) and that nearly all of the nanorods in suspension were deposited on the substrate. For the nanorods to remain rigidly fixed while etching the sacrificial metal layer, the polyelectrolytes used for immobilizing the nanorods must be carefully selected. As mentioned above, the nickel segments were etched using concentrated HCl solutions. So, to ensure that nanorods stay fixed the polyelectrolytes must remain charged at very low pH conditions and weak polyelectrolytes must be avoided. PSS/PAH served well for this reason as they did not dissociate or swell in a noticeable manner in the concentrated HCl solution during the 5 minute long etching step. SEM images show that the rods were rigidly bound and displayed excellent retention of the gap structure and deposition concentration after etching of the nickel segments (Figure 6.3b).

The major advantage of method 2 is that it allowed for very uniform deposition of nanorods over large areas and with very high efficiency. The simple combination of

magnetophoretic deposition and electrostatic interactions is particularly useful as it can be extended to a wide range of functionalized substrates. Layer-by-layer (LbL) techniques have proven to be extremely versatile at deposition of alternately charged polyelectolytes on a wide range of substrates with varying surface chemistry, geometry, and topography. Furthermore, the nature of LbL techniques allows for precise control over the thickness of the polyelectrolyte layers. This control can allow the spacing between the nanorods and the substrate to be finely tuned, and ultimately provide a means to modulate potential interactions with the substrate. Finally, as long as the electrostastic interactions between the polyelectrolytes are maintained the assemblies are stable in a wide range of organic solvents and moderately high temperatures (<200 °C).

6.3.2 Single Particle Scattering Measurements

Characterization of the far-field optical properties of substrate bound nanoparticles especially at the single particle level is particularly challenging. Conventional UV-Vis micro-spectrometry does not typically allow for collection of spectra from individual array elements, as the collection areas are too large and result in spectra that are averaged over several array elements. In order to overcome the limitations of these conventional techniques, we utilized hyperspectral imaging in the dark-field mode, which allowed for recording of scattering spectra at wavelengths from 400-1000 nm at each pixel in a dark-field optical image. Optical pattern matching with SEM images was used to ensure that the scattering spectra were actually collected from single nanorod arrays and not bundles (Figure 6.4). Representative unpolarized spectra from each element in array 1 highlighted in Figure 6.5a along with the corresponding ensemble UV-Vis spectrum are shown in

Figure 6.5b. As expected, the averaged spectrum for the entire linear array shows broad scattering from 550 to 900 nm with convoluted peaks due to the differential degree of coupling in each dimer.

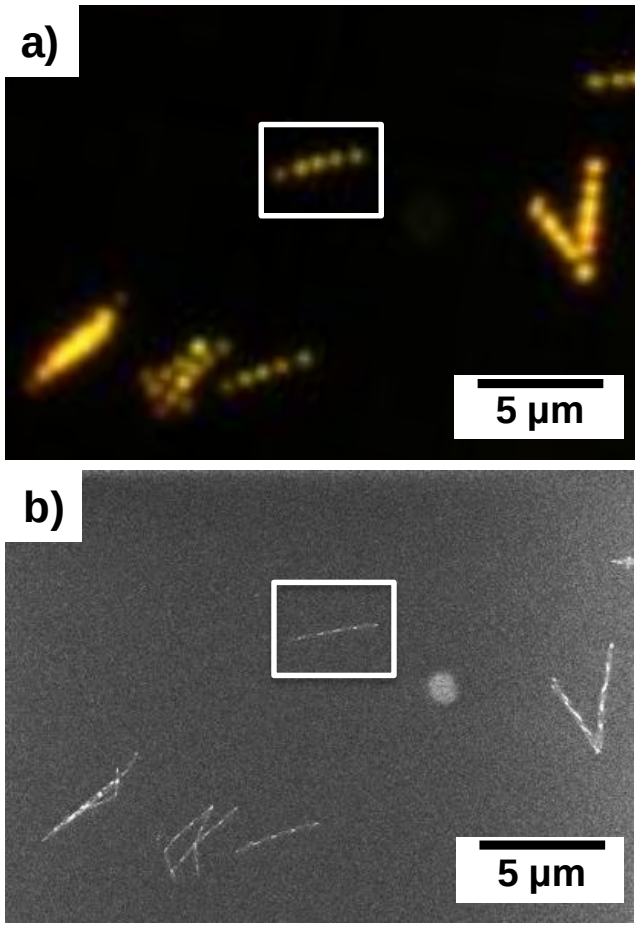

Figure 6.4: Optical pattern matching with SEM images was used to ensure that hyperspectral analysis was performed on single segmented nanorods. The nanorods in the a) hyperspectral dark-field image are clearly visible in the b) SEM image.

The spectra for each individual particle or dimer in array 1 exhibit more distinct scattering peaks. The spectrum for the 70 nm rod shows transverse and longitudinal resonance modes at 550 and 675 nm respectively, in close agreement with simulated spectra discussed in the next section. The spectra for the dimers with decreasing gap size

exhibit a transverse mode consistent with the uncoupled nanorods at 550-570 nm. As expected, the longitudinal mode for these dimers indicates significant coupling effects by a strong increase in scattering at longer wavelengths.[260] However, the spectra for the dimers and the 140 nm rod exhibit broad scattering with multiple convoluted peaks from 600 to 900 nm. We hypothesize that this broad scattering is caused by multi-pole resonance modes that may arise specifically due to roughness at the ends of the nanorods and appear more pronounced in strongly coupled or high aspect ratio nanorods. In order, to test this and more thoroughly resolve the coupling effects in dimers several follow-up experiments were performed.

First, a dimer array with larger gap spacing (array 2) was fabricated to determine if tunable coupling effects matching with simulated spectra could be clearly seen in systems with moderate coupling. Second, scattering spectra were collected again for array 1 with a polarized light source in an attempt to resolve anisotropic scattering modes in the strongly coupled dimers. Finally, the far-field optical properties of nanorods with specific non-flat end shapes routinely observed in SEM analysis were simulated in order to determine if specific modes observed in the experimental spectra could be attributed to these structural features.

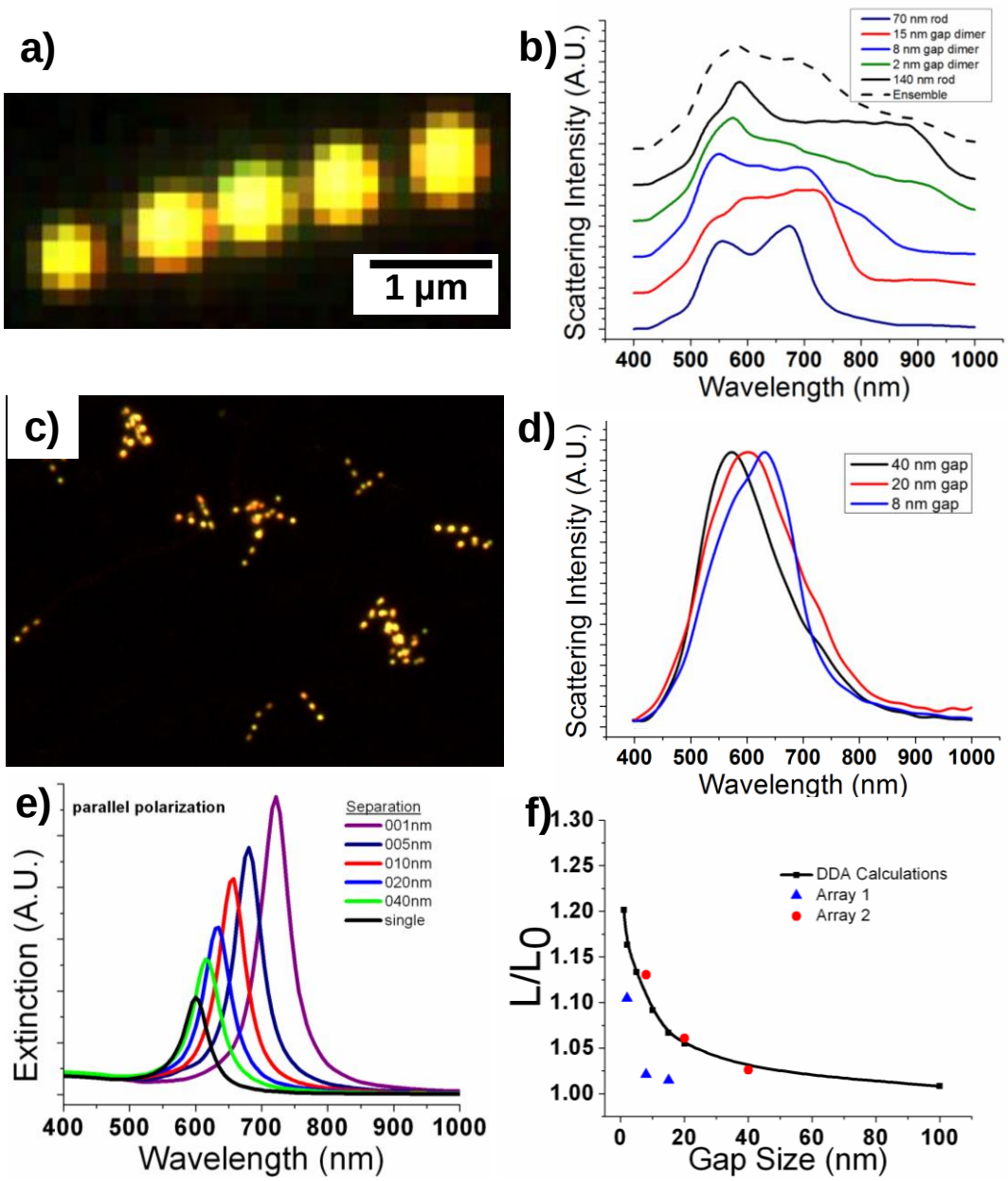

Figure 6.5: Hyperspectral dark-field images and unpolarized scattering spectra from arrays 1 and 2. a) High-resolution hyperspectral image of array 1. Each pixel in the image represents a scattering spectrum from 400 to 1000 nm. b) Scattering spectra corresponding to each dimer or rod shown in (a) along with integrated spectrum of a segmented nanorod (dashed line). c) Dark-field optical image of array 2 showing several arrays each consisting of 3 dimers. The color of each dimer can clearly be seen to shift from green to red as the gap size between the nanorods is reduced. d) Scattering spectra for dimers in array 2 with decreasing gap size indicating a noticeable red-shift in the longitudinal mode. e) DDA simulations of nanorod dimers showing the expected shift in the longitudinal mode. f) Comparison of the magnitude of the shift in the longitudinal mode with decreasing gap size, showing good correlation between the experimental and simulated results.

The hyperspectral image of array 2 shows dimer arrays with 3 distinct spots each of a remarkably different color (Figure 6.5c) varying from green to red as the gap spacing decreases. This visible color shift is in stark contrast to the hyperspectral image of array 1 (Figure 6.5a) in which each array element appears a bright yellow color due to the broad scattering at long wavelengths. The corresponding spectra from array 2 (Figure 6.5d) clearly shows the longitudinal modes for each dimer pair shifting from 600 to 650 nm as the gap spacing decreased from 40 to 8 nm. Additionally, the spectra from array 2 do not show strong scattering beyond 700 nm in contrast to array 1 indicating overall weaker coupling, as expected, from the larger gaps sizes in the array structure. For comparison with the experimental results from array 2, spectra for the dimer pairs were simulated by the discrete-dipole approximation (DDA) method (Figure 6.5e). The simulated spectra exhibit a well-known red shift in the longitudinal mode as the spacing between nanorods is reduced. Figure 6.5f shows the relative change in peak position with gap size for the DDA calculations as well as arrays 1 and 2. For array 2, the relative shift for the longitudinal mode was calculated using 570 nm as the position for the uncoupled longitudinal mode. The absolute peak positions, however, were slightly red shifted from the experimental results, which may result from small discrepancies between the simulated and experimental systems. Indeed, the simulations were performed for perfectly cylindrical dimers in uniform medium with average refractive index of 1.53. Whereas, the experiments were performed with dimers having rough ends and at the interface between the polystyrene film with refractive index of 1.55 and the immersion oil with refractive index of 1.515.

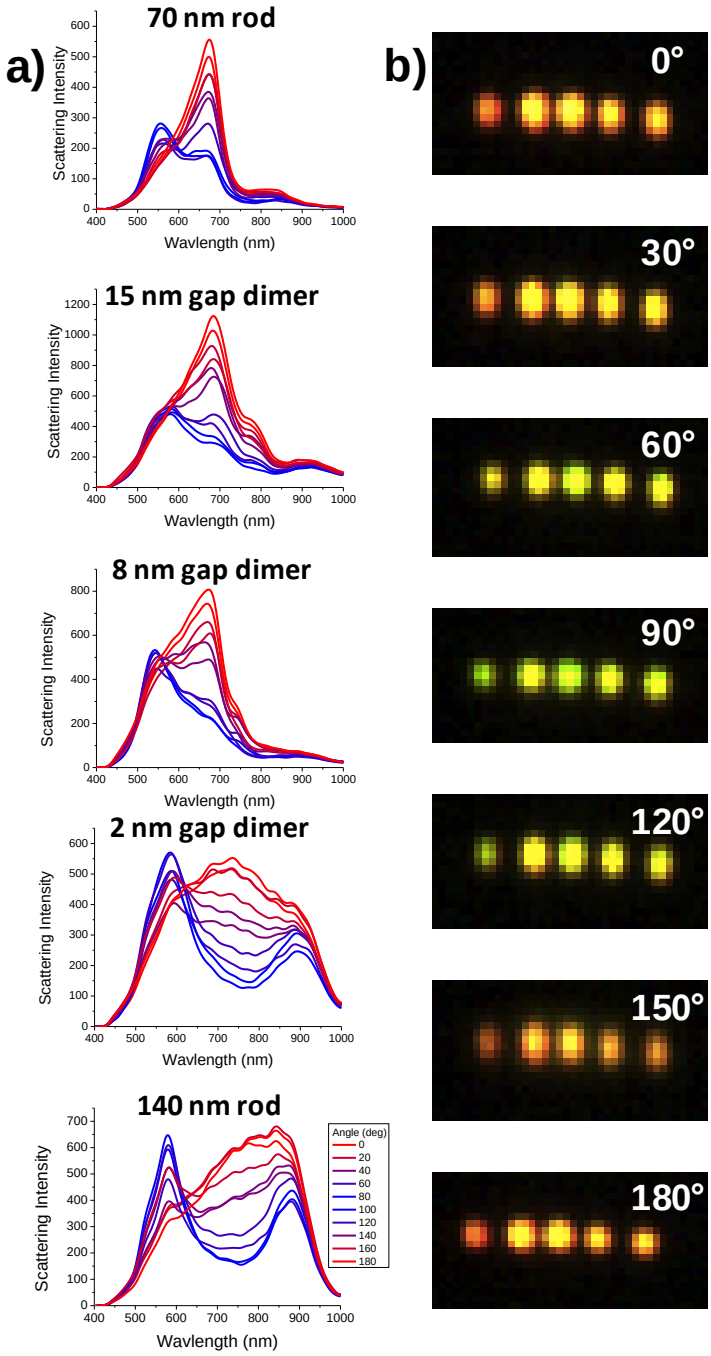

Figure 6.6: a) Polarized scattering for each dimer or rod in array 1. 0 and 180 degrees polarization correspond to the long axis of the dimer array (red lines), and 90 degrees polarization is perpendicular to the long axis of the dimer array (blue lines). Polarized spectra show selective excitation of the transverse and longitudinal modes with varying polarization angle. b) Dark-field optical images collected with polarized incoming light. The images show change in the predominant scattering mode from a red/orange color corresponding to the longitudinal mode excited at 0 and 180 degrees, to a green color corresponding to the transverse mode excited at 90 degrees.

The results from array 2 indicate that the expected shifts in the longitudinal mode due to coupling can be observed in moderately coupled dimers without giving rise to broad scattering at longer wavelengths. However, in order to more clearly resolve the spectra from the strongly coupled dimers in array 1, we performed high-resolution hyperspectral imaging with a polarized light source. The spectra collected for the individual nanorods and dimers clearly reveal the anisotropic nature of the optical scattering modes, which was not observed in the unpolarized measurements. The scattering spectra at different polarization angles for all elements in array 1 are shown in Figure 6.6a with 0 and 180 degrees corresponding to the long axis of the nanorod array. The relative intensities of the plasmon peaks vary dramatically with polarization orientation. At 0 and 180 degrees relative to the long axis of the linear array, the electric field component of the incident light is primarily in the long axis of the rod, and as a result the longitudinal modes are preferentially excited. Conversely, at 90 degree orientation the transverse mode is primarily excited.[261,262]

The spectra collected for the single 70 nm rod shows selective excitation of both the transverse and longitudinal plasmon modes at 550 nm and 675 nm, respectively. For all other array elements, the position of the transverse mode stays within 550 to 580 nm close to that of the uncoupled 70 nm rod. In the 15 and 8 nm gap dimers, the longitudinal mode appears at 700 nm and is red-shifted compared to the uncoupled nanorod. The polarized measurements were critical to identify the longitudinal mode for the 2 nm gap dimer and the 140 nm rod. In both cases, an additional peak appears at 900 nm, which

caused the peaks in the unpolarized spectra to appear broad and convoluted. However, in the polarized spectra the longitudinal mode becomes visible due to its modulation with polarization angle and appears at 750 and 775 nm, respectively. The ability to perform these polarized measurements at the single particle/dimer level provided a means to separate and identify the expected resonance modes.[260]

The polarization dependence of the plasmon excitation is also directly visible from the dark-field optical images that were collected at different polarization angles (Figure 6.6b). The first spot in the linear array (from the left side) is the terminal gold rod of 70 nm length. The light scattered by this particle shifts from red at 0 degrees, to green at 90 degrees, and back to red at 180 degrees. This agrees well with selective excitation of the red longitudinal mode and green transverse mode at the corresponding angles. Similar trends are observed for other segments, however, with some orange/yellow color at 0 and 180 due to scattering at longer wavelength, which may be compromised by the limited detector sensitivity for wavelengths above 900 nm.

The polar charts in Figure 6.7 show the angular variation for the relative intensities of the transverse and longitudinal modes for each segment of array 1. The angular variation of the scattering intensity data, *I(θ)*, were fitted by phase-shifted sine squared functions, as predicted for gold nanorods, in the form [263]:

$$I(\theta) = \alpha_{\perp} \sin^2(\theta - \theta_{\perp}) + \alpha_{\parallel} \cos^2(\theta - \theta_{\parallel})$$

where $\alpha_{\parallel}$ and $\alpha_{\perp}$ are polarization anisotropy ratio for the longitudinal and transverse bands, respectively and θ is the polarization angle.

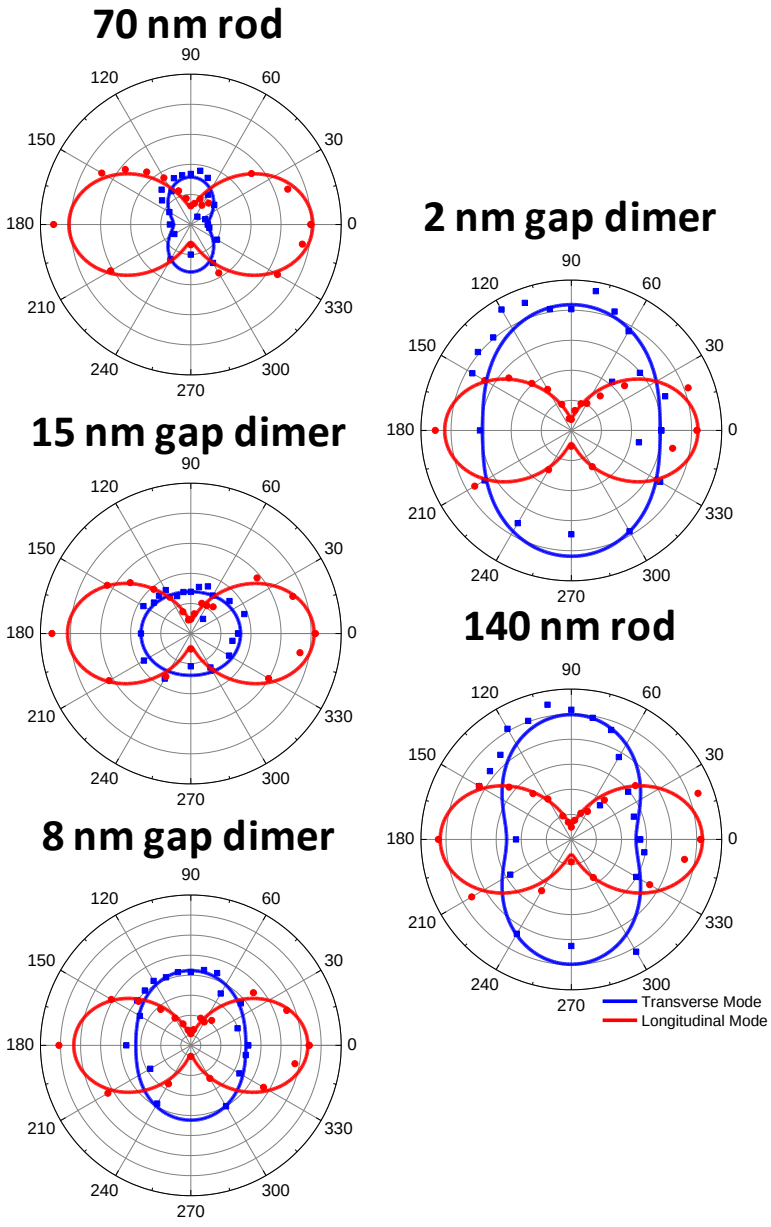

Figure 6.7: Polar charts showing the relative intensities of the transverse (blue lines) and longitudinal (red lines) modes for each dimer or rod in array 1.

For the 70 nm gold rod, the maximum for longitudinal mode is achieved at $\theta = 0.7 \pm 1.5^{o}$, and $\theta = 92.4 \pm 1.5^{o}$ for transverse mode, very close to the expected values. The half-widths of polarization dependencies are close to 50^{o} for both modes. Anisotropy ratios were 5 for longitudinal LSPR modes and decreased to 2 for transverse mode. According to recent theoretical estimations, for purely dipolar behavior the polarization anisotropy ratio can reach 10-100 for extinction of the longitudinal mode. The reduction of the polarization anisotropy to 5 observed here for scattering intensity can be related to several factors. Firstly, the gold nanorods fabricated had a relatively low aspect ratio of approximately 1.4, which is considerably smaller than typically aspect ratio reported earlier (>2) and inherently leads to weaker polarization anisotropy. Secondly, the polarization anisotropy can be weakened by inhomogeneous broadening of the longitudinal mode. Considering that we conducted spectral measurements for individual nanorod dimers in contrast to conventional bulk measurements, the last factor cannot be related to this nanostructure inhomogeneity but rather with roughness at the gold nanorod ends as will be addressed in simulations discussed below.[264,265,266]

It is worth to note that unexpectedly, apart from the expected transverse and longitudinal dipolar modes, a few other unique features have been detected in the polarized spectra of individual nanorods. Indeed, in the spectra for the 70 nm rod, a small peak appears at 833 nm. This peak seems to shift to 900 nm for the remaining elements, and dramatically intensifies for the 2 nm gap dimer and the 140 nm rod. The longitudinal mode for both the 15 and 8 nm gap dimers contain a red-shifted shoulder peak, and the transverse mode for the 15 and 2 nm gap dimers and the 140 nm rod contain a blue-shifted shoulder peak.

The presence of the consistent SPR peaks usually indicates the presence of nanostructural elements with different transversal or longitudinal dimensions. However, in our case this explanation is not supported by direct high-resolution observation of large nanorod arrays which shows very uniform (within 5%) geometrical dimensions of all segments fabricated here.

Therefore, in order to understand the potential contribution of the roughness at the ends of the nanorods towards these scattering modes, finite-difference time-domain (FDTD) simulations were performed for *real nanorod shapes with varying end geometry (actual defects).* From SEM images, we found that the ends of the nanorods commonly deviated from a flat geometry and often have a concave or convex curvature at their tips as well as asymmetric end shape with sharp "tails". For example, in Figure 5.2e the rod ends on either side of the gap show this morphology clearly. Another feature that was routinely observed was "comet-tail" like morphology that extent from the ends of some rods (shown in the top right nanorod in Figure 5.2d).

The effects of deviations of these end shapes from ideal flat facets were simulated for 70 nm long uncoupled nanorods asymmetric shapes to be simulated by different combinations of convex and concave shapes of different facets. The resulting simulated spectra for different scenarios are shown in Figure 5.8. The peak positions for the transverse and longitudinal modes in the simulated spectra to differ significantly from that for the ideal shape. These shifted positions were found to match well with the experimentally measured results (555 and 673 nm, respectively).

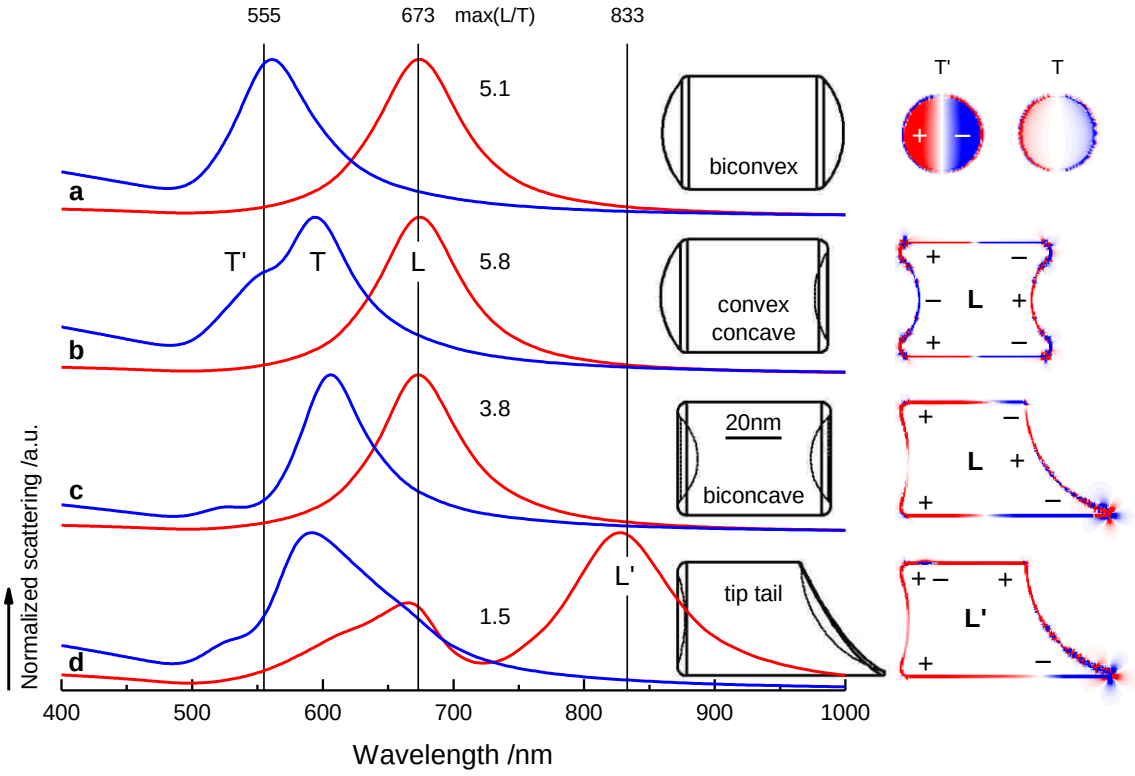

Figure 6.8: FDTD simulations of the effects of the tip shape on the scattering modes in uncoupled gold nanorods. a-c) Simulated spectra for nanorods with a combination of convex or concave tip shapes. Nanorods with concave tip shapes show a second transverse mode at higher energy, which was also observed in the experimental results. d) Simulated spectrum for a nanorod with a "comet-tail" like tip which resulted in a new peak appearing at 830 nm. FDTD simulations of the effects of the end tip shape on the scattering modes: 3D model of asymmetric tail along with plots of two strongest asymmetric charge distribution modes which contribute to the appearance of new long-wavelength resonance.

Different combinations of non-flat facets might result in very different scenarios for SPR peaks shifts. The first three rods shown (Figure 6.8a-c) contain different combinations of the convex and concave end shapes. Interestingly, in the cases where a concave end is present we observed splitting of the transverse mode (Figure 5.8b and c). The charge plots shown in the upper left inset indicate that this new transverse mode (T') is the second order resonant mode and as result appears at a higher energy. In the case of a

biconcave tip shape the charges are symmetric distributed correspondingly to the symmetry of the nanorod. The position of this higher order transverse mode agrees well with the experimental spectra where a blue-shifted shoulder peak was observed for the 15 and 2 nm gap dimers and 140 nm rod.

Finally, Figure 6.8d shows the simulated spectra for a peculiar nanorod with the "comet-tail" morphology on one side which is also frequently observed in the nanorods. Such a highly asymmetric nanorod shape resulted in a large resonance peak appearing at longer wavelength around 830 nm that is close to the additional surprising peak observed for the 70 nm nanorods.

Our simulations showed that an asymmetric tip tail generated by sphere (or etched by sphere) with the radius of 100 nm results in an additional longitudinal mode (L') (Figure 5.8d). Experimentally, a ratio of maximum of longitudinal scaled by the maximum of the transverse mode was measured of 1.78 (max(L/T)). In all cases the longitudinal mode wavelength could be achieved by adjusting the length of the nanorod. Change in the tip shape results in altering of the LSPR mode shown by the surface charges distributions. The second transverse mode (T') could be identified as an additional inverted charge at the outer shell compare to the transverse mode (T). The tip tail alters the symmetrical charge distribution for ideal symmetrical nanorods significantly with results of two longitudinal modes (Figure 6.8d). The 672nm mode (L) is similar to a biconcave mode. The second longitudinal mode shows a higher amount of charge separation with a charge concentration in the tip tail. This higher amount of charge separation is responsible for

the higher intensity at the L'-mode which is different from the experimental observations. This discrepancy can be related to mismatch of the orientation between longitudinal polarization and the long axes of the nanorod during measurements which can easily be within 10^{o}.

6.4 Conclusions

The inherent advantage of the template based strategy employed here is the ability to generate tailored linear arrays of rods with fine control over rod diameter, length, and spacing between rods. In this report, we have extended the versatility of this approach by demonstrating a simple method to transfer these linear nanorod assemblies in high quantity onto surfaces while preserving the fidelity of the local array structure. Moreover, we were able to measure the highly anisotropic LSPR optical properties at the single particle level using high-resolution hyperspectral imaging and suggest the origin of the multiple plasmon resonances including some peculiar optical features caused by characteristic fabrication defects. This capability to fabricate programmable assemblies and measure optical properties at the single particle level will be crucial for the practical development of plasmonic antennas, SERS sensors, and multiplexed biological/chemical LSPR sensors. Future efforts must be undertaken to understand the effects of roughness at the rod ends on the optical properties of template fabricated nanorods, especially in the regime of strong LSPR coupling. With further improvement in the assembly of these segmented nanorods with long-range order, this strategy has strong potential towards practical applications.

CHAPTER 7

A ROBUST AND FACILE APPROACH TO ASSEMBLING TUNABLE, MOBILE, AND HIGHLY-OPEN UNFRUSTATED TRIANGULAR LATTICES FROM FERROMAGNETIC NANORODS

7.1 Introduction

The fabrication of uniform colloidal arrays with easily tunable lattice spacing and symmetry is uniquely challenging due to self-assembly processes typically being driven and stabilized by mid- to short-range interactions such as electric double-layer repulsion, Van der Waals attraction, and steric repulsion.[267] Thus, a vast majority of traditionally assembled colloidal systems have a simple close-packed structure with lattice spacing and symmetry defined by particle size, shape, and charge properties.[268,269,270] Materials strategies to achieve open, tunable, and complex lattices with potentially unique properties include colloidal epitaxy,[271,272] binary colloidal mixtures,[273] template assisted confinement,[274,275] Janus or patchy functionalization,[276,277,278] and the use of biomolecular/polymeric linkers or surfactants.[279,280,281,282,283] While interesting and useful, these approaches tend to be multi-step, low-yield, and often require time-consuming design of materials systems including synthesizing complex linkers (e.g., complementary DNA strands),[279,280,281,282] processing multicomponent mixtures (e.g., nanoparticles and surfactants),273 or achieving cumbersome selective functionalization of particles (e.g., site-specific grafting or modification).[276,278] For bottom-up assembly processes to truly rival conventional top-down fabrication in technological importance, novel strategies that leverage long-range forces and allow for easy fabrication of highly ordered structures with tunable, open, and mobile lattices are crucial.

The application of external electric and magnetic fields can organize colloidal micro- and nanoparticles into ordered open lattices based on long-range interactions between induced or permanent electric or magnetic dipoles.[284,285,286,287,288,289,290,291] Numerous studies have demonstrated that the modulation of DC and AC fields can lead to precise control over the lattice structure in one- and two-dimensional arrays.[292,293,294] However, a major limitation for such methods is that the particles preferentially form chains in the field direction with poor ordering between adjacent chains.[295,296] The lack of ordering arises from the varying dipole magnitudes among the inherently polydisperse chains in unconfined systems. This is typically overcome by utilizing physical confinement to prevent chaining altogether or only allowing the formation of monodisperse chain lengths. While the addition of physical confinement enables efficient formation of highly ordered arrays, this requirement presents its own challenges. For example, assemblies formed at the air-liquid or liquid-liquid interfaces dissipate the moment the external field is removed.[292,293] These restrictions limit the attractiveness of field-assisted assembly methods, especially in scenarios where it is desired to assemble particles *in situ*.

In contrast to current methods, the approach suggested here enables the magnetic field-assisted assembly of chemically functionalized nickel nanorods into long-range ordered and tunable 2D lattices directly at a substrate surface using a low-cost magnetic system and eliminating the need for any physical confinement beyond the substrate surface. Careful control of the nanorod concentration and deposition method allows for the formation of a metastable ferromagnetic monolayer of vertically oriented nanorods. In

the assembled state, the nanorods form an extremely open unfrustrated triangular lattice with the spacing between nanorods exceeding their radius by nearly two orders of magnitude. We demonstrate control over the lattice spacing and symmetry by varying the magnitude and orientation of the applied magnetic field. The direct assembly of the nanorods at the solid-liquid interface further facilitates anchoring of the nanorods to the substrate through triggered intermolecular interactions enabling preservation of the assembled array even after removing the magnetic field. Immobilizing the nanorods in this way opens tremendous possibilities including hierarchical and sequential assembly of multiple lattices in close proximity to each other, and rapid actuation of the nanorod arrays by changing the magnetic field orientation in a manner similar to artificial cilia.

7.2 Experimental Methods

7.2.1 Fabrication of Nickel Nanorods

Nickel nanorods were synthesized in a porous anodic alumina template (Anodisc 47, Whatman) based on previously reported methods.[297,298,299] Briefly, a 50 nm thick gold layer was sputtered onto the branched side of PAA template to serve as the working electrode and attached at the edge to a thin wire using conductive silver paste. A thick nickel layer was then deposited from a commercial nickel sulfamate RTU solution (Technic Inc) by applying a -1.8 V potential using a Keithley 2400 sourcemeter for 20 minutes against a platinum counter electrode. The above nickel layer served to seal the pores while a thick paint layer applied thereafter ensured that the deposition occurred only through the pores. A sacrificial silver layer was deposited from a 1025 RTU @ 4.5 troy/gallon (Technic Inc) at -1.2 V for 5 min. Subsequently various length of Ni rods

were obtained (400, 800, 1600, and 4800 nm) by carrying out the deposition for varying times (5, 10, 20, 60 minutes).

The alumina template was dissolved in a solution of 1M NaOH with an additional 20 mg/ml polyvinylpyrrolidone (3,500,000 g/mol). After rinsing the remaining film in deionized water, the film was submerged in a 4:1:1 solution (ethanol:NH_3OH:H_2O_2), which released the rods into solution by etching the sacrificial layer of silver. After 10 minutes, the film was sonicated in solution, allowing the final release of the rods. Following this step, the nanorods were centrifuged and washed thrice, before final dispersion into 1ml of 20 mg/ml polyvinylpyrrolidone in aqueous solution. The nominal thickness of the PVPON shell was taken as 3.5 nm. It was found that polystyrene sulfonate (PSS) could also be used as a stabilizing polymer instead of PVPON. Though not presented in this work, these rods were noted to behave similarly to the rods coated in PVPON.

7.2.2 Magnetic Assembly

A piece of atomically polished piranha cleaned silicon wafer (approximately 1x1 cm in dimension) was used as a substrate for the magnetic assembly. This substrate was placed onto a rare earth magnet with magnetic field of 900, 1800 or 2700 gauss so that magnetic field was orthogonal to the substrate surface. After wetting the substrate with 50 µl of de-ionized water, 50 µl of a 250,000 nanorods/mL aqueous solution of nickel nanorods was added to the surface.

7.2.3 Tethering nanorods to substrate

It was originally determined that the nanorods could be pinned to the surface of the silicon substrate through addition of excess amounts (typically, 50 µl) of 25 mM NaCl in aqueous solution to the nanorod assembly. In the final approach, PMAA was used to tether the nanorods via hydrogen bonding between PMAA and PVPON. In brief, three PMAA/PVPON bilayers were deposited onto a silicon substrate via spin coating in a layer-by-layer fashion, with PVPON as the terminal monolayer. Following the assembly of the rods onto this substrate, 50 ul of 1 mg/ml PMAA solution was added onto the rods. The PMAA bound to the PVPON coated rods and PVPON coated substrate, forming a bridge between the two. Subsequently, gentle rinsing was employed to remove the excess PMAA from the substrate. In the case of PSS coated nanorods, a similar approach was used to tether the nanorods. In this approach, poly(allylamine hydrochloride) (PAH) was used in the place of PMAA to tether the nanorods. For this system, a silicon substrate with three bilayers of PSS/PAH (PSS terminated) was used for the assemblies. Though not presented here, this system was functionally identical to the PVPON/PMAA system detailed above.

7.2.4 Characterization

Shortly following the assembly of the Ni nanorods onto the silicon substrate, the assembly was imaged using a Leica DM4000 M optical microscope. All images were acquired using the dark field setting of the microscope at 10x, 20x, or 50x magnifications. During initial imaging, the substrate was kept under the magnetic field. After the rods were fixed to the substrate, the substrate was removed from the magnetic

field. In order to conduct SEM (Zeiss Ultra 60 FESEM) imaging on the assemblies, the rods were tethered to the substrate and the solvent was allowed to evaporate.

The MFM images were obtained on a Bruker Innova AFM operated under tappingmode.[300] MESP cantilever series purchased from Bruker with a tip radius ~25nm and spring constant ~3 N/m were used for the imaging. Typically, MFM imaging is done using a 'two-pass' technique. In the first pass, the cantilever is oscillated at the resonant frequency and the topographic profile of the surface is recorded. In the second pass, the tip is raised above the surface (200 nm) and moved over the sample along the same topographic path to give the MFM image of the surface.

7.3 Results and Discussion

The functionalized nickel nanorods used for field-assisted assembly were made by a well-known template-assisted technique based on electrodeposition in porous anodic alumina templates.[301,302,303] The advantage of this technique is that it allows for high throughput and uniform fabrication of nanorods with adjustable dimensions.[304] The lengths of the rods were varied by adjusting the duration of electrodeposition, resulting in rods with lengths between 400 nm and 1600 nm (Figure 7.1a shows a 800 nm long nanorod). Individual nanorods were obtained by dissolving away the alumina membrane and coated with a layer of polyvinylpyrrolidone (PVPON) to prevent aggregation in solution (Figure 7.1b). Nickel nanorods in this dimension range and made with similar techniques have been shown to be ferromagnetic with a saturated magnetization close to the bulk value of nickel (485 emu/cm^3).[305] Since all of the rods used in the study have an aspect ratio

greater than one (ranging from 2 to 8), they have an easy axis of magnetization along the long axis of the rod. Indeed, magnetic force microscopy (MFM) of a magnetized nanorod shows a contrast in the phase shift along the length of the rod thus confirming that the magnetic dipole moment is aligned with the rod's long-axis (Figure 7.1c).

Upon placement of the nanorod suspension in a vertical magnetic field the nanorods are quickly magnetized and orient perpendicular to the substrate surface (Figure 6.1d). The placement of the magnet creates a steep gradient in magnetic flux density normal to the substrate that results in a magnetophoretic force pulling the nanorods from the suspension to the surface.[306,307] Once on the surface, the nanorods maintain high lateral mobility and undergo a "phase separation" that results in the formation of stable labyrinth or island-like morphology. On larger diameter magnets (diameter > 1 cm), the nanorods were found to first form a labyrinth morphology that coarsened over time to eventually form discrete islands (Figure 7.2). However, using smaller magnets (diameter < 1 cm) the assembly could be controlled so that only a single island was formed in response to the radial gradients in magnetic flux density. Using this method, the nanorods are preferentially concentrated at the center of the magnet, and the position of the island can be precisely controlled by placement of the magnet center.

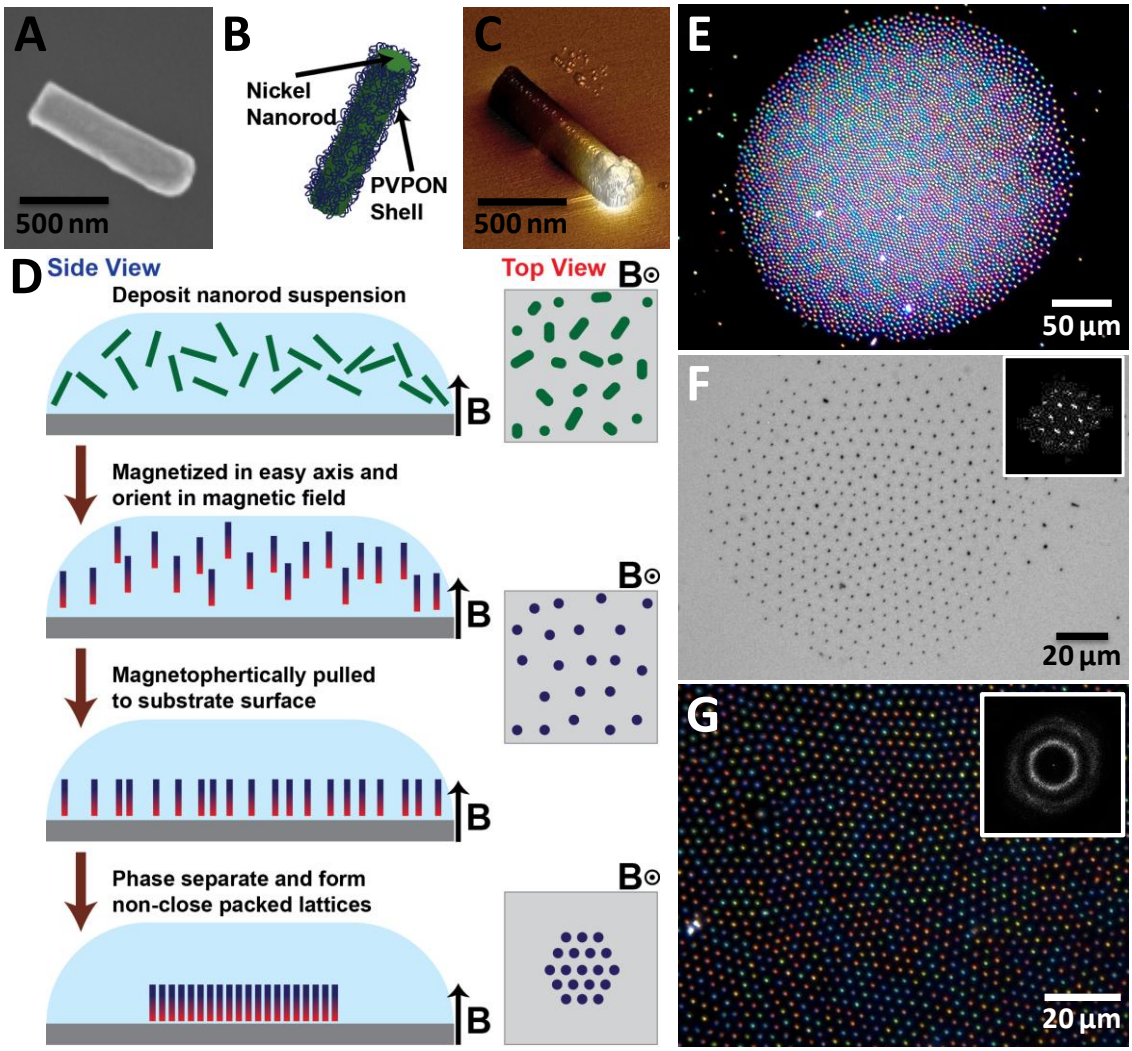

Figure 7.1: Assembly of nickel nanorods in a non-uniform orthogonal magnetic field. a) SEM image of a 200 by 800 nm nanorod; b) Illustration of a polyvinylpyrrolidone coated nickel nanorod; c) Magnetic force microscopy image showing the persistent magnetic dipole on a nanorod after removal from an external magnetic field; d) Schematic showing a cross-sectional and top-down perspective of the proposed nanorod assembly process; e-f) Optical microscopy images showing e) a well formed island imaged under dark field, f) a smaller assembly imaged under bright field with corresponding fft, g) an assembly imaged at high magnification under dark field with corresponding fft.

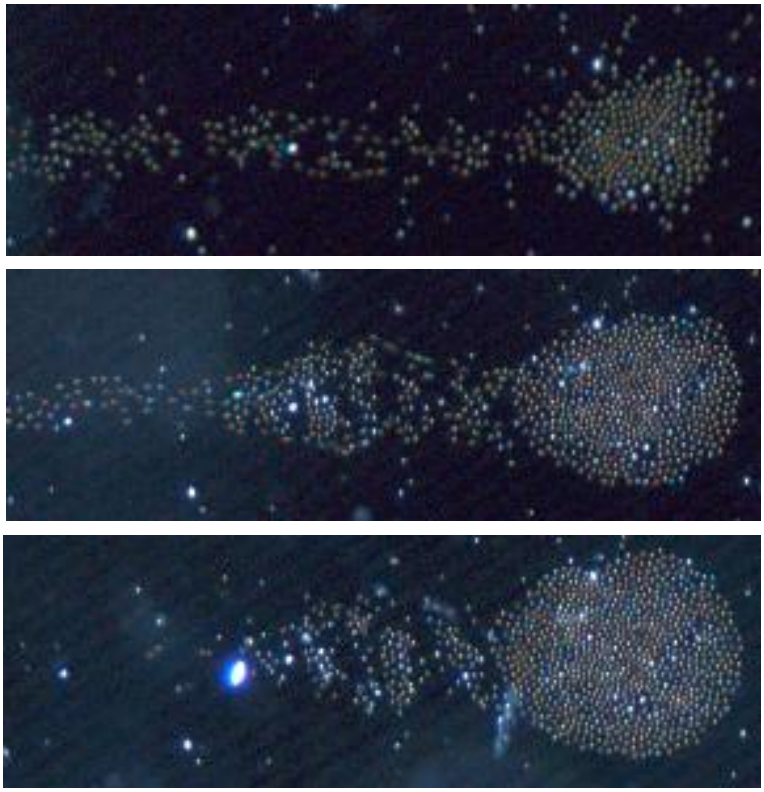

Figure 7.2: Sequence of dark field optical images showing the coarsening of labyrinth structure into discrete islands.

In this process, individual nanorods continually "arrive" from the bulk phase and incorporate themselves at the island boundaries until depleted as can be observed in real-time (Figure 7.1e, Video 7.1). Interestingly, within the aggregated phase the nanorods are packed into an extremely open and ordered hexagonal lattice with long-range positional order indicated by six-fold symmetry in the FFT with up to third order of Fourier components visible (Figures 7.1f and g). We observed that a dilute suspension of nanorods can be used to avoid the formation of chain aggregates within the island. At higher concentrations ($>10^6$ nanorods/mL), the chain aggregates in the island dramatically impact the quality of the lattice ordering as these aggregates have a larger dipole moment observed by a larger clearing zone. Therefore, reducing the concentration

to below 2.5 x 10^5 nanorods/mL resulted in the formation of monolayer islands with excellent lateral long-range ordering. Moreover, the individual island size can be tightly controlled over a wide range by varying the total amount of nanorods, from small islands, containing fewer than 20-50 nanorods all the way up to large-scale islands with 500 μm diameter, containing more than 25,000 nanorods (Figure 7.3). The placement of the island could precisely be manipulated after formation as the entire island could be efficiently and continuously moved by slowly moving the magnet in relation to the substrate (Video 7.2). Real-time lateral movement of the nanorods with reconfiguration of local organization, deformational flow around defects, and continuous reformation of the island front are clearly visible in the video.

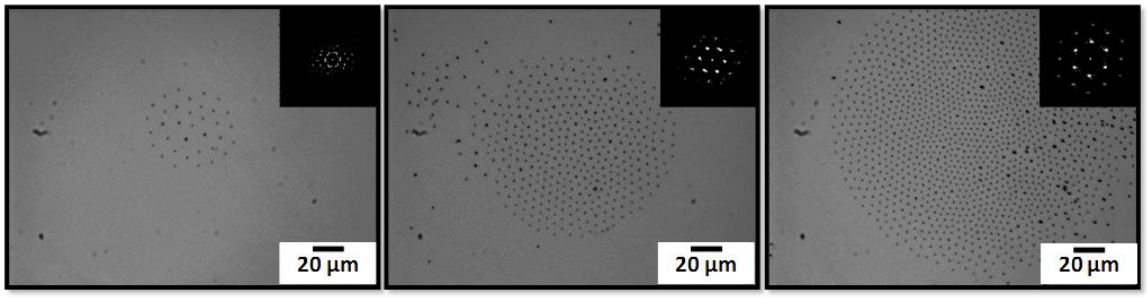

Figure 7.3: Sequence of optical images depicting islands of varying size and number of rods.

The field-assisted formation of lattices with spacing incommensurately larger than size of the individual elements is facilitated by the long-range repulsive forces arising from the uniformly aligned magnetic dipole moments of the nanorods (ferromagnetic ordering).[292] As known, frustrated triangular lattices can be formed by magnetic dipoles which are free to change their dipole orientation.[308] Such flipping events minimize the overall magnetic energy of unconfined lattices and facilitate formation of triangular symmetry with lattice spacing (***d***) comparable to the magnetic dipole length (***l***): ***d ~ l***. In striking contrast, the

kinetically confined spatial conditions at the solid-liquid interface and the externally applied field cause the nanorods to lose the freedom to flip. Thus, the only physical pathway to magnetic energy minimization is lateral displacement to form unfrustrated and highly-open lattices with a unique $\boldsymbol{d} >> \boldsymbol{l}$ characteristic, which is rarely observed in synthetic colloidal systems. Dramatically increasing spacing minimizes repulsive interactions and continues until it is balanced by the much weaker chemical potential, stabilizing at distances about two orders of magnitude larger than the diameter of the nanorods.

The repulsive long-range forces provide a means for easy and wide range tunability of the lattice spacing and symmetry. Increasing the magnetic moment of the nanorods through an increase in either the volume or the magnetization of the nanorods will lead to an increase in the magnetostatic repulsive force and consequently larger lattice spacing. As known, the magnetic field H_x created by a dipole with moment m and length $\boldsymbol{l}$, at a distance x in the direction perpendicular to the dipole, is given by:

$$H_x = \frac{m}{\left(x^2 + \frac{l^2}{4}\right)^{3/2}}$$

where the magnetic moment is $m = MV$, and M and V are respectively the magnetization and volume of the nanorod.[305] This dipole approximation gives a valuable estimation of the magnitude of the magnetostatic forces between nanorods with different characteristics.

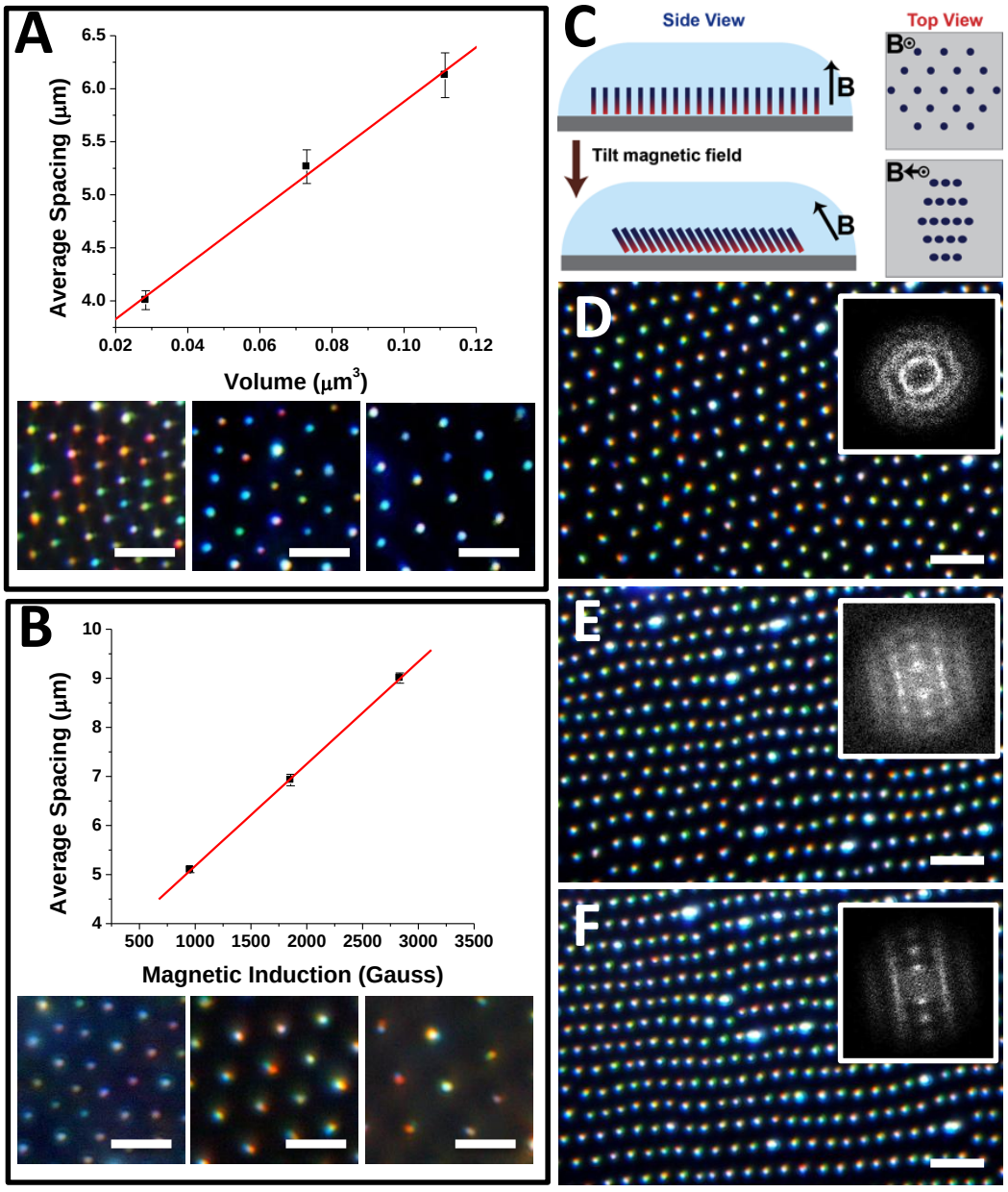

Figure 7.4: Tunability of lattice spacing and symmetry. a) Graph demonstrating the linear relationship between nickel nanorod volume and the equilibrium rod spacing in the assemblies. Inset images are shown (left to right) for 0.0126, 0.0251, and 0.0503 μm^3 . b) Graph demonstrating the linear relationship between applied magnetic field and the equilibrium rod spacing in the assemblies. Inset images are shown (left to right) for 900, 1800, and 2700 Gauss applied field. c) Schematic showing a cross-sectional and top-down perspective of the effect of an orthogonal and non-orthogonal field on the rod assemblies. d-f) Sequential dark field optical microscopy images of rods as magnetic field is tilted and corresponding FFTs: d) orthogonal field, e and f) tilted fields.

To test this relationship, nanorods with lengths of 400, 800, and 1600 nm (constant diameter of 200 nm) were fabricated and assembled on a cylindrical magnet with surface field strength of 900 Gauss. Figure 7.4a shows optical images of the resulting lattices and a plot of lattice spacing versus rod volume. As expected from eq. 1, it is found that the spacing increases linearly over the range of 4 μm to 6.5 μm with the increase in nanorod volume. Based on the saturated magnetization of nickel (485 emu/cm^3), we find that field strength for each nanorod length at the respective equilibrium lattice spacing was fairly constant and between 8-9 Oersted. This indicates that the repulsive force at the equilibrium lattice spacing is likely constant over this range of rod lengths.

Similarly, increasing the magnetization of the nanorods should increase the perpendicular field and also the repulsive force in accordance with eq. (1). To test this relationship, 800 nm long rods were assembled on magnets with surface field strengths of 900, 1800, and 2800 Gauss and the resulting lattice spacing was measured (Figure 7.4b). It was found that the lattice spacing increased linearly with the increase in magnetic field indicating that the field strengths of the magnets are above the saturation field of nickel, at which point the susceptibility becomes nearly constant. Thus, an increase in the external field leads to corresponding increase in the magnetic moment of the nanorods.

Finally, tilting the external magnetic field with respect to the substrate plane easily reorients the nanorods to maintain the easy axis of magnetization in the field direction. As a result, the repulsive force between adjacent rods becomes anisotropic and the nanorods form a rhombic lattice with the reduced lattice parameter in the direction of the

tilted magnetic field (Figure 7.4c). In Figures 7.4d-f, the optical images show the effect of sequential tilting of the external magnetic field on the lattice geometry in an assembled island, and as expected the lattice geometry shifts from triangular (Figure 6.4d) to rhombic (Figure 6.4e) as confirmed by FFT images. This is due to the weakening of the repulsive forces with the decrease in the distance between the opposite magnetic poles in adjacent nanorods. A further increase in the magnetic field angle with respect to the substrate normal results in a decrease in the lattice spacing with preservation of strong interchain correlations in contrast to the uncorrelated magnetically-assembled chains of spherical nanoparticles (Figure 6.4f).[309]

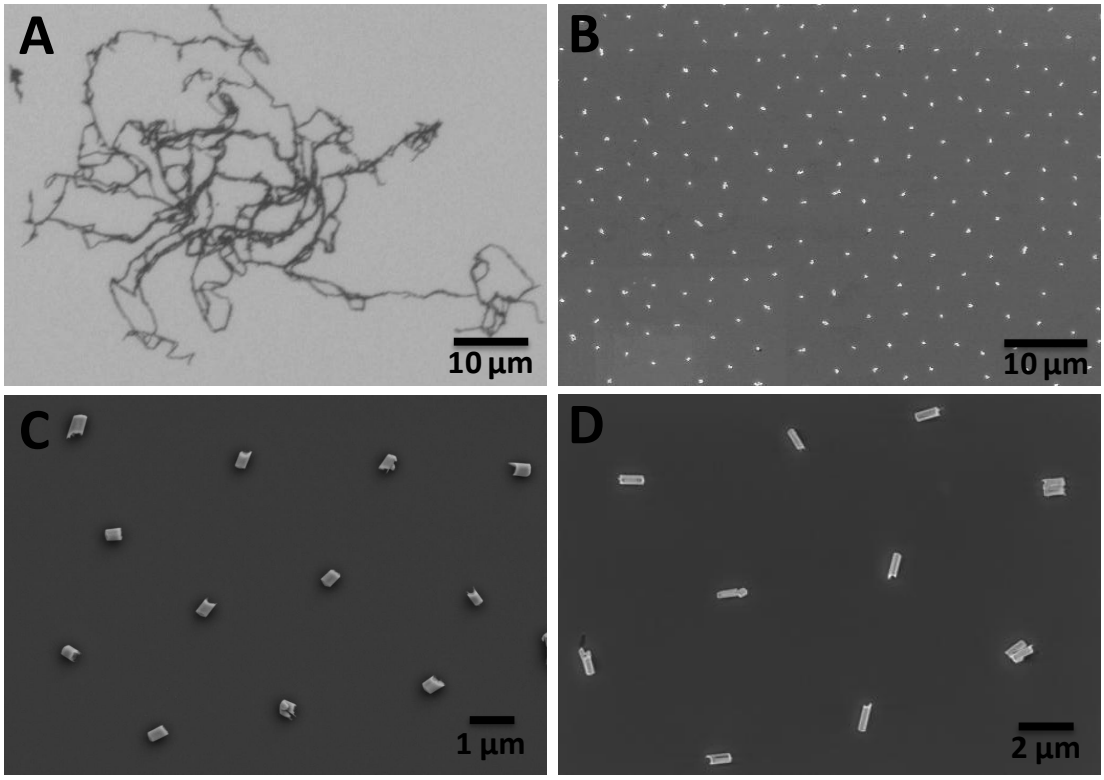

Figure 7.5: Tethering of nanorod arrays to the substrate. a) Bright field optical image demonstrating the effect of removing the external field without tethering nanorods. b-d) SEM images showing tethered nanorods after external fields have been removed, b) large area view of 400 nm length rods, c) close-up image of 400 nm length rods, d) close up image of 800 nm length rods.

As mentioned earlier, one of the major challenges facing field-assisted assembly methods is the difficulty in maintaining the assembled arrays in integrated materials/structures when the assisted field is turned off. In fact, as expected, without further processing to anchor or encapsulate the nanorods, removal of the magnetic field leads to irreversible chain formation (Figure 7.5a) due to the strong remnant magnetization of the ferromagnetic nanorods and preferred pole-to-pole interactions. Once this happens the array cannot be recovered even when the magnetic field is reapplied. Since the nanorod array is assembled and anchored directly at the substrate surface, the close proximity of the nanorods with the substrate enables strategies for robust encapsulation and preservation of the nanorod arrays. A second major advantage is that the assembled arrays can be further incorporated in flexible media using conventional processes such as monomer polymerization. Such processing is challenging for conventional systems utilizing electromagnetic coils and fluid cells due to the bulky nature of the coils and the need to maintain precise placement of the array within the coil/cell.

In an attempt to preserve the field-induced organization, we modified the chemical composition of the dispersion and changed the balance of nanorod-surface interactions. We suggested that adding dilute salt solutions (25 mM NaCl) to the nanorod array might decrease charge screening between the nanorods and the silicon substrate allowing the PVPON shells on the nanorods to physically adsorb to the substrate (Video 7.1). While this simple addition could freeze the nanorods, the anchoring was very weak as even mild rinsing dramatically disturbed the ordered arrays. Therefore, we developed a hydrogen-bonding based anchoring approach by introducing polymethacrylic acid PMAA/PVPON

functionalized substrates.[310,311] In this design, dilute solutions of PMAA were added dropwise to arrays formed in order to facilitate hydrogen-bond anchoring of PVPON-functionalized nanorod ends and substrate and the firm preservation of the initial ordering even after drying and rinsing processes (Figures 7.5b-d and 7.6a).

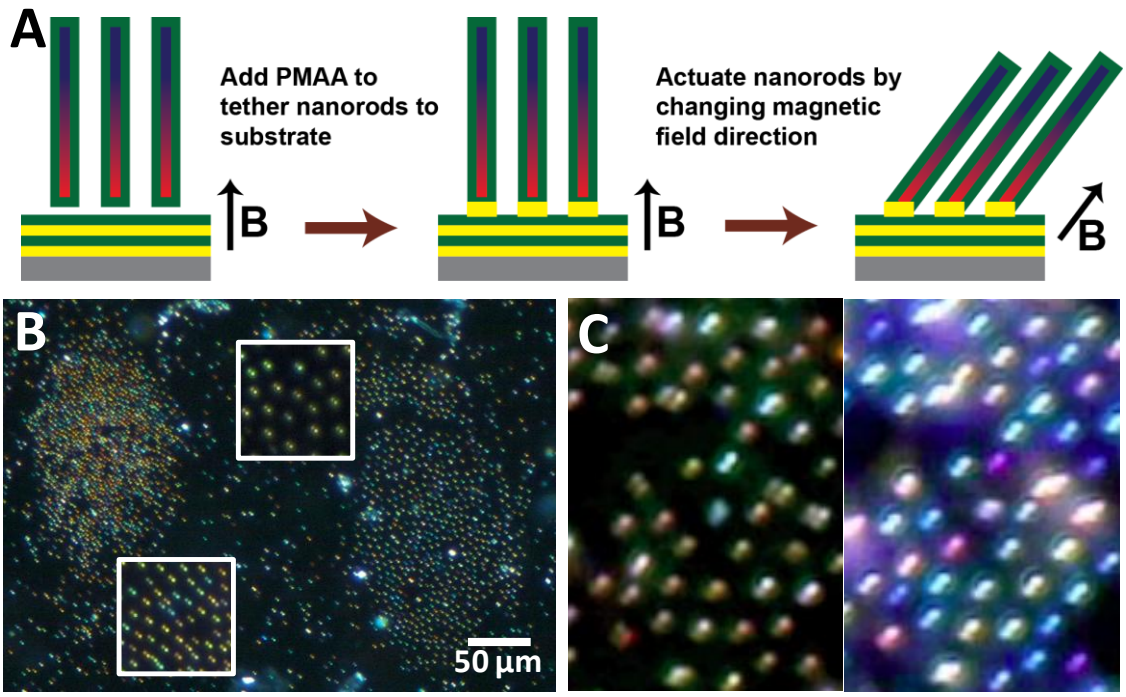

Figure 7.6: Sequential deposition of hierarchical assemblies and actuation of arrays. a) Schematic showing robust tethering process based on hydrogen-bonding between PMAA and PVPON layers. b) Darkfield optical image showing sequential deposition of two islands on the same substrate left island is comprised of 400 nm long nanorods and right-side island of 80 nm long rods. c) Darkfield images from movie S4 showing the change in scattering intensity as nanorods are actuated by an external magnetic field.

Moreover, the robust nature of the hydrogen-bonded coupling allowed deposition of multiple islands on the same substrate by repeating the assembly process at different locations (Figure 7.6b). Here, the island on the left side of the image is comprised of 400 nm long nanorods, and the island on the right side contains 800 nm long nanorods. As shown in Figure 6.4a, the island containing longer nanorods has larger lattice spacing.

The precise placement of the second island was achieved by registry of the desired location with the magnet center. The ability to sequentially deposit multiple islands with precise control of the island spacing could allow such a technique to be adopted for fabrication of multiplexed arrays for application in biological and chemical sensing. Furthermore, this method can easily be extended to a wide variety of shells with hydrogen-bonding, electrostatic interactions, or even covalent cross-linking.

An interesting consequence of the coupling method utilized here is that the polymer chains placed in-between the nanorod ends and the substrate can act as hinges about which the nanorods can freely rotate (Figure 7.6a). In this way, changing the magnetic field orientation leads to rapid actuation of the nanorod array in a manner similar to artificial cilia on flexible supports[312], and in contrast to microfabricated rod arrays which can only actuate via bending modes.[313,314,315] In Figure 7.6c and Video 7.3 the fast, real-time actuation of the nanorod array can be seen by the dramatic shift in the color and intensity of the scattered light. Changing the orientation of the nanorods from vertically standing to tilted increases the scattering cross-section, this is readily observed in the dark-field optical video.

7.4 Conclusion

The results presented here demonstrate a unique assembly of nickel nanorods into long-range organized lattices with tunable spacing and symmetry using a gradient magnetic field. Once at the substrate interface, the nanorods undergo a phase separation forming highly-open unfrustrated lattices, whose structure is governed by the long-range repulsive forces between the uniformly oriented adjacent magnetic dipoles. We suggest that the

high interfacial mobility of the nanorods along with long-range repulsion of kinetically confined magnetic dipoles resulted in the formation of unfrustrated triangular lattices with spacing between vertical nanorods exceeding their diameter by a ratio of 50:1 and open volume exceeding 99.9%. This assembly process is facilitated by the combination of magnetophoretic assembly, high lateral mobility of nanorods, kinetic confinement, and field/concentration-controlled phase separation. In contrast to ferrofluids and magnetorheologic fluids in a thin cell, which undergo phase separation when placed in orthogonal magnetic fields [316,317] a fluid cell confinement is not required in current approach.

These open lattices can be further locked in position by the simple triggering of hydrogen-bonding between the funcationalized nanorods and the substrate. This anchoring technique was extended to allow for assembly of multiple lattices with different geometries and spacing on the same substrate with precise registry. Furthermore, the hinge-like polymeric anchors offer the possibility to rapidly actuate the nanorods in a manner similar to artificial cilia. Thus, the magnetic-field assisted assembly of nanorods demonstrated here offers a unique combination of ease of assembly and ease of integration making it a promising platform for self-assembly in a wide range of applications including rapidly actuating arrays for micro- mixing/manipulation, biological/chemical sensing, and active magneto/optical/photonic systems. Compared to other self-assembled or lithographically fabricated post arrays this approach offers the advantage that long-range ordered arrays with uniform cilia lengths can be easily assembled *in situ* without the need for complex physical confinement. Moreover, the

ease of integrating other materials offers the possibility of creating magnetically actuated ferromagnetic arrays with fast-responsive multifunctional actuating behavior.

CHAPTER 8

GENERAL CONCLUSIONS, IMPACT, AND FUTURE DEVELOPMENTS

Throughout this work we have demonstrated template-assisted materials fabrication strategies to create active hybrid systems. The overall impact in the end of this work is to provide a basic framework for the utilization of such techniques to pattern both responsive polymers and nanomaterials in an effort to create novel and multifunctional active hybrid systems. These results have yielded developments of novel techniques for selective patterning of chain conformation in ultrathin films and long-range assembly and tethering of template fabricated nanorods.

We have suggested, developed, and shown assembly of multiple hybrid plasmonic systems and provided an understanding for design strategies for modulation of near-field vs. far-field coupling which were not revealed before. The importance of these results is two fold. First, to demonstrate how template and field assisted techniques can be leveraged to access spatial and temporal control in hybrid systems that cannot be commonly achieved through conventional lithographic or self-assembly based techniques. Second, to provide an understanding for how the interfacial and nanoscale structural properties dramatically impact the functional mechanical and optical properties in these hybrid systems. These techniques and understanding have the potential to impact the development of active hybrid material systems that are critical for next generation devices.

We have shown that the secondary structure of silk films can be patterned on the micron scale using a soft lithographic template with high spatial resolution. The selective transformation of the silk I structure resulted in well-defined regions with dramatically different mechanical, surface, and solubility properties controlled by local secondary structure of silk protein. The technique can also be extended as new paradigm for patterning the chain conformation of other materials including cellulose, scaffold proteins, collagen, and lipids. In the future, this technique will allow researchers to study the properties of silk I and silk II side by side and allow for the development of tailored protein materials with nominally uniform chemical composition but selectively transformed secondary structure.

At the next level of complexity, we have demonstrated a bimetallic hybrid nanostructure assembled from gold nanoparticles embedded into responsive PAA nanocoating around silver nanowires in which modulation of the gold-silver structural distances can serve as a chemical trigger for SERS activity. These finding are unique in that the modulation of optical Raman signal occurred without uncontrolled interparticle aggregation but only through changes in the interparticle distances within a single nanocob complex. The tunable separation distance between the two plasmonic nanostructures with nanometer precision and prevention of uncontrolled aggregation resulted in controlled modulation of electromagnetic coupling and thus a dramatic change in the corresponding SERS enhancement. The observed optical properties are reversible in wet state and can be presented in the dry state.

We suggest that the ability to change optical and SERS properties of a single nanostructure is a significant advancement over the current approach involving aggregation of multiple nanoparticles by allowing measurements to be made independently of nanoparticle concentration and under robust conditions. Placing nanoparticles inside polymer gel layer in close proximity to the nanowire surface suggested here effectively prevents any potential aggregation of nanoparticles under variable environmental conditions in contrast with regular nanoparticle solutions which easily precipitate with even slight change in environmental conditions (temperature, ionic conditions, pH, and shelf time). Nanoparticle complexes designed with the basic principles described in this work have the potential to play a significant role in chemical and biological sensing applications that can be expanded to a wide variety of extreme environmental conditions such as in-field, long-term, intracellular or *in vivo* applications.

The inherent advantage of template based strategies for fabricating nanorods is the ability to generate tailored linear arrays of rods with fine control over rod diameter, length, and spacing between rods. We have extended the versatility of this approach by demonstrating a simple method to transfer these linear nanorod assemblies in high quantity onto surfaces while preserving the fidelity of the local array structure. Moreover, we were able to measure the highly anisotropic LSPR optical properties at the single particle level using high-resolution hyperspectral imaging and suggest the origin of the multiple plasmon resonances including some peculiar optical features caused by characteristic fabrication defects. This capability to fabricate programmable assemblies and measure optical properties at the single particle level will be crucial for the practical

development of plasmonic antennas, SERS sensors, and multiplexed biological/chemical LSPR sensors. With further improvement in the assembly of these segmented nanorods with long-range order, this strategy has strong potential towards practical applications.

Further assembly of template fabricated nanorods into long-range organized lattices with tunable spacing and symmetry using a gradient magnetic field was also demonstrated. Once at the substrate interface, the nanorods undergo a phase separation forming highly-open unfrustrated lattices, whose structure is governed by the long-range repulsive forces between the uniformly oriented adjacent magnetic dipoles. We suggest that the high interfacial mobility of the nanorods along with long-range repulsion of kinetically confined magnetic dipoles resulted in the formation of unfrustrated triangular lattices with spacing between vertical nanorods exceeding their diameter by a ratio of 50:1 and open volume exceeding 99.9%. This assembly process is facilitated by the combination of magnetophoretic assembly, high lateral mobility of nanorods, kinetic confinement, and field/concentration-controlled phase separation. In contrast to ferrofluids and magnetorheologic fluids in a thin cell, which undergo phase separation when placed in orthogonal magnetic fields a fluid cell confinement is not required in current approach.

These open lattices can be further firmly locked in position by the simple triggering of hydrogen-bonding between the funcationalized nanorods and the substrate. This anchoring technique was extended to allow for assembly of multiple lattices with different geometries and spacing on the same substrate with precise registry. Furthermore, the hinge-like polymeric anchors offer the possibility to rapidly actuate the

nanorods in a manner similar to artificial cilia providing a new and facile route to nanostructures for microfluidic applications.

Thus, the magnetic-field assisted assembly of nanorods demonstrated offers a unique combination of ease of assembly and ease of integration making it a promising platform for self-assembly in a wide range of applications including rapidly actuating arrays for micro- mixing/manipulation, biological/chemical sensing, and active magneto/optical/photonic systems. Compared to other self-assembled or lithographically fabricated post arrays this approach offers the advantage that long-range ordered arrays with uniform cilia lengths can be easily assembled *in situ* without the need for complex physical confinement. Moreover, the ease of integrating other materials offers the possibility of creating magnetically actuated ferromagnetic arrays with fast-responsive multifunctional actuating behavior.

The work presented in this dissertation has been summarized in the following publications:

1. **M. K. Gupta**, S. Singamaneni, M. McConney, L. F. Drummy, R. R. Naik, V. V. Tsukruk. "A Facile Fabrication Strategy for Patterning Protein Chain Conformation in Silk Materials." *Adv. Mater.* **2010**, *22*, 115-119.

2. **M. K. Gupta**, S. Chang, S. Singamaneni, L. F. Drummy, R. Gunawidjaja, R. R. Naik, V. V. Tsukruk. "pH-Triggered SERS via Modulated Plasmonic Coupling in Individual Bimetallic Nanocobs." *Small* **2011**, *7*, 1192-1198.

3. S. L. Young, **M. K. Gupta**, C. Hanske, A. Fery, T. Scheibel, V. V. Tsukruk. "Utilizing Conformational Changes for Patterning Thin Films of Recombinant Spider Silk Proteins." *Biomacromol.* **2012**, *13*, 3189-3199.

4. **M. K. Gupta**, S. Naik, D. Nepal, L. F. Drummy, S. Biswas, M. F. Durstock, R. A. Vaia, V. V. Tsukruk. "Single Particle Measurement of Anisotropic Plasmonic Properties in Strongly Coupled One-Dimensional Segmented Gold Nanorods." *Adv. Funct. Mater.* (Submitted)

5. **M. K. Gupta,** D. Kulkarni, R. Geryak, S. Naik, V. V. Tsukruk, "A Robust and Facile Approach to Assembling Tunable, Mobile, and Highly-Open Unfrustated Triangular Lattices from Ferromagnetic Nanorods." *Nano Lett.* (Submitted)

The following publications are related to the work in this dissertation:

6. D. M. Anderson, **M. K. Gupta**, A. A. Voevodin, C. N. Hunter, S. A. Putnam, V. V. Tsukruk, A. G. Fedorov. "Using Amphiphilic Nanostructures to Enable Long-Range Ensemble Coalescence and Surface Rejuvenation in Dropwise Condensation." *ACS Nano* **2012**, *6*, 3262-3268.

7. R. Kodiyath, J. Wang, Z. A. Combs, S. Chang, **M. K. Gupta**, K. D. Anderson, R. J. C. Brown, V. V. Tsukruk. "SERS Effects in Silver-Decorated Cylindrical Nanopores." *Small* **2011**, *7*, 3452-3457.

8. R. Suntivich, I. Choi, **M. K. Gupta**, C. Tsitsilianis, V. V. Tsukruk. "Gold Nanoparticles Grown on Star-Shaped Block Copolymer Monolayers." *Langmuir* **2011**, *27*, 10730-10738.

9. O. Shchepelina, I. Drachuk, **M. K. Gupta**, J. Lin, V. V. Tsukruk. "Silk-on-Silk Layer-by-Layer Microcapsules." *Adv. Mater.* **2011**, *23*, 4655-4660.

10. S. Chang, Z. A. Combs, **M. K. Gupta**, R. Davis, V. V. Tsukruk. "In situ Growth of Silver Nanoparticles in Porous Membranes for Surface-Enhanced Raman Scattering." *ACS Appl. Mater. Interfaces* **2010**, *2*, 3333-3339.

11. E. Kharlampieva, D. Zimnitsky, **M. K. Gupta**, K. N. Bergman, D. L. Kaplan, R. R. Naik, V. V. Tsukruk. "Redox-Active Ultrathin Template of Silk Fibroin: Effect of Secondary Structure on Gold Nanoparticle Reduction." *Chem. Mat.* **2009**, *21*, 2696-2704.

12. S. Singamaneni, **M. K. Gupta**, R. Yang, M. M. Tomczak, R. R. Naik, Z. L. Wang, V. V. Tsukruk. "Nondestructive In Situ Identification of Crystal Orientation of Anisotropic ZnO Nanostructures." *ACS Nano* **2009**, *3*, 2593-2600.

Presentations

1. “Tunable Plasmonic Properties in One-dimensional Hybrid Nanostructures.” MRS Spring 2012 Conference, 04/12/2012, San Francisco, CA

2. “Template-Assisted Nanorod Dimers: Effect of Gap Size and Rod Length on Plasmon Coupling and Raman Enhancement.” MRS Fall 2011 Conference, 11/29/2011, Boston, MA (Poster)

3. “Responsive Nanocobs With Tunable SERS Intensity” MRS Spring 2010 Conference, 04/07/2010, San Francisco, CA (Poster)

4. “Strategy for Micropatterning Protein Chain Conformation in Silk Fibroin Materials.” MRS Spring 2010 Conference, 04/06/2010, San Francisco, CA (Poster)

5. “Control of Secondary Structure and Nanomechanical Properties of Silk Fibroin Films.” MRS Fall 2008 Conference, 12/04/2008, Boston, MA (Poster)

6. “Encapsulation of Enzymes on Silk Fibroin Fibers” MRS Spring 2008 Conference, 03/27/2008, San Francisco, CA (Poster)

REFERENCES

[1] W. A. Murray, W. L. Barnes *Adv. Mater.* **2007**, *19*, 3771-3782.

[2] K.-S. Lee, M. A. El-Sayed *J. Phys. Chem. B* **2006**, *110*, 19220-19225 .

[3] H. A. Atwater, .A. Polman *Nat. Mater.* **2010**, *9*, 205-213.

[4] S. J. Hurst, E. K. Payne, L. Qin, C. A. Mirkin *Angew. Chem. Int. Ed.* **2006**, *45*, 2672-2692.

[5] X. Huang, S. Neretina, M. A. El-Sayed *Adv. Mater.* **2009**, *21*, 4880-4910.

[6] Y. Sun, Y. Xia *Analyst* **2003**, *128*, 686-69.

[7] J. A. Schuller, E. S. Barnard, W. Cai, Y. C. Jun, J. S. White, M. L. Brongersma, *Nat. Mater.* **2010**, *9*, 193-204.

[8] C. J. Murphy, A. M. Gole, S. E. Hunyadi, J. W. Stone, P. N. Sisco, A. Alkilany, B. E. Kinard, P. Hankins *Chem. Commun.**2008***, 544-557.

[9] B. Sepulveda, P. C. Angelome, L. M. Lechuga, L. M. Liz-Marzan *Nano Today* **2009**, *4*, 244.

[10] M. A. C. Stuart, W. T. S. Huck, J. Genzer, M. Muller, C. Ober, M. Stamm, G. B. Sukhorukov, I. Szleifer, V. V. Tsukruk, M. Urban, F. Winnik, S. Zauscher, I. Luzinov, S. Minko *Nat. Mater.* **2010**, *9*, 101-113.

[11] I. Tokarev, S. Minko *Soft Matter*. **2009**, *5*, 511-524.

[12] Y. Roiter, S. Minko *J. Am. Chem. Soc*. **2005**, *127*, 15688-15689.

[13] Y. Li, T. Tanaka *Annu. Rev. Mater. Sci*. **1992**, *22*, 243-277.

[14] J. S. Mohammed, W. L. Murphy, *Adv. Mater***. 2009**, *21*, 1-14.

[15] S.-K. Ahn, R. M. Kasi, S.-C. Kim, N. Sharma, Y. Zhou *Soft Matter*. **2008**, *4*, 1151-1157.

[16] C. H. Alarcon, S Pennadam, C. Alexander *Chem. Soc. Rev***. 2005**, *34*, 276-285.

[17] A. Kumar, A. Srivastava, I. Y. Galaev, B. Mattiasson *Prog. Polym. Sci***. 2007**, *32*, 1205-1237.

[18] S. Sukhishvili *Curr. Opin. Coll. Interface. Sci.* **2005**, *10*, 37-44.

[19] T. Tanaka, I. Nishio, S.-T. Sun, S. Ueno-Nishio *Science*. **1982**, *218*, 467-469.

[20] A. Suzuki, T. Tanaka *Nature*, **1990**, *346*, 345-346.

[21] K. Glinel, C. Dejugnat, M. Prevot, B. Scholer, M. Schonhoff, R. V. Klitzing *Colloids Surf., A***. 2007**, *303*, 3-13.

[22] I. Tokareva, S. Minko, J. H. Fendler, E. Hutter *J. Am. Chem. Soc*. **2004**, *126*, 15950-15951.

[23] Y. Leroux, E. Eang, C. Fave, G. Trippe, J. Lacroix *Electrochem. Comm.* **2007**, *9*, 1258-1262.

[24] I. S. Lokuge, P. W. Bohn *Langmuir*. **2005**, *21*, 1979-1985.

[25] D. Palioura, S. P. Armes, S. H. Anastasiadis, M. Vamvakaki *Langmuir*. **2007**, *23*, 5761-5768.

[26] T. Asakura, J. Yao, T. Yamane, K. Umemura, S. A. Ulrich *J. Am. Chem. Soc.* **2002**, *124*, 8794.

[27] B. Lotz, H. D. Keith *J. Mol. Biol.* **1971**, *61*, 201.

[28] U.-J. Kim, J. H. Park, H. J. Kim, M. Wada, D. L. Kaplan *Biomaterials* **2005**, *26*, 2775.

[29] M. K. Gupta, S. K. Khokhar, D. M. Phillips, L. A. Sowards, L. F. Drummy, M. P. Kadakia, R. R. Naik, R. R. *Langmuir* **2007**, *23*, 1315.

[30] H.-J. Jin, J. Park, V. Karageorgiou, U.-J. Kim, R. Valluzzi, P. Cebe, D. L. Kaplan *Adv. Funct. Mater.* **2005**, *15*, 1241.

[31] E. Servoli, A. Maniglio, A. Motta, R. Predazzer, C. Migliaresi *Macromol. Biosci.* **2005**, *5*, 1175.

[32] G. H. Altman, F. Diaz, C. Jakuba, T. Calabro, R. L. Horan, J. Chen, H. Lu, J. Richmond, D. L. Kaplan *Biomaterials* **2003**, *24*, 401.

[33] R. V. Lewis *Chem. Rev.* **2006**, *106*, 3762.

[34] T. Arai, G. Freddi, R. Innocenti, M. Tsukada, *J. Appl. Polym. Sci.* **2004**, *91*, 2383.

[35] H. Shulha, C. Wong, D. L. Kaplan, V. V. Tsukruk *Polymer*, **2006**, *47*, 5821.

[36] C.-Z. Zhou, F. Confalonieri, M. Jacquet, R. Perasso, Z.-G. Li, J. Janin *Proteins* **2001**, *44*, 119.

[37] C. Z. Zhou, F. Confalonieri, N. Medina, Y. Zivanovic, C. Esnault, T. Yang, M. Jacquet, J. Janin, M. Duguet, R. Perasso, Z. G. Li *Nucleic Acids Res.* **2000**, *28*, 2413.

[38] B. D. Lawrence, M. Cronin-Golomb, I. Georgakoudi, D. L. Kaplan, F. G. Omenetto *Biomacromol.* **2008**, *9*, 1214.

[39] H. Perry, A. Gopinath, D. L. Kaplan, L. Dal Negro, F. G. Omenetto *Adv. Mater.* **2008**, *20*, 3070.

[40] F. G. Omenetto, D. L. Kaplan *Nat. Photonics* **2008**, *2*, 641.

[41] M. Demura, T. Asakura *Biotech. Bioeng.* **1989**, *33*, 598-603.

[42] E. S. Gil, S. M. Hudson, *Biomacromol.* **2007**, *8*, 258-264.

[43] E. S. Gil, S-H. Park, L. W. Tien, B. Trimmer, S. M. Hudson, D. L. Kaplan, *Langmuir* **2010**, *26*, 15614-15624.

[44] C. Ye, O. Schepelina, R. Calabrese, I. Drachuk, D. L. Kaplan, V. V. Tsukruk, *Biomacromol.* **2011**, *12*, 4319-4325.

[45] K. L. Kelley, E. Coronado, L. L. Zhao, G. C. Schatz *J. Phys. Chem. B* **2003**, *107*, 668.

[46] H. Ko, S. Singamaneni, V. V. Tsukruk *Small* **2008**, *4*, 1576.

[47] E. Hutter, J. H. Fendler *Adv. Mater.* **2004**, *16*, 1685.

[48] L. M. Liz-Marzan *Langmuir* **2006**, *22*, 32.

[49] M. Moskovits *Rev. Mod. Phys.* **1985**, *57*, 783.

[50] A. Tao, P. Sinsermsuksakul, P. Yang *Nat. Nano.* **2007**, *2*, 435.

[51] H. Masuda, K. Fukuda *Science.* **1995**, *268*, 1466-1468.

[52] A. P. Li, F. Müller, A. Birner, K. Nielsch, U. Gösele **1998,** *84,* 6023-6026.

[53] K. Nielsch, F. Müller, A. P. Li, U. ; Gösele *Adv. Mater.* ***2000,*** *12*, 582-586.

[54] Y. Zheng, T. Huang *J. Assoc. Lab. Automat.* **2008**, 13, 215-226 .

[55] Y. Xia, Y. Xiong, B. Lim, S. E. Skrabalak *Angew. Chem. Intern. Ed.* **2009**, *48*, 60-103.

[56] K. S. Lee, M. A. El-Sayed *J. Phys. Chem. B.* **2006**, *110*, 19220.

[57] M. E. Stewart, C. R. Anderton, L. B. Thompson, J. Maria, S. K. Gray, J. A. Rogers, R. G. Nuzzo *Chem. Rev.* **2008**, *108*, 494.

[58] J. Homola *Chem. Rev.* **2008**, *108*, 462.

[59] J. Homola *Anal. Bioanal. Chem.* **2003**, *377*, 528.

[60] C. D. Chen, S. F. Cheng, L. K. Chau, C. R. C. Wang, C. R. C. *Biosens. Bioelectron.* **2007**, *22*, 926.

[61] K. M. Mayer, S. Lee, H. Liao, B. C. Rostro, A. Fuentes, P. T. Scully, C. L. Nehl, J. H. Hafner *ACS Nano* **2008**, *2*, 687.

[62] A. J. Haes, R. P. Van Duyne *J. Am. Chem. Soc.* **2002**, *124*, 10596.

[63] J. C. Riboh, A. J. Haes, A. D. McFarland, C. R. Yonzon, R. P. Van Duyne *J. Phys. Chem.* B **2003**, *107*, 1772.

[64] C. R. Yonzon, E. Jeoung, S. Zou, G. C. Schatz, M. Mrksich, R. P. Van Duyne *J. Am. Chem. Soc.* **2004**, *126*, 12669.

[65] A. J. Haes, L. Chang, W. L. Klein, R. P. Van Duyne *J. Am. Chem. Soc.* **2005**, *127*, 2264.

[66] T. Endo, K. Kerman, N. Nagatani, H. M. Hiepa, D. K. Kim, Y. Yonezawa, K. Nakano, E. Tamiya *Anal. Chem.* **2006**, *78*, 6465.

[67] Y. B. Zheng, Y. W. Yang, L. Jensen, L. Fang, B. K. Juluri, A. H. Flood, P. S. Weiss, J. F. Stoddart, T. J. Huang *Nano Lett.* , **2009**, *9*, 819-825.

[68] Y. R. Leroux, J. C. Lacroix, K. I. Chane-Ching, C. Fave, N. Felid, G. Levi, J. Aubard, J. R. Krenn, A. Hohenas *J. Am. Chem. Soc.* **2005**, *127*, 16022-16023.

[69] P. Ahonen, D. J. Schiffrin, J. Paprotny, K. Kontturi *Phys. Chem. Chem. Phys.* **2007**, *9*, 651e658.

[70] L. Gunnarsson, T. Rindzevicius, J. Prikulis, B. Kasemo, M. Kall, S. Zou, G. C. Schatz *J. Phys. Chem. B.* **2005**, *109*, 1079.

[71] K. H. Su, Q. H. Wei, X Zhang, J. J. Mock, D. R. Smith, S. Schultz *Nano Lett.* **2003**, *3*, 1087.

[72] N. L. Rosi, C. A. Mirkin *Chem. Rev.* **2005**, *105*, 1547.

[73] B. M. Reinhard, M. Siu, H. Agarwal, A. P. Alivisatos, J. Liphardt *Nano Lett.* **2005**, *5*, 2246.

[74] M. S. Han, A. K. R. Lytton-Jean, C. A. Mirkin *J. Am. Chem. Soc.* **2006**, *128*, 4954.

[75] J. Zhang, L. Wang, D. Pan, S. Song, F. Y. C. Boey, H. Zhang, C. Fan, *Small* **2008**, *4*, 1196.

[76] C. L. Schofield, R. A. Field, D. A. Russell *Anal. Chem.* **2007**, *79*, 1356.

[77] J. Liu, Y. Lu *J. Am. Chem. Soc.* **2005**, *127*, 12677.

[78] I. Luzinov, S. Minko, V. V. Tsukruk *Soft Matter* **2008**, *4*, 714-725.

[79] I. Csetneki, G. Filipcsei, M. Zrnyi *Macromol.* **2006**, *39*, 1939-1942.

[80] D. Li, Q. He, Y. Yang, H. Mohwald, J. Li, *Macromol.* **2008**, *41*, 7254-7256.

[81] S. Santer, J. Rühe *Polymer, **2004,** 45,* 8279-8297.

[82] P. K. Jain, W. Huang, M. A. El-Sayed *Nano Lett.* **2007**, *7*, 2080-2088.

[83] D. M. Phillips, L. F. Drummy, D. G. Conrady, D. M. Fox, R. R. Naik, M. O. Stone, P. C. Trulove, H. C. De Long, R. A. Mantz *J. Am. Chem. Soc.* **2004**, *126*, 14350.

[84] D. M. Phillips, L. F. Drummy, R. R. Naik, H. C. De Long, D. M. Fox, P. C. Trulove, R. A. Mantz *J. Mater. Chem.* **2005**, *15*, 4206.

[85] K.-K.Chia, M. F. Rubner, R. E. Cohen *Langmuir*, **2009**, *25*, 14044-14052.

[86] C. Jiang, S. Markutsya, Y. Pikus, V. V. Tsukruk *Nat. Mater.* **2004**,*3*, 721-728.

[87] A. P. Li, F. Müller, A. Birner, K. Nielsch, U. Gösele, U. *Adv. Mater.* **1999,** *11***,** 483-487.

[79] A. P. Li, F. Müller, A. Birner, K. Nielsch, U. Gösele *J. Appl. Phys.* **1998**, *84*, 6023-6026.

[89] www.veeco.com.

[90] B. Ratner, V. V. Tsukruk *Scanning Probe Microscopy of Polymers.* B. Ratner, V.V. Tsukruk, Eds.; ACS Symposium Series; American Chemical Society: Washington, D.C., **1998**; Vol. 694.

[91] V. V. Tsukruk, K. Wahl *Microstructure and Microtribology of Polymer Surfaces.* V. V. Tsukruk, K. Wahl, Eds. ACS Symposium Series: Washington, D.C., **1999**, 741.

[92] B. Cappella, G. Dietler *Surface Science Reports* **1999**, *34*, 1.

[93] AFM Manual from the SEMA Lab

[94] X. Qian, J. Li, S. Nie *J. Am. Chem. Soc.* **2009**, *131*, 7540-7541.

[95] J. Nelayah, M. Kociak, O. Stephan, F. J. Garcia de Abajo, M. Tence, L. Henrad, D. Taverna, I. Pastoriza-Santos, L. M. Liz-Marzan, C. Colliex *Nat. Phys.*, **2007**,*3*, 348-353.

[96] M.-W. Chu, V. Myroshnychenko, C. H. Chen, J. P. Deng, C. Y. Mou, F. J. Garcia de Abajo *Nano Letters* **2009,***9*, 399-404.

[97] L. G. Griffith, G. Naughton, *Science* **2002**, *295*, 1009.

[98] R. O. Hynes, *Trends Cell Biol*. **1999**, *9*, M33.

[99] M. K. Gupta, S. K. Khokhar, D. M. Phillips, L. A. Sowards, L. F. Drummy, M. P. Kadakia, R. R. Naik, *Langmuir* **2007**, *23*, 1315.

[100] H.-J. Jin, J. Park, V. Karageorgiou, U.-J. Kim, R. Valluzzi, P. Cebe, D. L. Kaplan, *Adv. Funct. Mater.* **2005**, *15*, 1241.

[101] E. Servoli, A. Maniglio, A. Motta, R. Predazzer, C. Migliaresi, *Macromol. Biosci.* **2005**, *5*, 1175.

[102] G. H. Altman, F. Diaz, C. Jakuba, T. Calabro, R. L. Horan, J. Chen, H. Lu, J. Richmond, D. L. Kaplan, *Biomaterials* **2003**, *24*, 401.

[103] R. V. Lewis, *Chem. Rev.* **2006**, *106*, 3762.

[104] T. Arai, G. Freddi, R. Innocenti, M. Tsukada, *J. Appl. Polym. Sci.* **2004**, *91*, 2383.

[105] H. Shulha, C. Wong, D. L. Kaplan, V. V. Tsukruk, *Polymer*, **2006**, *47*, 5821.

[106] E. Kharlampieva, D. Zimnitsky, M. K. Gupta, K. N. Bergman, D. L. Kaplan, R. R. Naik, V. V. Tsukruk, *Chem. Mater* **2009**, *21*, 2696-2704.

[107] C.-Z. Zhou, F. Confalonieri, M. Jacquet, R. Perasso, Z.-G. Li, J. Janin, *Proteins* **2001**, *44*, 119.

[108] C.-Z. Zhou, F. Confalonieri, N. Medina, Y. Zivanovic, C. Esnault, T. Yang, M. Jacquet, J. Janin, M. Duguet, R. Perasso, Z. G. Li, *Nucleic Acids Res.* **2000**, *28*, 2413.

[109] B. D. Lawrence, M. Cronin-Golomb, I. Georgakoudi, D. L. Kaplan, F. G. Omenetto, *Biomacromolecules* **2008**, *9*, 1214.

[110] H. Perry, A. Gopinath, D. L. Kaplan, L. Dal Negro, F. G. Omenetto, *Adv. Mater.* **2008**, *20*, 3070.

[111] F. G. Omenetto, D. L. Kaplan, *Nat. Photonics* **2008**, *2*, 641.

[112] T. Asakura, J. Yao, T. Yamane, K. Umemura, A. S. Ulrich, *J. Am. Chem. Soc.* **2002**, *124*, 8794.

[113] B. Lotz, H. D. Keith, *J. Mol. Biol.* **1971**, *61*, 201.

[114] U.-J. Kim, J. H. Park, H. J. Kim, M. Wada, D. L. Kaplan, *Biomaterials* **2005**, *26*, 2775.

[115] H.-J. Jin, D. L. Kaplan, *Nature* **2003**, *424*, 1057.

[116] L. F. Drummy, B. Farmer, R. R. Naik, *Soft Matter* **2007**, *3*, 877.

[117] Z. Shao, F. Vollrath, *Nature* **2002**, *418*, 741.

[118] D. M. Phillips, L. F. Drummy, D. G. Conrady, D. M. Fox, R. R. Naik, M. O. Stone, P. C. Trulove, H. C. De Long, R. A. Mantz, *J. Am. Chem. Soc.* **2004**, *126*, 14350.

[119] D. M. Phillips, L. F. Drummy, R. R. Naik, H. C. De Long, D. M. Fox, P. C. Trulove, R. A. Mantz, *J. Mater. Chem.* **2005**, *15*, 4206.

[120] Socrates, G. Infrared and Raman characteristic group frequencies Tables and Charts 3rd Ed. Wiley, NY, 2001.

[121] H. Ko, C. Jiang, V. V. Tsukruk, *Chem. Mater.* **2005**, *17*, 5489.

[122] P. Monti, G. Freddi , A. Bertoluzza, N. Kasai, M. Tsukada, *J. Raman Spectrosc.* **1998**, *29*, 297.

[123] M. Tsukada, G. Freddi, P. Monti, A. Bertoluzza, N. Kasai, *J. Polym. Sci., Part B: Polym. Phys.* **2003**, *33*, 1995.

[124] V. V. Tsukruk, *Rubber Chem. Techn.* **1997**, *70*, 430.

[125] V. V. Tsukruk, D. H. Reneker *Polymer* **1995**, *36*, 1791.

[126] S. A. Chizhik, Z. Huang, V. V. Gorbunov, N. K. Myshkin, V. V. Tsukruk, *Langmuir* **1998**, *14*, 2606.

[127] V. V. Tsukruk, Z. Huang *Polymer* **2000**, *41*, 5541.

[128] I. Luzinov, D. Julthongpiput, V. V. Tsukruk *Macromolecules* **2000**, *33*, 7629.

[129] V. V. Tsukruk, Z. Huang, S. A. Chizhik, V. V. Gorbunov *J. Materials Science* **1998**, *33*, 4905.

[130] C. Jiang, X. Wang, R. Gunawidjaja, Y.-H. Lin, M. K. Gupta, D. L. Kaplan, R. R. Naik, V. V. Tsukruk *Adv. Funct. Mater.* **2007**, *17*, 2229.

[131] V. V. Tsukruk, V. N. Bliznyuk *Langmuir* **1998**, *14*, 446.

[132] V. V. Tsukruk, *Adv. Mater.* **2001**, *13*, 95.

[133] C. A. Mirkin, R. L. Letsinger, R. C. Mucic, J. J. Storhoff *Nature* **1996**, *382*, 607-609.

[134] J.-M. Nam, C. S. Thaxton, C. A. Mirkin *Science* **2003**, *301*, 1884-1886.

[135] T. Vo-Dinh, A. Dhawan, S. J. Norton, C. G. Khoury, H.-N. Wang, V. Misra, M. D. Gerhold *J. Phys. Chem. C* **2010**, *114*, 7480-7488.

[136] J. N. Anker, W. P. Hall, O. Lyandres, N. C. Shah, J. Zhao, R. P. Van Duyne *Nat. Mater.* **2008**, *7*, 442-453.

[137] H. Ko, S. Singamaneni, V. V. Tsukruk *Small* **2008**, *4*, 1576-1599.

[138] P. K. Jain, K. S. Lee, I. H. El-Sayed, M. A. El-Sayed *J. Phys. Chem. B* **2006**, *110*, 7238-7248.

[139] R. A. Alvarez-Puebla, L. M. Liz-Marzan *Energy Environ. Sci.* **2010**, *3*, 1011-1017.

[140] W. A. Murray, W. L. Barnes, *Adv. Mater.* **2007**, *19*, 3771-3782.

[141] C. Jiang, S. Markutsya, V. V. Tsukruk *Langmuir* **2004,** *20*, 882-890.

[142] R. A. Alvarez-Puebla, L. M. Liz-Marzán *Small* **2010**, *6*, 604-610.

[143] P. K. Jain, W. Huang, M. A. El-Sayed *Nano Lett.* **2007**, *7*, 2080-2088.

[144] H. Xu, E. Bjerneld, M. Käll, L. Börjesson *Phys. Rev. Lett.* **1999**, *83*, 4357-4360.

[145] H. Xu, J. Aizpurua, M. Käll, P. Apell *Phys. Rev. E* **2000**, *62*, 4318-4324.

[146] H. Xu, X.-H. Wang, M. Persson, H. Xu, M. Käll, P. Johansson *Phys. Rev. Lett.* **2004**, *93*, 243002.

[147] Y. Lu, L. G. Liu, L. P. Lee *Nano Lett.* **2005**, *5*, 5-9.

[148] C. E. Talley, J. B. Jackson, C. Oubre, N. K. Grady, C. W. Hollars, S. M. Lane, T. R. Huser, P. Nordlander, N. J. Halas *Nano Lett.* **2005**, *5*, 1569-1574.

[149] S. Chang, H. Ko, S. Singamaneni, R. Gunawidjaja, V. V. Tsukruk *Anal. Chem.* **2009,** *81*, 5740-5748.

[150] H. Ko, V. V. Tsukruk *Small* **2008**, *4*, 1980-1984.

[151] J. E. Ghadiali, M. M. Stevens *Adv. Mater*. **2008**, *20*, 4359-4363.

[152] V. Kozlovskaya, E. Kharlampieva, B. P. Khanal, P. Manna, E. R. Zubarev, V. V. Tsukruk *Chem. Mater.* **2008**, *20*, 7474-7485.

[153] Y. B. Zheng, T. J. Huang *J. Assoc. Lab. Autom.* **2008**, 13, 215-226.

[154] V. K. S. Hsiao, Y. B. Zheng, B. K. Juluri, T. J. Huang *Adv. Mater*. **2008**, *20*, 3528-3532.

[155] Y. B. Zheng, Y.-W. Yang, L. Jensen, L. Fang, B. K. Juluri, A. H. Flood, P. S. Weiss, J. F. Stoddart, T. J. Huang *Nano Lett*. **2009**, *9*, 819-825.

[156] E. Kharlampieva, V. Kozlovskaya, O. Zavgorodnya, G. D. Lilly, N. A. Kotov, V. V. Tsukruk *Soft Matter* **2010,** *6*, 800-807.

[157] M. A. C. Stuart, W. T. S. Huck, J. Genzer, M. Müller, C. Ober, M. Stamm, G. B. Sukhorukov, I. Szleifer, V. V. Tsukruk, M. Urban, F. Winnik, S. Zauscher, I. Luzinov, S. Minko *Nat. Mater*. **2010**, *9*, 101-113.

[158] I. Luzinov, S. Minko, V. V. Tsukruk *Prog. Polym. Sci.* **2004,** *29*, 635-698.

[159] I. Luzinov, S. Minko, V. V. Tsukruk *Soft Matter* **2008,** *4*, 714-725.

[160] M. De, P. S. Ghosh, V. M. Rotello *Adv. Mater*. **2008**, *20*, 4225-4241.

[161] J. A. Schuller, E. S. Barnard, W. Cai, Y. C. Jun, J. S. White, M. L. Brongersma *Nat. Mater.* **2010**, *9*, 193-204.

[162] C. J. Murphy, A. M. Gole, S. E. Hunyadi, J. W. Stone, P. N. Sisco, A. Alkilany, B. E. Kinard, P. Hankins *Chem. Commun.* **2008**, 544-557.

[163] B. Sepulveda, P. C. Angelome, L. M. Lechuga, L. M. Liz-Marzan *Nano Today* **2009**, *4*, 244-251.

[164] I. Tokarev, I. Tokareva, S. Minko *Adv. Mater.* **2008**, *20*, 2730-2734.

[165] A. Housni, Y. Zhao, Y. Zhao *Langmuir* **2010**, *26*, 12366-12370.

[166] A. Housni, Y. Zhao *Langmuir* **2010**, *26*, 12933-12939.

[167] X. Qian, J. Li, S. Nie *J. Am. Chem. Soc.* **2009**, *131*, 7540-7541.

[168] G. Song, C. Chen, J. Ren, X. Qu *ACS Nano* **2009**, *3*, 1183-1189.

[169] R. Gunawidjaja, S. Peleshanko, H. Ko, V. V. Tsukruk *Adv. Mater*. **2008**, *20*, 1544-1549

[170] B. Wiley, Y. Sun, Y. Xia *Langmuir* **2005**, *21*, 8077-8080.

[171] A. Tao, F. Kim, C. Hess, J. Goldberger, R. He, Y. Sun, Y. Xia, P. Yang *Nano Lett.* **2003**, *3*, 1229-1233.

[172] M. Brust, D. Bethell, D. J. Schiffrin, C. J. Kiely *Adv. Mater.* **1995**, *7*, 795-797.

[173] V. V. Tsukruk *Rubber Chem. Technol.* **1997**, *70*, 430.

[174] M. E. McConney, S. Singamaneni, V. V. Tsukruk *Polym. Rev.*, **2010,** *50*, 235-286.

[175] S. Singamaneni, M. Gupta, R. Yang, M. M. Tomczak, R. R. Naik, Z. L. Wang, V. V. Tsukruk *ACS Nano* **2009**, *3*, 2593-2600.

[176] R. Gunawidjaja, E. Kharlampieva, I. Choi, V. V. Tsukruk *Small* **2009**, *5*, 2460-2466.

[177] R. Sakthivel, B. Das, B. Satpati, B. K Mishra *Appl. Surf. Sci*. **2009**, *255*, 6577-6581.

[178] H. Kitano, Y. Akatsuka, N. Ise *Macromolecules* **1991**, *24*, 42-46.

[179] O. E. Philippova, D. Hourdet, R. Audebert, A. R. Khokhlov *Macromolecules* **1997**, *30*, 8278-8285.

[180] J. C. H. Spence, *High Resolution Electron Microscopy*, Oxford University Press, Oxford, United Kingdom, **2003**, p. 295.

[181] P. Hildenbrandt, M. Stockburger *J. Phys. Chem.* **1984**, *88*, 5935-5944.

[182] A. M. Michaels, L. Brus *J. Phys. Chem. B* **2000**, *104*, 11965-11971.

[183] J. Dong, Y. Ozaki, K. Nakashima *Macromolecules* **1997**, *30*, 1111-1117.

[184] H. Wei, F. Hao, Y. Huang, W. Wang, P. Nordlander, H. Xu *Nano Lett.* **2008**, *8*, 2497-2502.

[185] Y. Fang, H. Wei, F. Hao, P. Nordlander, H. Xu *Nano Lett.* **2009**, *9*, 2049-2053.

[186] N. J. Halas, S. Lal, W. S. Chang, S. Link, P. Nordlander *Chem. Rev.* **2011**, *111*, 3913-3961.

[187] R. Elghanian, J. J. Storhoff, R. C. Mucic, R. L. Letsinger, C. A. Mirkin *Science* **1997**, *277*, 1078-1081.

[188] S. Nie, S. R. Emory *Science* **1997**, *275*, 1102-1106.

[189] M. K. Gupta, S. Chang, S. Singamaneni, L. F. Drummy, R. Gunawidjaja, R. R. Naik, V. V. Tsukruk *Small* **2011**, *7*, 1192-1198.

[190] S. Chang, H. Ko, R. Gunawidjaja, V. V. Tsukruk *J. Phys. Chem. C* **2011**, *115*, 4387-4394.

[191] J. A. Schuller, E. S. Barnard, W. Cai, Y. C. Jun, J. S. White, M. L. Brongersma. *Nat. Mater.* **2010**, *9*, 193-204.

[192] H. A. Atwater, A. Polman *Nat. Mater.* **2010**, *9*, 205-213.

[193] J. N. Anker, W. Paige Hall, O Lyandres, N. C. Shah, J. Zhao, R. P. Van Duyne *Nat. Mater.* **2008**, *7*, 442-453.

[194] R. A. Alvarez-Puebla, L. M. Liz-Marzan *Small* **2010**, *6*, 604-610.

[195] H. Ko, S. Singamaneni, V. V. Tsukruk *Small* **2008**, *4*, 1576-1599.

[196] W. Rechberger, A. Hohenau, A. Leitner, J. R. Krenn, B. Lamprecht, F. R. Aussenegg *Opt. Commun.* **2003**, *220*, 137-141.

[197] P. K. Jain, W. Huang, M. A. El_Sayed *Nano Lett.* **2007**, 7, 2080-2088.

[198] P. K. Jain, M. A. El-Sayed *Chem. Phys. Lett.* **2010**, *487*, 153-164.

[199] C. Tabor, D. Van Haute, M. A. El-Sayed *ACS Nano* **2009**, *3*, 3670-3678.

[200] R. Near, C. Tabor, J. Duan, R. Pachter, M. A. El-Sayed *Nano Lett.* **2012**, *12*, 2158-2164.

[201] V. M. Shalaev, W. Cai, U. K. Chettiar, H. K. Yuan, A. K. Sarychev, V. P. Drachev, A. V. Kildishev *Opt. Lett.* **2005**, *30*, 3356-3368.

[202] J. B. Lassiter, H. Sobhani, J. A. Fan, J. Kundu, F. Capasso, P. Nordlander, N. J. Halas *Nano Lett.* **2010**, *10*, 3184-3189.

[203] Z. Fang, J. Cai, Z. Yan, P. Nordlander, N. J. Halas, X. Zhu *Nano Lett.* **2011**, *11*, 4475-4479.

[204] J. Ye, F. Wen, H. Sobhani, J. B. Lassiter, P. Van Dorpe, P. Nordlander, N. J. Halas *Nano Lett.* **2012**, *12*, 1660-1667.

[205] B. Luk'yanchuk, N. I. Zheludev, S. A. Maier, N. J. Halas, P. Nordlander, H. Giessen, C. T. Chong *Nat. Mater.* **2010**, *9*, 707-715.

[206] P. Nagpal, N. C. Lindquist. S.-H. Oh, D. J. Norris *Science* **2009**, *325*, 594-597.

[207] K. Kiu, Z. Nie, N. Zhao, W. Li, M. Rubinstein, E. Kumacheva, *Science* **2010**, *329*, 197-200.

[208] Z. Nie, D. Fava, M. Rubinstein, E. Kumacheva *J. Am. Chem. Soc.* **2008**, *130*, 3683-3689.

[209] A. P. Alivisatos, K. P. Johnsson, X. Peng, T. E. Wilson, C. J. Loweth, M. P. Bruchez , P. G. Schultz *Nature* **1996**, *382*, 609-611.

[210] S. Y. Park, A. K. R. Lytton-Jean, B. Lee, S. Weigand, G. C. Schatz, C. A. Mirkin *Nature*, **2008**, *451*, 553-556.

[211] D. Nykpanchuk, M. M. Maye, D. van der Lelie, O. Gang *Nature*, **2008**, *451*, 549-552.

[212] A. Guerrero-Martinez, J. Perez-Juste, E. Carbo-Argibay, G. Tardajos, L. M. Liz-Marzan *Angew. Chem. Int. Ed.* **2009**, ***48***, 9484-9488.

[213] S. Pal, Z. Deng, H. Wang, S. Zou, Y. Liu, H. Yan *J. Am. Chem. Soc.* **2011**, *133*, 1706-1709.

[214] J. M. Slocik, F. Tam, N. J. Halas, R. R. Naik *Nano Lett.* **2007**, *7*, 1054-1058.

[215] M. P. Busson, B. Rolly, B. Stout, N. Bonod, E. Larquet, A. Polman, S. Bidault *Nano Lett.* **2011**, *11*, 5060-5065.

[216] M. Rycenga, J. M. McLellan, Y. Xia *Adv. Mater.* **2008**, *20*, 2416-2420.

[217] D. Nepal, K. Park, R. A. Vaia *Small* **2012**, *8*, 1013-1020.

[218] N. Gandra, A. Abbas, L. Tian, S. Singamaneni *Nano Lett.* **2012**, *12*, 2645-2651.

[219] R. J. Macfarlane, B. Lee, M. R. Jones, N. Harris, G. C. Schatz, C. A. Mirkin *Science* **2011**, *334*, 204-208.

[220] K. Park, H. Koerner, R. A. Vaia *Nano Lett.* **2010**, *10*, 1433-1439.

[221] D. Nepal, M. S. Onses, K. Park, M. Jespersen, C. J. Thode, P. F. Nealey, R. A. Vaia *ACS Nano* **2012**, *6*, 5693-5701.

[222] C. Kuemin, L. Nowack, L. Bozano, N. D. Spencer, H. Wolf *Adv. Funct. Mater.* **2012**, *22*, 702-708.

[223] T. Thai, Y. Zheng, S. H. Ng, S. Mudie, M. Altissimo, U. Bach *Angew. Chem. Int. Ed.* **2012**, *51*, 8732-8735.

[224] C. R. Martin, *Science* **1994**, *266*, 1961-1966.

[225] M. R. Jones, K. D. Osberg, R. J. Macfarlane, M. R. Langille, C. A. Mirkin *Chem. Rev.* **2011**, *111*, 3736-3827.

[226] S. J. Hurst, E. K. Payne, L. Qin, C. A. Mirkin *Angew. Chem. Int. Ed.* **2006**, *45*, 2672-2692.

[227] T. R. Kline, M. Tian, J. Wang, A. Sen, M. W. H. Chan, T. E. Mallouk *Inorg. Chem.* **2006**, *45*, 7555-7565.

[228] L. Jiang, Y. Sun, F. Huo, H. Zhang, L. Qin, S. Li, X. Chen *Nanoscale* **2012**, *4*, 66-75.

[229] D. AlMawlawi, N. Coombs, M. Moskovits *J. Appl. Phys.* **1991**, *70*, 4421-4425.

[230] S. R. Nicewarner-Pena, R. G. Freeman, B. D. Reiss, L. He, D. J. Pena, I. D. Walton, R. Cromer, C. D. Keating, M. J. Natan *Science* **2001**, *294*, 137-141.

[231] R. Elnathan, R. Kantaev, F. Patolsky *Nano Lett.* **2008**, *8*, 3964-3972.

[232] W. Lee, R. Scholz, K. Nielsch, U. Gosele *Angew. Chem. Int. Ed.* **2005**, *44*, 6050-6054.

[233] C. D. Keating, M. J. Natan *Adv. Mater.* **2003**, *15*, 451-454.

[234] S. Kim, K. L. Shuford, H.-M. Bok, S. K. Kim, S. Park *Nano Lett.* **2008**, *8*, 800-804.

[235] S. Kim, S. K. Kim, S. Park *J. Am. Chem. Soc.* **2009**, *131*, 8380-8381.

[236] A. L. Schmucker, N. Harris, M. J. Banholzer, M. G. Blaber, K. D. Osberg, G. C. Schatz, C. A. Mirkin *ACS Nano* **2010**, *4*, 5453-5463.

[237] S. Liu, J. B.-H. Tok, Z. Bao *Nano Lett.* **2005**, *5*, 1071-1076.

[238] L. Qin, S. Park, L. Huang, C. A. Mirkin *Science* **2005**, *309*, 113-115.

[239] T. Mirkovic, M. L. Foo, A. C. Arsenault, S. Fournier-Bidoz, N. S. Zacharia, G. A. Ozin *Nat. Nanotech.* **2007**, *2*, 565-569.

[240] K. D. Osberg, A. L. Schmucker, A. J. Senesi C. A. Mirkin, *Nano Lett.* **2011**, *11*, 820-824.

[241] L. Qin, J.-W. Jang, L. Huang, C. A. Mirkin *Small*, **2007**, *3*, 86-90.

[242] L. Qin, M. J. Banholzer, J. E. Millstone, C. A. Mirkin *Nano Lett.* **2007**, *7*, 3849-3853.

[243] M. J. Banholzer, K. D. Osberg, S. Li, B. F. Mangelson, G. C. Schatz, C. A. Mirkin *ACS Nano* **2010**, *4*, 5446-5452.

[244] W. Wei, S. Z. Li, L. D. Qin, C. Xue, J. E. Millstone, X. Y. Xu, G. C. Schatz, C. A. Mirkin *Nano Lett.* **2008**, *8*, 3446-3449.

[245] L. Qin, S. Zou, C. Xue, A. Atkinson, G. C. Schatz C. A. Mirkin, *Proc. Natl. Acad. Sci.* **2006**, *103*, 13300-13303.

[246] D. M. O'Carroll, C. E. Hofmann, H. A. Atwater *Adv. Mater.* **2010**, *22*, 1223-1227.

[247] M. L. Pedano, S. Li, G. C. Schatz, C. A. Mirkin *Angew. Chem. Int. Ed.* **2010**, *49*, 78-82.

[248] W. Wei, S. Z. Li, J. E. Millstone, M. J. Banholzer, X. D. Chen, X. Y. Xu, G. C. Schatz, C. A. Mirkin *Angew. Chem. Int. Ed.* **2009**, *48*, 4210-4212.

[64] M. J. Banholzer, L. Qin, J. E. Millstone, K. D. Osberg, C. A. Mirkin *Nat. Prot.* **2009**, *4*, 838-848.

[250] K. D. Osberg, M. Rycenga, N. Harris, A. L Schmucker, M. R. Langille, G. C. Schatz, C. A. Mirkin *Nano Lett.* **2012**, *12*, 3828-3832.

[251] P. B. Johnson, R. W. Christy *Phys. Rev. B* **1972**, *6*, 4370-4379.

[252] S. A. Maier, M. L. Brongersma, P. R. Kik, H. A. Atwater *Phys. Rev. B* **2002**, *65*, 193408.

[253] L. Slaughter, W.-S. Chang, S. Link *J. Phys. Chem. Lett.* **2011**, *2*, 2015-2023.

[254] A. Gole, C. J. Murphy *Chem. Mater.* **2005**, *17*, 1325-1330.

[255] A. M. Alkilany, L. B. Thompson, C. J. Murphy *ACS Appl. Mater. Interfaces* **2010**, *2*, 3417-3421.

[256] S. Vial, I. Pastoriza-Santos, J. Perez-Juste, L. M. Liz-Marzan *Langmuir* **2007**, *23*, 4606-4611.

[257] V. Kozlovskaya, E. Kharlampieva, B. P. Khanal, P. Manna, E. R. Zubarev, V. V. Tsukruk *Chem. Mater.* **2008**, *20*, 7474-7485.

[258] L. Tian, M. Fei, R. Kattumenu, A. Abbas, S. Singamaneni *Nanotechnology*, **2012**, *23*, 255502.

[259] J. Lim, C. Lanni, E. R. Evarts, F. Lanni, R. D. Tilton, S. A. Majetich *ACS Nano* **2011**, *5*, 217-226.

[260] P. K. Jain, S. Eustis, M. A. El-Sayed *J. Phys. Chem. B* **2006**, *110*, 18243-18253.

[261] A. S. Stender, G. Wang, W. Sun, N. Fang *ACS Nano* **2010**, *4*, 7667-7675.

[262] O. L. Muskens, G. Bachelier, N. Del Fatti, F. Vallée, A. Brioude, X. Jiang, M. P. Pileni *J. Phys. Chem. C* **2008**, *112*, 8917-8921.

[263] S. Link, M. B. Mohamed, M. A. El-Sayed *J. Phys. Chem. B* **1999**, *103*, 3073-3077.

[264] J.-M. Moon, A. Wei. *J. Phys. Chem. B* **2005**, *109*, 23336-23341.

[265] K.-S. Lee, M. A. El-Sayed *J. Phys. Chem. B* **2005**, *109*, 20331-20338.

[266] S. Link, M. A. El-Sayed *J. Phys. Chem. B* **1999**, *103*, 8410-8426.

[267] J. M. K. Bishop, C. E. Wilmer, S. Soh, B. A. Grzybowski *Small* **2009**, *5*, 1600-1630.

[268] V. J. Anderson, H. N. W. Lekkerkerker *Nature* **2002**, *416*, 811-815.

[269] S. C. Glotzer, M. J. Solomon *Nat. Mater.* **2007**, *6*, 557-562.

[270] X. Ye, L. Qi *Nano Today* **2011**, *6*, 608-631.

[271] A. van Blaaderen, R. Ruel, P. Wiltzius *Nature* **1997**, *385*, 321-324.

[272] J. P. Hoogenboom, A. K. van Langen-Suurling, J. Romijn, A. van Blaaderen *Phys. Rev. Lett.* **2003**, *90*, 138301.

[273] E. V. Shevchenko, D. V. Talapin, N. A. Kotov, S. O'Brien, C. B. Murray *Nature* **2006**, *439*, 55-59.

[274] Y. Yin, Y. Lu, B. Gates, Y. Xia *J. Am. Chem. Soc.* **2001**, *123*, 8718-8729.

[275] Y. Xia, Y. Yin, Y. Lu, J. McLellan *Adv. Funct. Mat.* **2003**, *13*, 907-918.

[276] Q. Chen, S. C. Bae, S. Granick *Nature* **2011**, *469*, 381-385.

[277] S. K. Smoukov, S. Gangwal, M. Marquez, O. D. Velev *Soft Matter* **2009**, *5*, 1285-1292.

[278] Z. Nie, D. Fava, M. Rubinstein, E. Kumacheva *J. Am. Chem. Soc.* **2008**, *130*, 3683-3689.

[279] A. P. Alivisatos, K. P. Johnsson, X. Peng, T. E. Wilson, C. J. Loweth, M. P. Bruchez Jr, P. G. Schultz *Nature* **1996**, *382*, 609-611.

[280] S. Y. Park, A. K. R. Lytton-Jean, B. Lee, S. Weigand, G. C. Schatz, C. A. Mirkin *Nature* **2008**, *451*, 553-556.

[281] D. Nykpanchuk, M. M. Maye, D. van der Lelie, O Gang *Nature* **2008**, *451*, 549-552.

[282] R. J. Macfarlane, B. Lee, M. R. Jones, N. Harris, G. C. Schatz, C. A. Mirkin *Science* **2011**, *334*, 204-208.

[283] A. Guerrero-Martinez, J. Perez-Juste, E. Carbo-Argibay, G. Tardajos, L. M. Liz-Marzan *Angew. Chem. Int. Ed.* **2009**, *48*, 9484-9488.

[284] A. L. Rogach, N. A. Kotov, D. S. Koktysh, J. W. Ostrander, G. A. Ragoisha, *Chem. Mater.* **2000**, *12*, 2721-2726.

[285] M. Giersig, P. Mulvaney *Langmuir* **1993**, *9*, 3408-3413.

[286] M. Trau, D. A. Saville, I. A. Aksay *Science* **1996**, *272*, 706-709.

[287] S. O. Lumsdon, E. W. Kaler, J. P. Williams, O. D. Velev *Appl. Phys. Lett.* **2003**, *82*, 949-951.

[288] M. Golosovsky, Y. Saado, D. Davidov *Phys. Rev. E* **2002**, *65*, 061405.

[289] E. Alsberg, E. Feinstein, M. P. Joy, M. Prentiss, D. E. Ingber *Tissue Eng.* **2006**, *12*, 3247-3256.

[290] D. C. Pregibon, M. Toner, P. S. Doyle *Langmuir* **2006**, *22*, 5122-5128.

[291] C. M. Hangarter, Y. Rheem, B. Yoo, E.-H. Yang, N. V. Myung *Nanotechnology* **2007**, *18*, 205305.

[292] W. Wen, L. Zhang, P. Sheng *Phys. Rev. Lett.* **2000**, *85*, 5464-7.

[293] B. A. Grzybowski, H. A. Stone, G. M. Whitesides *Nature* **2000**, *405*, 1033-1036.

[294] M. Motornov, S. Z. Malynych, D. S. Pippalla, B Zdyrko, H. Royter, Y. Roiter, M. Kahabka, A. Tokarev, I. Tokarev, E. Zhulina, K. G. Kornev, I. Luzinov, S. Minko *Nano Lett.* **2012**, *12*, 3814-3820.

[295] P. Y. Keng, I. Shim, B. D. Korth, J. F. Douglas, J. Pyun *ACS Nano* **2007**, *1*, 279-292.

[296] S. E. Bowles, W. Wu, T. Kowalewski, M. C. Schalnat, R. J. Davis, J. E. Pemberton, I Shim, B. D. Korth, J. Pyun *J. Am. Chem. Soc.* **2007**, *129*, 8694-8695.

[297] C. R. Martin *Science* **1994**, *266*, 1961-1966.

[298] J. C. Hulteen, C. R. Martin *J. Mater. Chem.* **1997**, *7*, 1075-1087.

[299] M. J. Banholzer, L. Qin, J. E. Millstone, K. D. Osberg, C. A. Mirkin *Nat. Prot.* **2009**, *4*, 838-848.

[301] V. V. Tsukruk, S. Singamaneni *Scanning Probe Microscopy of Soft Matter: Fundamentals and Practices*; Wiley-VCH: New York, **2012**.

[301] C. R. Martin *Science* **1994**, *266*, 1961-1966.

[302] J. C. Hulteen, C. R. Martin *J. Mater. Chem.* **1997**, *7*, 1075-1087.

[303] M. J. Banholzer, L. Qin, J. E. Millstone, K. D. Osberg, C. A. Mirkin *Nat. Prot.* **2009**, *4*, 838-848.

[304] M. R. Jones, K. D. Osberg, R. J. Macfarlane, M. R. Langille, C. A. Mirkin *Chem. Rev.* **2011**, *111*, 3736-3827.

[305] L. Sun, Y. Hao, C.-L. Chien, P. C. Searson *IBM J. Res. & Dev.* **2005**, *49*, 79-102.

[306] J. Lim, D. X. Tan, F. Lanni, R. D. Tilton, S. A. Majetich *J. Magn. Magn. Mater.* **2009**, *321*, 1557-1562.

[307] J. Lim, C. Lanni, E. R. Evarts, F. Lanni, R. D. Tilton, S. A. Majetich *ACS Nano* **2011**, *5*, 217-226.

[308] R. F. Wang, C. Nisoli, R. S. Freitas, J. Li, W. McConville, B. J. Cooley, M. S. Lund, N. Samarth, C. Leighton, V. H. Crespi, P. Schiffer *Nature* **2006**, *439*, 303-306.

[309] Singamaneni, S.; Bliznyuk, V. N.; Binek, C.; Tsymbal, E. Y. *J. Mater. Chem.* **2011**, *21*, 16819-16845.

[310] E. Kharlampieva, V. Kozlovskaya, S. A. Sukhishvili *Adv. Mater.* **2009**, *21*, 3053-3065.

[311] V. Kozlovskaya, E. Kharlampieva, B. P. Khanal, P. Manna, E. R. Zubarev, V. V. Tsukruk *Chem. Mater.* **2008**, *20*, 7474-7485.

[312] M. E. McConney, K. D. Anderson, L. L. Brott, R. R. Naik, V. V. Tsukruk *Adv. Funct. Mater.* **2009**, *19*, 2527-2544.

[313] H. Singh, P. E. Laibinis, T. A. Hatton *Nano Lett.* **2005**, *5*, 2149-2154.

[314] B. A. Evans, A. R. Shields, R. L. Carroll, S. Washburn, M. R. Falvo, R. Superfine *Nano Lett.* **2007**, *7*, 1428-1434.

[315] A. Sidorenko, T. Krupenkin, A. Taylor, P. Fratzl, J. Aizenberg *Science* **2007**, *315*, 487-490.

[316] D. Andelman, R. E. Rosensweig *J. Phys. Chem. B* **2009**, *113*, 3785-3798.

[317] H. Wolf, R. Birringer *J. Appl. Phys.* **2005**, *98*, 074303.

VITA

Maneesh K. Gupta

Maneesh Gupta was born in Dayton, Ohio on August 26, 1982 to Rakesh and Santosh Gupta. He attended Beavercreek City Schools and graduated from Beavercreek High School in 2000. In 2004, he obtained a B.S. in Chemical Engineering from the University of Illinois at Urbana-Champaign. From 2004 to 2007, he worked in the Materials and Manufacturing Directorate at the Air Force Research Laboratories in Dayton, Ohio under the guidance of Dr. Rajesh Naik, and completed a M.S. in Biomedical Engineering from Wright State University. In 2008, He began a Ph.D. in Materials Science and Engineering at the Georgia Institute of Technology with Prof. Vladimir Tsukruk. On August 22, 2009, Maneesh and Kamna Mehta (daughter of Rajendra and Sushma Mehta) were married. After completion of his Ph.D., Maneesh will begin a post-doctoral position at Princeton University with Prof. Michael McAlpine.